



TECHNISCHE
UNIVERSITÄT
WIEN
Vienna | Austria

UNTERSCHRIFT (BETREUER)

DIPLOMARBEIT

VASP SIMULATION OF
THORIUM DOPED
MAGNESIUM FLUORIDE

AUSGEFÜHRT AM INSTITUT FÜR
ANGEWANDTE PHYSIK
DER TECHNISCHEN UNIVERSITÄT WIEN

UNTER DER ANLEITUNG VON

UNIV. PROF. DIPL.-ING. DR. TECHN. PETER MOHN
DIPL.-ING. JOHANNES GUGLER

DURCH

MARTIN PIMON
Stolzenhalergasse 21/13
1080 Wien, Österreich

11. DEZEMBER 2017

UNTERSCHRIFT (STUDENT)

Abstract

For the construction of new types of atomic clocks, the metastable thorium isotope ^{229m}Th has been proposed due to its extremely low excitation energy, which lies in the range of electronic transitions. This type of clock may realize time measurements with unparalleled precision. Since this thorium isotope is very rare, it needs to be doped into a host crystal. To measure the core transition energy, it is necessary that the crystal is transparent in that energy regime.

A possible host for the thorium isomer is magnesium fluoride with the chemical formula MgF_2 , which was simulated using the Vienna Ab-initio Simulation Package (VASP). The theoretical background of VASP is Density Functional Theory, which is summarized in this work, in addition to the numerical treatment of molecular dynamics. The electronic structure and optical properties of MgF_2 were studied and it was determined whether thorium will be accepted as a dopant and which charge compensations occur. Energetically, the most favorable compensation is a substitutional doping of thorium with the interstitial placement of two fluorine atoms. Furthermore, the size of the band gap was determined for different configurations to see if MgF_2 stays transparent for the isomer energy. It is shown that the gap preserves its size for the most probable configurations. Additionally, the first excited states originate almost exclusively from the thorium atom. It may therefore be possible that the nucleus is excited via the electron-bridge mechanism, which serves as an outlook for further theoretical and experimental work.

Kurzfassung

Für die Konstruktion einer neuartigen Atomuhr wurde das metastabile Thorium Isotop ^{229m}Th vorgeschlagen, weil es eine sehr niedrige Anregungsenergie besitzt, die in der Nähe von elektronischen Übergängen liegt. Diese Art von Uhr würde Zeitmessungen mit bisher unerreichter Präzision ermöglichen. Da dieses Thorium Isotop extrem selten ist, muss es in einen Kristall dotiert werden. Um die Anregungsenergie des Kerns zu messen, ist es zudem erforderlich, dass der Kristall transparent für diesen Energiebereich ist.

Ein mögliches Trägermaterial ist Magnesiumfluorid mit der chemischen Formel MgF_2 , das mit dem Vienna Ab-initio Simulation Package (VASP) simuliert wurde. Der theoretische Hintergrund von VASP ist die Dichtefunktionaltheorie, die in dieser Arbeit zusammengefasst ist. Zusätzlich wird die numerische Behandlung von Moleküldynamik diskutiert. Die elektronischen und optischen Eigenschaften von MgF_2 wurden in dieser Arbeit erforscht. Es wurde bestimmt, ob Thorium vom Trägermaterial als Dotand akzeptiert wird und welche Art der Ladungskompensation am wahrscheinlichsten stattfindet. Die energetisch günstigste Konfiguration ist der substitutionale Einbau von Thorium und der interstitielle Einbau von zwei Fluor Atomen. Weiterhin wurde die Größe der Bandlücke für verschiedene Konfigurationen berechnet um zu überprüfen, ob MgF_2 transparent für die Isomerenergie bleibt. Es wird gezeigt, dass die Bandlücke ihre ursprüngliche Größe für die wahrscheinlichsten Konfigurationen nahezu behält. Zusätzlich stammen die ersten angeregten Zustände beinahe ausschließlich vom Thorium Atom. Es könnte daher möglich sein, dass der Kern über den Elektronenbrückenmechanismus angeregt wird, was einen Ausblick auf weitere theoretische und experimentelle Arbeit eröffnet.

Contents

1	Introduction	1
2	Theory	3
2.1	Introduction	3
2.1.1	Schrödinger Equation	3
2.1.2	Band Gap	5
2.1.3	Born-Oppenheimer Approximation	6
2.2	Density Functional Theory	8
2.2.1	Hartree-Fock Equations	8
2.2.2	Hohenberg-Kohn Theorem	10
2.2.3	Thomas-Fermi Theory	11
2.2.4	Energy Functional	12
2.2.5	Kohn-Sham Equations	14
2.2.6	Local Density Approximation	16
2.2.7	Generalized Gradient Approximation	17
2.2.8	Hybrid Functionals	17
2.3	Ionic Movement	18
2.4	Methods	20
2.4.1	Basis Sets	20
2.4.2	Pseudopotentials	20
2.4.3	Brillouin Zone Sampling	21
2.4.4	Smearing	23
2.4.5	Differential Equations	24

3	Results	27
3.1	Convergence Studies	27
3.1.1	Cutoff Convergence	27
3.1.2	\mathbf{k} -Space Mesh	28
3.2	Structure	30
3.3	Electronic Configuration	31
3.3.1	Band Structure	32
3.3.2	Density Of States	34
3.4	Optical Studies	34
3.5	Total Energies	36
3.6	Doping	37
3.6.1	Cell Size	39
3.6.2	Γ -only \mathbf{k} -mesh	40
3.7	Charge Compensation	41
3.7.1	Overview	41
3.8	Electric Field Gradient	45
4	Discussion	49
	Appendices	53
A	Theory	53
A.1	Isomer states	53
A.2	Ritz Method	55
A.3	Functionals	55
A.4	PBE Functional	57
A.5	Optics	58
B	Optimization	61
B.1	Compilation	61
B.2	Ionic Relaxation Parameters	61
B.3	Paralellization	62
C	List of Calculations	65

C.1	Total Energies	65
C.1.1	+O (Interstitial)	65
C.1.2	+2O (Substitutional)	66
C.1.3	+2F (Interstitial)	66
C.1.4	−Mg (Vacancy)	67
C.1.5	No Doping	68
C.1.6	PBE	68
C.2	Plots	70
C.2.1	O Interstitial	71
C.2.2	O Substitutional	75
C.2.3	F Interstitial	79
C.2.4	Mg vacancy	96

List of Symbols and Notation

$ \Psi\rangle$	Abstract wave vector
H	Hamilton operator
E	Energy
T	Kinetic energy operator
V	Potential
n	Refers to a nucleus
e	Refers to an electron
K	Total number of nuclei
\mathbf{R}	Position of a nucleus
σ	Spin of a particle
M	Mass of a nucleus
Z	Charge of a nucleus
N	Total number of electrons
Ψ	Wave function
Δ	Band gap
\mathbf{k}	Wave vector
ϕ	Single electron wave function
O	Arbitrary observable

Chapter 1

Introduction

The fundamental unit of time, the second, is since 1968 defined by the *International System of Units* as the following:

The second is the duration of 9 192 631 770 periods of the radiation corresponding to the transition between the two hyperfine levels of the ground state of the caesium 133 atom.

It was later added that the caesium atom is at rest at 0 K [dPeM06].

At first it might seem unnatural to assign such an intricate definition for a mundane quantity as the second. Yet the reason is the accuracy of the time measurement using a caesium atomic clock. The energy emitted by the transition between the two hyperfine levels is $3.8 \cdot 10^{-5}$ eV, corresponding to a wavelength of 32.6 mm, which lies in the microwave length. The best clocks of this type achieve a relative uncertainty in their time measurement in the order of 10^{-16} [Bur16, Par10, KLR⁺12].

However, a new type of atomic clock emitting light in the visible range has since been proposed, that may outperform caesium clocks by several orders of magnitude [ODD⁺06]. The major advantage of these optical clocks is that the atom can be fixed in the experiment, allowing for longer and more stable measurements [KLR⁺12]. In 2005, the Nobel Prize in Physics for theoretical and experimental work concerning optical lasers has been awarded to Roy J. Glauber, John L. Hall and Theodor W. Hänsch [Nobb], who opened up possibilities to build an optical atomic clock. Since then, a number of different atoms and techniques were studied to realize such a device. In principle, the first generation of atomic clocks consist of either single trapped ions or neutral atoms confined in an optical lattice [ODD⁺06].

With the former system, it was already possible to perform a time measurement with an uncertainty of $3 \cdot 10^{-18}$ [HSL+16].

Nonetheless, the accuracy might be improved even further. The isotope thorium-229 has a nuclear isomer state $^{229\text{m}}\text{Th}$ [vdWSL+16], which lies extremely close to the ground state (for a short discussion of isomer states, see section A.1). Recent measurements predict an energy difference of 7.8 ± 0.5 eV [BWB+09, BBB+07, KSS17, vdWSL+16], corresponding to a wavelength of approximately 160 nm, which is in the vacuum ultraviolet (VUV) region. This is by far the lowest ground-state doublet of all known nuclei [Des16, vdWSL+16]. In fact, the energy is in reach of modern optical laser spectroscopy methods and thus might be experimentally viable. It was suggested that this isomer could be used as an atomic clock of highest precision [PT03, PZOT08]. A particular advantage is that the clock is not based on an electronic but rather a nuclear transition and thus, the electron shell shields the core from external fields.

Additionally, confining $^{229\text{m}}\text{Th}$ in a lattice would have the tremendous advantage to work with a macroscopic number of thorium atoms, compared to only one in the ion trap. With this method, it is predicted that an unprecedented uncertainty level of 10^{-19} might be reached [KLR+12]. A critical component of the feasibility is that the host crystal should be transparent in the VUV region and therefore its band gap must exceed the predicted isomer energy.

In this work we simulated magnesium fluoride (MgF_2), a possible host to $^{229\text{m}}\text{Th}$, with the Vienna Ab-initio Simulation Package (VASP) [KH93, KH94, KF96b, KF96a, KJ99]. A summary of the theory behind VASP and its methods can be found in Chapter chapter 2. The results of the calculations are presented in chapter 3. For MgF_2 the electronic properties including the band structure and optical features were determined. When MgF_2 is doped with $^{229\text{m}}\text{Th}$, it was investigated which type of doping and which charge compensation is energetically favored. Finally it is demonstrated if and under which conditions the material is suitable for the construction of a new atomic clock. Possible applications and an outlook to other fields of research are discussed in chapter 4.

Chapter 2

Theory

2.1 Introduction

2.1.1 Schrödinger Equation

To describe properties that arise from quantum theory in any physical system, it is necessary to solve the Schrödinger equation

$$\frac{\partial}{\partial t} |\Psi\rangle = H |\Psi\rangle \quad (2.1)$$

to find a suitable wave function, which contains the full set of positions \mathbf{R} and spin variables σ of the particles of the system. Often it is sufficient to look at stationary states and thus rule out the time dependence of the Hamiltonian H , such that we are left with the eigenvalue problem

$$H |\Psi\rangle = E |\Psi\rangle. \quad (2.2)$$

The Hamiltonian H represents an operator for the total amount of energy in the system. To describe interactions between nuclei and electrons, we can construct H as [ED11]

$$H = T_n + V_{n-n} + H_e + (V_{n\text{-field}}), \quad (2.3)$$

where the index n refers to nuclei and the index e to electrons. The kinetic energy of the nuclei T_n is the sum over all K individual nuclei with mass M_α

$$T_n = \sum_{\alpha=1}^K \frac{(-i\hbar\nabla_{\mathbf{R}_\alpha})^2}{2M_\alpha}, \quad (2.4)$$

while the potential energy V_{n-n} is due to Coulomb forces and creates a correlation between all the nuclei

$$V_{n-n} = \sum_{\alpha,\beta=1;\alpha<\beta}^K \frac{Z_\alpha Z_\beta e^2}{|\mathbf{R}_\alpha - \mathbf{R}_\beta|}. \quad (2.5)$$

The Hamiltonian H_e for the electronic system can be split up into the following contributions

$$H_e = T_e + V_{n-e} + V_{e-e} + (V_{e\text{-field}}). \quad (2.6)$$

Likewise, the kinetic energy of the N electrons with mass m is

$$T_e = \sum_{a=1}^N \frac{(-i\hbar\nabla_a)^2}{2m}. \quad (2.7)$$

When describing chemical bonds between different atoms, the Coulomb force plays the dominant role. Besides the Coulomb attraction of the electrons and the nuclei

$$V_{n-e} = - \sum_{\alpha=1}^K \sum_{a=1}^N \frac{Z_\alpha e^2}{|\mathbf{R}_\alpha - \mathbf{r}_a|}, \quad (2.8)$$

there is also a repulsion between electrons

$$V_{e-e} = \sum_{a,b=1;a<b}^N \frac{e^2}{|\mathbf{r}_a - \mathbf{r}_b|}. \quad (2.9)$$

In the following work, the contributions to H in terms of external electric or magnetic fields V_{field} are not discussed.

In the context of the many different contributions to the Hamiltonian discussed earlier, with each of them making the problem more and more complicated, finding a solution for equation (2.2) is a very demanding task. For systems with more than two particles, an analytic solution is impossible to calculate. Even a numeric solution poses great difficulties for systems typically found in a solid state, due to the interaction of a large number of particles. It is thus necessary to look for suitable approximations. In a crystal for example, atoms are arranged in a lattice, which has distinct symmetries that are utilized to a high degree.

2.1.2 Band Gap

A particularly important property of an insulating material is the band gap Δ : When solving the Schrödinger equation for electrons on a crystal lattice, it turns out that due to translational symmetry there is an infinite number of wave functions $\Psi_a(\mathbf{k})$ and energy levels $E_a(\mathbf{k})$ that depend on the wave vector \mathbf{k} . These functions are commonly called energy bands. The distance between the highest energy below the Fermi level E_F and the lowest energy above the Fermi level is the band gap Δ . The bands above the Fermi level are the conduction bands, whereas the bands below the Fermi level are the valence bands. For metals there is no band gap and $\Delta = 0$, as opposed to insulators, where the gap can be large. When discussing band gaps, an important property is the density of states (DOS), which is the number of energy states per energy interval and thus an integrated quantity over the \mathbf{k} -dependent $E_a(\mathbf{k})$. Obviously, at the gap the DOS is zero, whereas the DOS obtains finite values for regions where bands exist.

The system of interest in this work is magnesium fluoride with the formula MgF_2 . It is an insulator and was measured to have a band gap of at least $\Delta = 10.8$ eV [BCA⁺11, AO, Rob79, SCLR69]. Thus, the band gap is large enough to be transparent for the $^{229\text{m}}\text{Th}$ transition energy.

Calculating the band gap Δ requires solving the Schrödinger equation (2.2), which turns out to be a huge effort for systems with a large number of particles as we have discussed in the previous subsection 2.1.1. In the following, we will introduce a theoretical approach that enables a numerical treatment of this problem. The Born-Oppenheimer approximation is the foundation of a big field of physics that considers the simulation of atomic systems and sets up the stage for all subsequent deliberations.

2.1.3 Born-Oppenheimer Approximation

First we choose an appropriate basis to write the abstract $|\Psi\rangle$ as a function depending on the nuclei positions \mathbf{R}_α , electron positions \mathbf{r}_i and the spin σ of the electrons. The time-independent Schrödinger equation (2.2) then has the form

$$\begin{aligned} H\Psi_a(\mathbf{R}_1, \dots, \mathbf{R}_K; \mathbf{r}_1\sigma_1, \dots, \mathbf{r}_N\sigma_N) = \\ E_a\Psi_a(\mathbf{R}_1, \dots, \mathbf{R}_K; \mathbf{r}_1\sigma_1, \dots, \mathbf{r}_N\sigma_N). \end{aligned} \quad (2.10)$$

We use a shorthand notation for the position and spin vectors

$$\begin{aligned} \mathbf{R}_1, \dots, \mathbf{R}_K &\equiv \mathbf{R} \\ \mathbf{r}_1\sigma_1, \dots, \mathbf{r}_N\sigma_N &\equiv \mathbf{r}\sigma \end{aligned} \quad (2.11)$$

to write the Schrödinger equation (2.10) as

$$H\Psi_a(\mathbf{R}; \mathbf{r}\sigma) = E_a\Psi_a(\mathbf{R}; \mathbf{r}\sigma) \quad (2.12)$$

Because the nuclei have significantly more mass than the electrons, they are a lot more inert. Due to this property, the electronic movement takes place on different timescales than the ionic movement. It is therefore a valid assumption to keep the positions of the ions fixed during an electronic relaxation and to separate the total wave function in an electronic part and an ionic part [BO27]

$$\Psi_a(\mathbf{R}, \mathbf{r}\sigma) \cong \Psi_a^n(\mathbf{R})\Psi_a^e(\mathbf{R}; \mathbf{r}\sigma). \quad (2.13)$$

Because the Schrödinger equation is linear, it is possible to calculate the electronic part separately from the nuclear part [MKE⁺]

$$H_e\Psi_a^e(\mathbf{R}; \mathbf{r}\sigma) = E_a^e(\mathbf{R})\Psi_a^e(\mathbf{R}; \mathbf{r}\sigma) \quad (2.14)$$

$$(T_N + V_{n-n} + E_a^e(\mathbf{R}))\Psi_a^n(\mathbf{R}) = E_a^n\Psi_a^n(\mathbf{R}). \quad (2.15)$$

This is the so-called Born-Oppenheimer approximation and serves as the foundation of all subsequent calculations. Since we can treat the electron and ionic movements separately, it is much more accessible to find appropriate simplifications. For example, quantum effects such as the Pauli

exclusion principle can be more easily considered when the electronic part is treated independently. Due to the strong localization of the ionic wave functions, it is even feasible to calculate their movement classically and therefore save a big amount of computing power. Obviously, every simplification has a drawback in accuracy for the calculation.

In the following [section 2.2](#), a selection of simplifications and its errors will be introduced and discussed. In [section 2.4](#) we will have a look at some of the computational tools available for the calculation of the problem depicted above. For an in-depth look of selected topics, [section A.2 – section A.4](#) will be referenced.

2.2 Density Functional Theory

2.2.1 Hartree-Fock Equations

Now that we have decoupled the ionic from the electronic movement we want to introduce a theory based on the simplifications suggested by generations of physicists for the many-body electron problem given by the electronic part of the Schrödinger equation (2.14). A starting point is the construction of an electronic wave function. It is a well known consequence of quantum theory that particles such as electrons are fermions and according to the Pauli exclusion principle, two fermions cannot occupy the same quantum state at the same time. When two electrons get close, they will experience an additional repulsive force, which will increase the total energy. This change in energy is commonly called exchange energy. Mathematically speaking, the wave function of fermions needs to be antisymmetric: When two electron coordinates are exchanged the sign of the wave function has to change as well [BPM14]. An elegant way to express this behavior is to use the properties of the determinant function since by swapping two rows or columns of a matrix the determinant function changes its sign as well. Therefore, we will write a matrix of single electron wave functions $\phi_i(\mathbf{r}_i, \sigma)$ and take the determinant to construct an arbitrary wave function for a many-electron system.

$$\Psi^e(\mathbf{r}\sigma) = \frac{1}{\sqrt{N!}} \begin{vmatrix} \phi_1(\mathbf{r}_1\sigma_1) & \cdots & \phi_1(\mathbf{r}_N\sigma_N) \\ \vdots & \ddots & \vdots \\ \phi_N(\mathbf{r}_1\sigma_1) & \cdots & \phi_N(\mathbf{r}_N\sigma_N) \end{vmatrix} \quad (2.16)$$

This wave function is called Slater determinant [Sla29] and ensures that the wave function is antisymmetric. The factor $1/\sqrt{N!}$ takes care of the appropriate normalization. Because section 2.2 is concerned with the electronic part of the Hamiltonian only, we will subsequently drop the index e , which would refer to an electron in contrast to the nucleus n . Now that we have constructed a wave function, we want to find the corresponding equations of motion. The Ritz method (see section A.2) states that we can write the energy as

$$E[\Psi] = \frac{\langle \Psi | H | \Psi \rangle}{\langle \Psi | \Psi \rangle}. \quad (2.17)$$

For this theorem it is not required for the wave function to be normalized. Alternatively, one can as well normalize the wave function with

$$|\tilde{\Psi}\rangle = \frac{1}{\sqrt{\langle\Psi|\Psi\rangle}} |\Psi\rangle. \quad (2.18)$$

Note that this is a rather general statement, so we have not written any indices and dependencies. Since the energy is a scalar value and takes the wave function as an input, we write it as a functional of Ψ (for an overview on the theory of functionals see [section A.3](#)). We seek a stationary solution of the energy functional with respect to a variation of the function Ψ

$$\frac{\delta E[\Psi]}{\delta(\langle\Psi|)} = 0. \quad (2.19)$$

The variation for the abstract bra and ket vectors can be treated by means of ordinary differential calculus [[Buron](#)]

$$\frac{\delta E[\Psi]}{\delta(\langle\Psi|)} = H \frac{1}{\langle\Psi|\Psi\rangle} |\Psi\rangle - \frac{\langle\Psi|H|\Psi\rangle}{\langle\Psi|\Psi\rangle} \frac{1}{\langle\Psi|\Psi\rangle} |\Psi\rangle = 0. \quad (2.20)$$

It follows quickly that

$$H |\tilde{\Psi}\rangle = E |\tilde{\Psi}\rangle, \quad (2.21)$$

which means we end up at the equations of motion of the system when calculating $\delta E = 0$. For the wave functions it makes sense to plug in the Slater determinant we have constructed earlier ([2.16](#)). It is important to note that expressing the wave function by a single Slater determinant is already an approximation in itself and forms the basis of Hartree-Fock theory. In more accurate models, a linear combination of Slater determinants has to be used.

Since we only deal with a single Slater determinant, correlation is not included. This means for an electron, that it moves freely in the electric field $v(\mathbf{r})$ produced from the other nuclei and electrons. After some calculation which we will not discuss in this work, we end up with the equations of motion, called the Hartree-Fock (HF) equations [[Cap02](#)]

$$\left[-\frac{\hbar^2}{2m} \nabla^2 + v(\mathbf{r}) \right] \phi_i^{HF}(\mathbf{r}) - e^2 \int d^3r' \frac{\gamma(\mathbf{r}, \mathbf{r}')}{|\mathbf{r} - \mathbf{r}'|} \phi_i^{HF}(\mathbf{r}') = E_i^{HF} \phi_i^{HF}(\mathbf{r}_i),$$

(2.22)

where $\gamma(\mathbf{r}, \mathbf{r}')$ is a density matrix. This equation is technically quite accurate. In fact, it accounts for the exchange energy exactly by definition. However, due to the simplifications made we are often left with an unsatisfactory result as a calculation can lead to a large deviation from experimental data. Additionally, the computational effort can be very demanding, since it is necessary to solve the Slater determinant as well as the $2N$ coupled integro-differential Hartree-Fock equations. However, the HF-equations still have an important role in the simulation of materials. Several approaches to include electron correlation to the wave function are collectively called post Hartree-Fock methods. In this work we will discuss the HF-equations again in [subsection 2.2.8](#) when we introduce the concept of Hybrid Functionals.

2.2.2 Hohenberg-Kohn Theorem

As we discussed, there are some practical problems when applying the HF-equations to a real system. Therefore, alternative ways to find a solution to the many-body Schrödinger equation have been found. At the heart of the highly successful and widely applied [[Giu14](#), [KH00](#), [Eug90](#)] *Density Functional Theory (DFT)* lies the Hohenberg-Kohn (HK) theorem, first proposed in 1964 [[HK64](#)]. The theorem proved to be so useful, that Walter Kohn was awarded the Nobel Prize in Chemistry in 1998 [[Noba](#)]. It states that [[BPM14](#), [Cap02](#)]:

- The ground state energy $E_{v,0}$ of a system of N identical particles in an external potential $v(\mathbf{r})$ can be expressed uniquely as a functional of the particle density $n(\mathbf{r})$, such that $E_{v,0} = E[n(\mathbf{r})]$.
- This functional has its minimum with respect to a variation $\delta n(\mathbf{r})$ of the particle density for the ground state density $n_0(\mathbf{r})$ for a given external potential.

A short summary of the variations of functionals can be found in [section A.3](#). Given a ground state density $n_0(\mathbf{r})$ it is therefore in principle possible to calculate the corresponding ground state wave function

$$\Psi_0(\mathbf{r}_1, \mathbf{r}_2, \dots, \mathbf{r}_N) = \Psi[n_0(\mathbf{r})] \quad (2.23)$$

and as a consequence, all ground state observables too

$$O_0 = O[n_0] = \langle \Psi[n_0] | O | \Psi[n_0] \rangle. \quad (2.24)$$

Additionally, if a particle density n is different from the ground-state density n_0 in a potential $v(\mathbf{r})$, then the wave functions Ψ that produce this n differ from the ground-state wave function Ψ_0 . The corresponding energy $E_v[n]$ will be, in accordance with the variational principle,

$$E_v[n_0] \leq E_v[n]. \quad (2.25)$$

2.2.3 Thomas-Fermi Theory

In the course of the HK-theorem, we express the energy of the system in its different contributions

$$E_v[n] = T[n] + V_{e-e}[n] + V_{n-e}[n] = T[n] + V_{e-e}[n] + \int n(\mathbf{r})v(\mathbf{r}) d^3r. \quad (2.26)$$

Beforehand, it is not clear what the functional form of these different parts will look like. To find suitable expressions, the greatest challenge is to find valid approximations. Starting with the most simple, we approximate $T[n]$ and $V_{e-e}[n]$ first. For $V_{e-e}[n]$ one can use the electrostatic repulsion of electrons with charge distribution $n(\mathbf{r})$

$$V_{e-e}[n] \approx V_{e-e}^H[n] = \frac{e^2}{2} \int d^3r \int d^3r' \frac{n(\mathbf{r})n(\mathbf{r}')}{|\mathbf{r} - \mathbf{r}'|}. \quad (2.27)$$

The approximation for the kinetic energy is done corresponding to the *Thomas-Fermi theory* [Tho27a, Tho27b]. Here, it is assumed that there are parts in space, where the kinetic energy density is that of a homogeneous and interacting system $t^{hom}(n(\mathbf{r}))$ with constant density n . Note that the use of lower case letters indicate a density, whereas an upper case letter represent the total amount of a quantity. This term is not known explicitly, so there is another approximation where the electrons are assumed to be non-interacting, denoted by the index s . This energy is known explicitly and it is $t_s^{hom}(n) = 3\hbar^2(3\pi^2)^{2/3}n^{5/3}/10m$. It is assumed, that these parts in

space are infinitesimally small such that an integral over all these regions yields the total kinetic energy.

$$T[n] \approx T^{LDA}[n] = \int d^3r t^{hom}(n(\mathbf{r})) \approx \int d^3r t_s^{hom}(n(\mathbf{r})) \quad (2.28)$$

2.2.4 Energy Functional

The Thomas-Fermi approximation for the kinetic energy has proven not to be very good but we can use the concept and try to improve the theory. It is instructive to separate $T[n]$ into two parts: One includes the kinetic energy of non-interacting electrons while the other one solely takes the correlations into account,

$$T[n] = T_s[n] + T_c[n]. \quad (2.29)$$

This time we write $T_s[n]$ in terms of single particle orbitals $\phi_i(\mathbf{r})$ such that

$$T_s[n] = -\frac{\hbar^2}{2m} \sum_i^N \int d^3r \phi_i^*(\mathbf{r}) \nabla^2 \phi_i(\mathbf{r}). \quad (2.30)$$

The exact energy functional is now

$$E[n] = T[n] + V_{e-e}[n] + V_{n-e}[n] = T_s[\{\phi_i[n]\}] + V_{e-e}^H[n] + E_{xc}[n] + V_{n-e}[n], \quad (2.31)$$

where $E_{xc}[n]$ contains the differences $T - T_s = T_c$ and $V_{e-e} - V_{e-e}^H = V_{e-e}^{xc}$. This *exchange-correlation* energy difference can also be decomposed to $E_{xc} = E_x + E_c$ where E_x is the exchange energy due to the Pauli principle and E_c is due to correlations. The advantage is now that we can write the exchange energy E_x explicitly as

$$E_x^{\text{HF}}[\{\phi_i[n]\}] = -\frac{e^2}{2} \sum_{jk} \int d^3r \int d^3r' \frac{\phi_j^*(\mathbf{r}) \phi_k^*(\mathbf{r}') \phi_j(\mathbf{r}') \phi_k(\mathbf{r})}{|\mathbf{r} - \mathbf{r}'|} \quad (2.32)$$

a result that can be found in the Hartree-Fock equations (2.22), but modified only in a way that the Hartree-Fock orbitals $\phi_i^{HF}(\mathbf{r})$ were substituted by Kohn-Sham orbitals $\phi_i(\mathbf{r})$, also called Fock-term. The Kohn-Sham orbitals are the solutions to the Kohn-Sham equations, which will be discussed in the next section.

For the correlation energy E_c a general expression is not known. There exist a number of different approaches on how to approximate E_c which can be found in reference [Cap02], but exceed the dimensions of this work.

However, it is instructive to look at the exchange-correlation energy E_{xc} further. To be precise, it shows a derivative discontinuity with respect to the total particle number,

$$\left. \frac{\delta E_{xc}[n]}{\delta n(\mathbf{r})} \right|_{N+\delta} - \left. \frac{\delta E_{xc}[n]}{\delta n(\mathbf{r})} \right|_{N-\delta} = v_{xc}^+(\mathbf{r}) - v_{xc}^-(\mathbf{r}) = \Delta_{xc}, \quad (2.33)$$

where δ is an infinitesimal small shift of the electron number N and Δ_{xc} is a shift of the exchange-correlation potential $v_{xc}(\mathbf{r})$. Furthermore, the non-interacting kinetic energy also exhibits this property

$$\left. \frac{\delta T_s[n]}{\delta n(\mathbf{r})} \right|_{N+\delta} - \left. \frac{\delta T_s[n]}{\delta n(\mathbf{r})} \right|_{N-\delta} = \varepsilon_{N+1} - \varepsilon_N = \Delta_{KS}, \quad (2.34)$$

where ε_{N+1} and ε_N are the single particle Kohn-Sham energy eigenvalues of the highest occupied and lowest unoccupied eigenstate. The energy gap Δ_{KS} is simply the single-particle energy difference between the HOMO (highest occupied molecular orbital) and LUMO (lowest unoccupied molecular orbital). It turns out that the fundamental energy gap, that is $\Delta = E(N+1) + E(N-1) - 2E(N)$, is the sum [SS83, ED11]

$$\Delta = \Delta_{KS} + \Delta_{xc} = \left. \frac{\delta E[n]}{\delta n(\mathbf{r})} \right|_{N+\delta} - \left. \frac{\delta E[n]}{\delta n(\mathbf{r})} \right|_{N-\delta}. \quad (2.35)$$

Speaking in this frame, the Thomas-Fermi theory or local density approximations generally predict $\Delta_{xc} = 0$ and thus estimate the energy gap to be too low as depicted in Figure 2.1.

So far, the energy functional $E_v[n]$ we have constructed in equation (2.31) is exact. In the big picture, the initial goal was to find an alternative way to the Thomas-Fermi theory. We will apply the HK-theorem again, but try a more sophisticated approach for the different contributions to the energy.

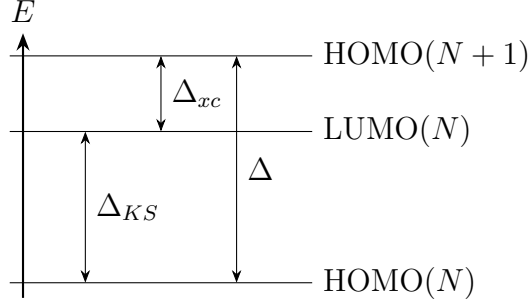


Figure 2.1: Schematic depiction of discussed energy eigenvalues.

2.2.5 Kohn-Sham Equations

The HK-theorem tells us that we find the ground state energy by minimizing the total energy with respect to the particle density. Using the exact energy functional (2.31) we get

$$\begin{aligned}
 0 &= \left. \frac{\delta E[n(\mathbf{r})]}{\delta n(\mathbf{r})} \right|_{n(\mathbf{r})=n_0(\mathbf{r})} \\
 &= \frac{\delta T_s[n]}{\delta n(\mathbf{r})} + \frac{\delta V_{n-e}[n]}{\delta n(\mathbf{r})} + \frac{\delta V_{e-e}^H[n]}{\delta n(\mathbf{r})} + \frac{\delta E_{xc}[n]}{\delta n(\mathbf{r})} \\
 &= \frac{\delta T_s[n]}{\delta n(\mathbf{r})} + v(\mathbf{r}) + v_H(\mathbf{r}) + v_{xc}(\mathbf{r}).
 \end{aligned} \tag{2.36}$$

Now we consider a system of non-interacting particles with energy $E_s[n]$, moving in a potential $v_s(\mathbf{r})$. For this problem, minimizing the energy results in

$$\begin{aligned}
 0 &= \left. \frac{\delta E_s[n(\mathbf{r})]}{\delta n(\mathbf{r})} \right|_{n(\mathbf{r})=n_0(\mathbf{r})} \\
 &= \frac{\delta T_s[n]}{\delta n(\mathbf{r})} + \frac{\delta V_s[n]}{\delta n(\mathbf{r})} \\
 &= \frac{\delta T_s[n]}{\delta n(\mathbf{r})} + v_s(\mathbf{r}).
 \end{aligned} \tag{2.37}$$

Comparing both equations, we see that it is possible to find the same solution if

$$v_s(\mathbf{r}) = v(\mathbf{r}) + v_H(\mathbf{r}) + v_{xc}(\mathbf{r}). \tag{2.38}$$

Thus it is possible to construct an auxiliary system which enables to find a solution to a single-particle Schrödinger equation

$$\left[-\frac{\hbar^2}{2m}\nabla^2 + v_s(\mathbf{r}) \right] \phi_i(\mathbf{r}) = \varepsilon_i \phi_i(\mathbf{r}), \quad (2.39)$$

which yields the same particle density n as the original system

$$n(\mathbf{r}) \equiv n_s(\mathbf{r}) = \sum_i^N f_i |\phi_i(\mathbf{r})|^2, \quad (2.40)$$

where f is the occupation number of the i 'th orbital. Equations (2.38) – (2.40) are the so-called Kohn-Sham equations. Essentially, they substitute the problem that arise when calculating many-body physics with a single-particle problem, just like mean-field theory. Because these equations are coupled in a non-linear way, they are usually solved by iteration also known as the self-consistency cycle. The procedure is as follows:

1. Making a guess for the particle density $n(\mathbf{r})$.
2. Calculating the corresponding single particle potential $v_s(\mathbf{r})$.
3. Solving the single particle Schrödinger equation (2.39).
4. Calculating a new particle density (2.40).
5. Repeat from step 2 until convergence is reached at $n_0(\mathbf{r})$.

The ground state energy can be found in the same way as we found the HF-energy (2.32). Using the different contributions to the energy it is possible to re-write the attraction of the nuclei and electrons as

$$\begin{aligned} V_{n-e}[n] &= \int d^3r v(\mathbf{r})n(\mathbf{r}) = \int d^3r [v_s(\mathbf{r}) - v_H(\mathbf{r}) - v_{xc}(\mathbf{r})]n(\mathbf{r}) \\ &= V_s[n] - \int d^3r [v_H(\mathbf{r}) + v_{xc}(\mathbf{r})]n(\mathbf{r}) \end{aligned} \quad (2.41)$$

and therefore, the ground state energy turns out to be

$$E_0 = \sum_i^N \varepsilon_i - \frac{e^2}{2} \int d^3r \int d^3r' \frac{n_0(\mathbf{r})n_0(\mathbf{r}')}{|\mathbf{r} - \mathbf{r}'|} - \int d^3r v_{xc}(\mathbf{r})n_0(\mathbf{r}) + E_{xc}[n_0].$$

(2.42)

2.2.6 Local Density Approximation

As we discussed earlier in [subsection 2.2.3](#), the LDA is inferior to the KS-theory when applied to the kinetic energy. However, it turns out that there is an application for it when applying LDA within the KS-equations. In particular, for $v_{xc}[n]$ a good approximation can be found.

For a homogeneous electron gas, the exchange energy is known exactly

$$e_x^{hom}(n) = -\frac{3e^2}{4} \left(\frac{3}{\pi}\right)^{1/3} n^{4/3} \quad \text{and} \quad (2.43)$$

$$E_x^{LDA}[n] = \int d^3r e_x^{hom}(n) = -\frac{3e^2}{4} \left(\frac{3}{\pi}\right)^{1/3} \int d^3r n(\mathbf{r})^{4/3},$$

where the change to a lower case letter again refers to a quantity per volume. The correlation energy proves to be a more complex subject and has to be studied on its own [[Cap02](#)]. As we have introduced in [subsection 2.2.3](#), independent of its approximation, the general way of LDA for the exchange-correlation energy consists of

$$E_{xc}[n] \approx E_{xc}^{LDA}[n] = \int d^3r e_{xc}^{hom}(n) \Big|_{n \rightarrow n(\mathbf{r})} = \int d^3r e_{xc}^{hom}(n(\mathbf{r})), \quad (2.44)$$

where $e_{xc}^{hom} = e_x^{hom} + e_c^{hom}$ with the corresponding potential

$$v_{xc}^{LDA}[n](\mathbf{r}) = \frac{\partial e_{xc}^{hom}(n)}{\partial n} \Big|_{n \rightarrow n(\mathbf{r})}. \quad (2.45)$$

The big advantage of implementing LDA in this particular way is that it performs strikingly well when doing calculations even for systems which are very much different from the reference frame of the electron liquid. The reason for it is that LDA usually overestimates E_x and underestimates E_c so that the sum yields good values and the errors cancel out. While this procedure is quite effective there have been a lot of efforts to increase the accuracy and improve the methods. In the following, we will briefly introduce two popular improvements: the Generalized Gradient Approximation (GGA) and Hybrid Functionals.

2.2.7 Generalized Gradient Approximation

In the LDA we approximate an inhomogeneous system with a locally homogeneous one. Therefore it would of course be instructive to not only take the particle density $n(\mathbf{r})$ into account, but also its variation in space $\nabla n(\mathbf{r})$. This is precisely the idea behind the Generalized Gradient Approximation. A GGA is therefore of the form

$$E_{xc}^{GGA} = \int d^3r f(n(\mathbf{r}), \nabla n(\mathbf{r})). \quad (2.46)$$

Different GGAs differ by their choice of $f(n, \nabla n)$. While there is only one LDA, there exist multiple forms of GGAs. The most popular and widely used GGAs are PBE [PBE96, XI04] (denoting the functional proposed by Perdew, Burke, Ernzerhof), which is fully expressed in section A.4 and BLYP [LYP88] (denoting the correction to Becke's functional by Lee, Yang and Parr). Recently, the Strongly Constrained and Appropriately Normed functional (SCAN) has been developed [SRP15], which obeys all 17 known constraints for a GGA. It has been confirmed to greatly enhance results obtained by the other GGA's at a comparable computational effort [SRZ⁺15, PYSP15, ZSPW17].

2.2.8 Hybrid Functionals

Although there are many sophisticated approaches in DFT, the approximations are subject to errors that can sometimes not be neglected [AG98]. Many theories were developed that go beyond LDA, like DFT + U or the *GW*-approach. In this section we shortly discuss a popular alternative, namely Hybrid Functionals.

The idea behind Hybrid Functionals is to use, in parts, the exact calculation of E_x as given by the HF-equations and then a combination of GGAs or LDAs to improve the result even further. A proper starting point is the adiabatic connection formula [Bec93a, Bec93b, PEB96]

$$E_{xc} = \int_0^1 d\lambda E_{xc,\lambda}, \quad (2.47)$$

where

$$E_{xc,\lambda} = \langle \Psi_\lambda | V_{ee} | \Psi_\lambda \rangle - \frac{e^2}{2} \int d^3r \int d^3r' \frac{n(\mathbf{r})n(\mathbf{r}')}{|\mathbf{r} - \mathbf{r}'|} \quad (2.48)$$

is λ^{-1} times the potential energy of exchange and correlation for electron – electron interaction $\lambda e^2/|\mathbf{r} - \mathbf{r}'|$ in a system whose external potential $v_\lambda(\mathbf{r})$ is adjusted to hold the electron density $n(\mathbf{r})$ fixed at its physical $\lambda = 1$ value. Ψ_λ is the ground-state wave function of this system. At $\lambda = 0$, the Kohn-Sham non-interacting system is recovered.

An obvious first approximation for the λ dependence of the integrand in equation (2.47) is a two-point approximation

$$E_{xc} = \frac{1}{2}E_{xc}^0 + \frac{1}{2}E_{xc}^1, \quad (2.49)$$

where the first term is the exchange-correlation potential energy of the non-interacting system, which is exactly known and the second term is the exchange correlation potential energy of the fully interacting real system, which can be approximated by LDA. Therefore, the idea is to mix exact Hartree-Fock exchange (2.32) and local density energies. The simplest such hybrid functional is [Phi]

$$E_{xc}^{hyb} = aE_x^{exact} + (1 - a)E_x^{GGA} + E_c^{GGA}, \quad (2.50)$$

where the constant a can be fitted or estimated theoretically.

A popular example that can improve the band gap is the HSE (Heyd-Scuseria-Ernzerhof) [HSE03] exchange-correlation functional

$$E_{xc}^{HSE} = aE_x^{HF,SR}(\omega) + (1 - a)E_x^{PBE,SR}(\omega) + E_x^{PBE,LR}(\omega) + E_c^{PBE}, \quad (2.51)$$

where SR and LR stand for "short range" and "long range" respectively, a is a mixing coefficient and ω is an adjustable parameter governing the extent of short-range interactions.

2.3 Ionic Movement

In the previous sections, we have discussed how to treat the electronic part of the Schrödinger equation (2.14). Naturally, that is only half of the picture because once the electronic movement is solved and a ground state has been found, the forces on the ions will need to be updated. In

this section, we will have a look at the atomic part of the Schrödinger equation (2.15).

As we have discussed in subsection 2.1.3, the main idea behind ab-initio molecular dynamics is the classical treatment of the ions. Instead of the Schrödinger equation, we will use Newton's second law for the equations of motion [Tuc02, Gro00, Laa13, MKE⁺]

$$M_\alpha \frac{d^2 \mathbf{R}_\alpha}{dt^2} = \mathbf{F}_\alpha(\mathbf{R}) \quad (2.52)$$

The force \mathbf{F}_α is expressed in terms of the electronic ground state and the ion-ion interaction

$$\mathbf{F}_\alpha(\mathbf{R}) = -\nabla_{\mathbf{R}_\alpha} (E^e(\mathbf{R}) + V_{n-n}(\mathbf{R})). \quad (2.53)$$

To determine the first term, we can e.g. use DFT to calculate $E^e(\mathbf{R}) = \min_\Psi \langle \Psi_0 | H_e(\mathbf{R}) | \Psi_0 \rangle$. Because the electronic ground state depends on the positions of the nuclei \mathbf{R} there needs to be an electronic relaxation as discussed in subsection 2.2.5 after each ionic step. In practice, this process is repeated iteratively until the forces (2.53) are minimized in a hopefully global minimum, such that

$$\mathbf{F}_\alpha(\mathbf{R}) \approx 0. \quad (2.54)$$

The classical treatment of the nuclei (2.52), together with using a GGA or a hybrid functional for the electronic part, makes it possible to simulate complex systems numerically. With computing power becoming exponentially better for the same price over the years [Wgs], there is rapid progress in the simulation of materials. While it was only possible to simulate simple unit cells several decades ago, calculations with systems including hundreds of atoms are nowadays standard procedure using modern parallel machines and specialized software. It is indeed a fascinating outlook, what will be possible in several decades from now.

In the next section, selected numerical methods required for the simulation will be introduced and their validity is discussed.

2.4 Methods

2.4.1 Basis Sets

To perform the calculations, in practice the Kohn-Sham orbitals are expanded in a suitable set of basis functions. VASP uses plane waves due to their periodicity which work well when there are periodic boundary conditions. Among other advantages is that the Fast Fourier transform can be done exceptionally efficient with plane waves. On the other hand, convergence is often slow and a high number of plane wave coefficients is required to describe the wave function especially when there are rapid oscillations as is the case near the ionic cores [MKE⁺]. To circumvent the problem of the strong oscillations near the cores pseudopotentials are introduced.

2.4.2 Pseudopotentials

The main idea behind pseudopotentials is that core electrons retain, to a good approximation, their original configuration in a many body formation such as a crystal. This means that it is feasible to treat the core electrons by means of an atomic calculation and consider the valence electron density n_v only. The core electrons are expressed in the external potential v_{ext}^{PP} such that the single particle potential becomes

$$v_s^{PP}[n_v] = v_{ext}^{PP} + v_H[n_v] + v_{xc}[n_v]. \quad (2.55)$$

The determination of v_{ext}^{PP} involves two steps: At first, one calculates in an auxiliary reference configuration an effective pseudopotential (PP) to find v_s^{PP} and then compares this to an all-electron KS calculation of the same atom outside a cutoff radius r_v , to see if the valence orbitals agree. If the particle densities in this region agree, we label them with n_v^{at} and continue to the next step. Now one subtracts the atomic valence contribution and the exchange-correlation potential from the single particle potential to obtain

$$v_{ext}^{PP} = v_s^{PP}[n_v^{at}] - v_H[n_v^{at}] - v_{xc}[n_v^{at}]. \quad (2.56)$$

This pseudopotential can then be used in the actual calculation, together with $v_H[n_v]$ and $v_{xc}[n_v]$ taken at proper valence densities for these systems [Cap02]. In principle, valence wavefunctions tend to have large

oscillations near the nuclei. The method of using a pseudopotential makes these regions more smooth, so that a lower number of Fourier components is needed. In VASP, the method of Projector Augmented Wave (PAW) pseudopotentials [Blö94] is implemented.

2.4.3 Brillouin Zone Sampling

There are many cases in DFT, where it is required to perform integrals in \mathbf{k} -space i.e. over the first Brillouin zone. When performing numerical integration the integration space has to be sampled on a grid and some summation rule has to be used. Similar to a Gaussian integration, a proper choice of the \mathbf{k} -points set, reduces the necessary sampling size. Often there are averages over the Brillouin zone with integrals of the type

$$\bar{f} = \frac{\Omega}{(2\pi)^3} \int_{\text{BZ}} f(\mathbf{k}) d^3k, \quad (2.57)$$

where $f(\mathbf{k})$ is a function that has the complete symmetry of the lattice. We can thus express the function in the form of a Fourier expansion as

$$f(\mathbf{k}) = f_0 + \sum_{m=1}^{\infty} f_m A_m(\mathbf{k}), \quad (2.58)$$

where

$$A_m(\mathbf{k}) = \sum_{|\mathbf{R}|=C_m} e^{i\mathbf{k}\mathbf{R}}, \quad m = 1, 2, \dots \quad (2.59)$$

The crucial idea is that if it was possible to find a vector \mathbf{k}_0 such that

$$A_m(\mathbf{k}_0) = 0, \quad m = 1, 2, \dots \quad (2.60)$$

we would immediately have [CC73]

$$\bar{f} = f_0 = f(\mathbf{k}_0). \quad (2.61)$$

Unfortunately, such a point does not in fact exist. The remedy is to impose other conditions on the points \mathbf{k}_i

$$\sum_{i=1}^N \alpha_i A_m(\mathbf{k}_i) = 0, \quad m = 1, 2, \dots, N, \quad (2.62)$$

where the α_i are weighting factors and satisfy

$$\sum_{i=1}^N \alpha_i = 1. \quad (2.63)$$

Combining equations (2.58), (2.62) and (2.63) the value of the integral is

$$f_0 = \sum_{i=1}^N \alpha_i f(\mathbf{k}_i) - \sum_m' \sum_i \alpha_i f_m A_m(\mathbf{k}_i), \quad (2.64)$$

where the prime indicates that the first m to appear is f_{N+1} . The expansion coefficients f_m normally drop rapidly when m becomes large, and by making N large enough and disregard the second term we have a good approximation [CC73]

$$f_0 = \sum_{i=1}^N \alpha_i f(\mathbf{k}_i). \quad (2.65)$$

Apparently the points \mathbf{k}_i exhibit the special property that the integration can be reduced to a small number of points. The method to find these points as implemented in VASP is the Monkhorst-Pack scheme [MP76]. The construction rule proposed is

$$\mathbf{k}_{prs} = u_p \mathbf{b}_1 + u_r \mathbf{b}_2 + u_s \mathbf{b}_3, \quad (2.66)$$

where

$$u_r = \frac{2r - q_r - 1}{2q_r}, \quad r = 1, 2, \dots, q_r. \quad (2.67)$$

Here, q_r is an integer that determines the number of special \mathbf{k} -points in the r -direction. This gives q^3 distinct points uniformly spaced in the BZ.

2.4.4 Smearing

Often, an integration has to be performed over the Brillouin zone over functions that are discontinuous at the Fermi level. This means that a high number of Fourier-components and therefore a dense grid are needed to accurately reproduce the integration numerically. Obviously such a task is computationally quite demanding. A possible way around this is known as *smearing*. Essentially, the discontinuity is replaced by a smoother function.

As an example, consider the occupancies of energy levels at a temperature T , which can be determined by the Fermi-Dirac Distribution $\bar{n}_i = (\exp [(E_i - \mu)/k_B T] + 1)^{-1}$. According to the Pauli principle, there is a sudden cutoff at the Fermi level, except when there is a non-zero temperature when the function changes from a step function to a smooth function. In a way, the denominator $k_B T = \tau$ can thus be seen as the smearing parameter

$$f^{\text{FD}} \left(\frac{E_i - \mu}{\tau} \right) = \frac{1}{\exp \left(\frac{E_i - \mu}{\tau} \right) + 1}. \quad (2.68)$$

Obviously, this is not the only possibility of how smearing can be done. Discontinuities of energy levels can also be smoothed out by a Gaussian function

$$f^{\text{G}} \left(\frac{E_i - \mu}{\tau} \right) = \frac{1}{2} \left[1 - \operatorname{erf} \left(\frac{E_i - \mu}{\tau} \right) \right]. \quad (2.69)$$

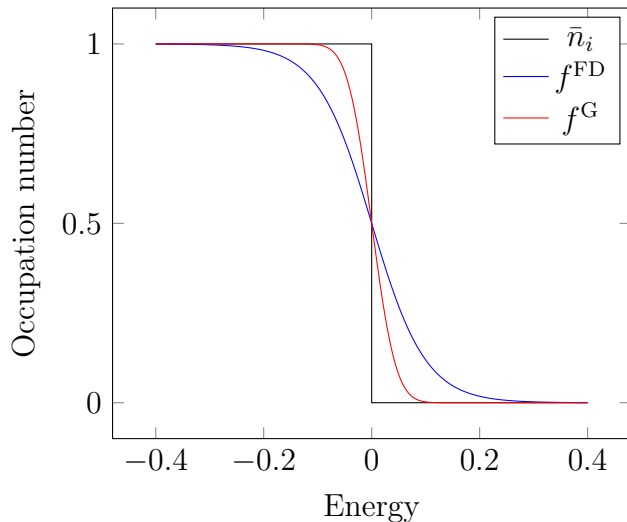


Figure 2.2: Different types of smearing with a smearing parameter $\tau = 0.05$. The black line represents the exact Fermi Dirac distribution, the blue and red lines are the smearing functions (2.68) and (2.69) respectively. For $T = 0$ the zero point on the energy scale is equivalent to the Fermi energy.

To circumvent the smearing method, an interpolation scheme between calculated \mathbf{k} -points is also possible. One example is the linear tetrahedron method [BJA94]. In this method, the \mathbf{k} -space is divided into tetrahedra and functions are interpolated inside them, removing the discontinuity. This scheme is in particular applicable to insulators and metals with a complicated shape of the Fermi surface.

2.4.5 Differential Equations

VASP uses a variety of algorithms to solve the differential equations that arise with ionic relaxations. One of them is called the Direct Inversion in the Iterative Subspace (DIIS) [SM07] scheme. This illustrates the procedure for descent algorithms.

In DIIS the minimization scheme not only considers the current steepest descent of the function to minimize, but also mixes the information of all previous steps, which is also known as Pulay-mixing. Consider the real minimum to be at \mathbf{x}_0 .

1. The starting position of the iteration is labeled with \mathbf{x}_1 . For the first iteration, we move along the gradient $\mathbf{g}_1 = \partial f / \partial \mathbf{x}_1$ and find the next point $\mathbf{x}_2 = \mathbf{x}_1 - \lambda \mathbf{g}_1$.

2. Now, we construct an optimal gradient \mathbf{g}_{opt} , which contains all the information from the previous gradients $\{\mathbf{g}_1, \mathbf{g}_2, \dots, \mathbf{g}_N\}$ multiplied by weighting coefficients $\sum_{i=1}^N \alpha_i = 1$

$$\mathbf{g}_{\text{opt}} = \sum_{i=1}^N \alpha_i \mathbf{g}_i. \quad (2.70)$$

The coefficients will be chosen such that the \mathbf{g}_{opt} is minimized. The corresponding position vector is then

$$\mathbf{x}_{\text{opt}} = \sum_{i=1}^N \alpha_i \mathbf{x}_i \quad (2.71)$$

3. Now the next point in the iteration is calculated by moving from \mathbf{x}_{opt} along the gradient \mathbf{g}_{opt} , such that $\mathbf{x}_3 = \mathbf{x}_{\text{opt}} - \lambda \mathbf{g}_{\text{opt}}$ [MKE⁺].

This method can greatly improve the convergence speed [RS11] over simple steepest descent methods, where in principle one repeats step number 1 from the DIIS scheme.

Other possibilities for the minimization procedure are the conjugate gradient algorithm and damped molecular dynamics. The former is concerned with finding a set of vectors \mathbf{s}_i , which are conjugate with respect to the Hessian matrix, i.e. $\mathbf{s}_i B \mathbf{s}_j = \delta_{ij}$, where B is defined as the Hessian matrix of the function to minimize $f(\mathbf{x}) = \mathbf{a} + \frac{1}{2}(\mathbf{x} - \mathbf{x}_0)B(\mathbf{x} - \mathbf{x}_0)$. The main idea is to minimize the function along the direction of \mathbf{s}_i , instead of going along \mathbf{g}_{opt} in DIIS. In damped molecular dynamics, the Forces are not minimized using a procedure like in DIIS or CG, but rather seen as accelerations and an additional friction term is introduced. In that sense, the position \mathbf{x}_i is rolling with friction in the potential towards the minimum [MKE⁺].

Chapter 3

Results

The results were obtained with VASP versions 5.4.1. and 5.4.3. In VASP, there are four files required, which set the input parameters for the calculations:

- **INCAR:** This file handles the most important flags for the calculation, i.e. which algorithm will be used, what the precision is, etc.
- **POSCAR:** The initial positions of the ions are set in this file.
- **KPOINTS:** The mesh in \mathbf{k} -space will be generated according to the flags set in the KPOINTS file.
- **POTCAR:** This file does not handle any input parameters but it contains the pseudopotentials for each element.

3.1 Convergence Studies

Before starting the actual calculations, it is crucial to determine the input flags for VASP accordingly. On the one hand, values such as the energy cutoff of the plane wave basis should be large enough to simulate the physical reality accordingly and on the other hand they should not be too large or otherwise the performance will be severely slowed down.

3.1.1 Cutoff Convergence

The energy cutoff determines the maximum energy VASP uses for the plane wave basis set. It can be controlled by the flag **ENCUT** in the **INCAR**

file. The value should be chosen large enough to yield accurate results, but alas the computational demand scales heavily with this value. As a rule of thumb, it is recommended to set it higher than the maximum cutoff `ENMAX` used for the computation of the pseudopotential found in the `POTCAR` file for good results.

In this case the highest `ENMAX` was from the fluorine potential (dated April 8th, 2002) with a value of 400 eV. Eventually, the cutoff `ENCUT` was chosen to be 450 eV after some additional analysis (see [Figure 3.1](#)).

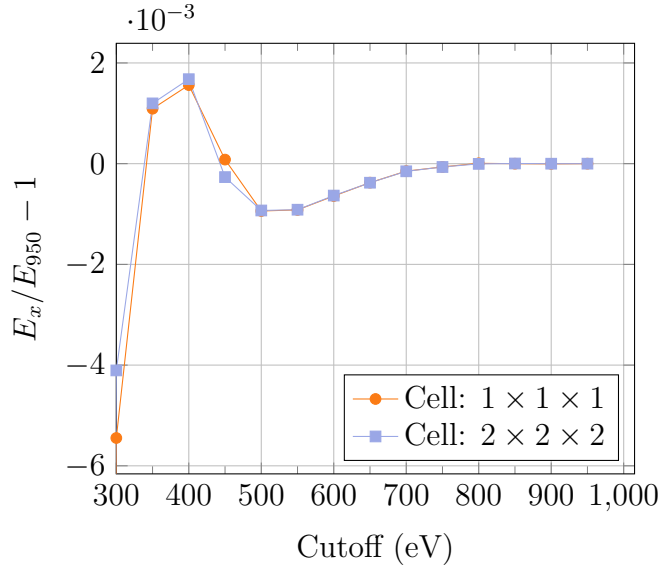


[Figure 3.1](#): The parameter `ENCUT` varies the cutoff energy for the plane wave basis set and can be seen on the x-axis. On the y-axis the energy quotient between the current cutoff and the maximum cutoff investigated at 950 eV was determined. The calculation was iterated for a $1 \times 1 \times 1$ and a $2 \times 2 \times 2$ unit cell respectively. A relative convergence in the order of 10^{-3} is already viable and additionally both curves exhibit a remarkably close value of the final energy at a cutoff 450 eV. Because both curves are very similar in their functional form, it can be assumed that the cutoff chosen is sufficient even for larger cells.

3.1.2 k-Space Mesh

Sampling the Brillouin-zone with a right mesh can significantly improve the calculation speed. All meshes in the following were generated using the Monkhorst-Pack scheme [[MP76](#)]. Different cell sizes were also investigated.

Note that the volume of the Brillouin zone V_Ω reduces in size compared to the volume of the primitive cell V_c with the relation

$$V_\Omega \propto \frac{1}{V_c}. \quad (3.1)$$

Thus, the number of points in \mathbf{k} -space needed to make an accurate calculation reduces when the volume of the primitive unit cell increases. For large supercells, it can even be sufficient to consider the Γ -Point (i.e. the origin) only. When having such a system, the calculation simplifies and the computational time needed will reduce greatly. In this case, all simulations with $4 \times 4 \times 4$ unit cells were performed with only the Γ -point (see [Figure 3.2](#)) after some additional verification as will be shown in [subsection 3.6.2](#).

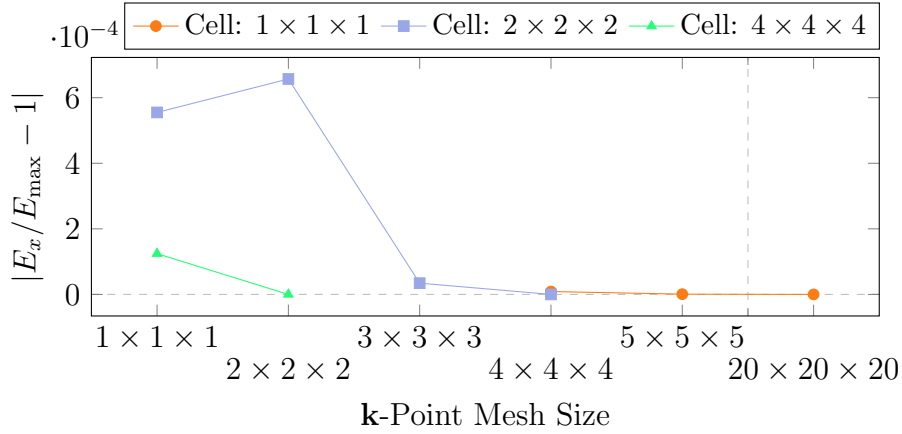
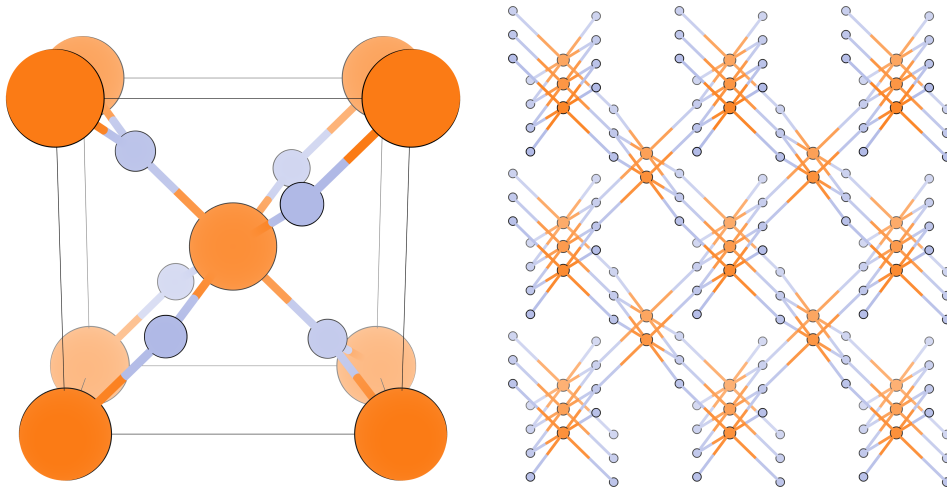


Figure 3.2: The energies were compared for different mesh sizes of the Monkhorst-Pack [MP76] scheme in reciprocal space. The orange dots represent a $1 \times 1 \times 1$ unit cell of MgF_2 . For this cell, a reference calculation with a large amount of points in \mathbf{k} -space has been performed. Note the discontinuity in the x-axis marked by the dashed vertical line $5 \times 5 \times 5$ followed by $20 \times 20 \times 20$. There is almost no difference compared to smaller grid sizes. The blue squares try to find the right grid size for a $2 \times 2 \times 2$ unit cell. There is a sudden change in accuracy for the $3 \times 3 \times 3$ Monkhorst-Pack mesh, which is why this value was chosen for the calculations. The green triangles account for a $4 \times 4 \times 4$ super cell of thorium doped MgF_2 . Since a Γ -only calculation saves a lot of computation time, it was important to determine if the sampling is not too small (see [subsection 3.6.2](#)).

3.2 Structure

The material MgF_2 exhibits an exceptionally wide transparency range from a few μm into the VUV region. It crystallizes into a simple tetragonal cell [JAG76, AO] with a rutile structure (see Figure 3.3) [Rob79]. Its melting point is at about 1535 K [CTT97].



(a) The unit cell of MgF_2 is depicted. In total, it consists of 2 magnesium and 4 fluorine atoms. (b) This $2 \times 2 \times 2$ super cell makes it possible to see the periodicity of the crystal structure more easily.

Figure 3.3: Visual depiction of the structure of MgF_2 . The coloring was chosen such that magnesium is displayed in orange and fluorine in a faint blue. All figures in this work that depict lattice structures were made with the software VESTA [MI11].

The lattice vectors were obtained by performing a volume scan and considering the minimum for the energy. To do so, each of the lattice vectors was varied and subsequently, the energy was fitted in terms of a quadratic function in accordance with Hooke's law

$$f(x; A, B, x_0) = A (x - x_0)^2 + B, \quad (3.2)$$

where A, B and x_0 are the fit parameters, with x_0 being the minimum of the lattice vector length. This process was done iteratively until a convergence was reached. The results are shown in Table 3.1.

Lattice Vector	VASP	Expt[Bau76]	Expt[AO]
$\mathbf{a} = \mathbf{b}$ (Å)	4.70	4.62	4.64
\mathbf{c} (Å)	3.10	3.05	3.06

Table 3.1: This table contains the calculated lattice parameters and a comparison of experimental values. Here VASP estimates the vectors to be larger than in the experiment, but the average relative increase is only 1.5%.

3.3 Electronic Configuration

The band structure for MgF_2 was determined using a variety of different functionals. A comparison of the results for the band gap can be found in Figure 3.4. The band structures determined can be found in Figure 3.5.

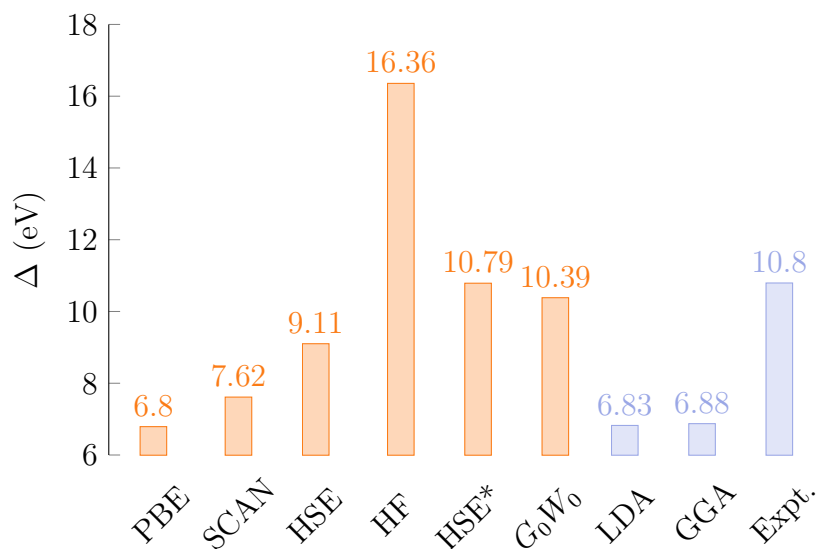


Figure 3.4: In orange, the band gaps Δ calculated with different functionals are depicted. In faint blue are reference values [BCA⁺11]. It is evident, that for the PBE functional the band gap is underestimated. SCAN shows a small improvement and lies directly between PBE and HSE. As expected, the full Hartree-Fock calculation overestimates the experimental value [AG98]. Thus, the mixing was adjusted denoted by the star * for the HSE functional (see Figure 3.6) to fit the experimental value. The closest value to the experiment without any tweaking is provided by G_0W_0 [AG98].

3.3.1 Band Structure

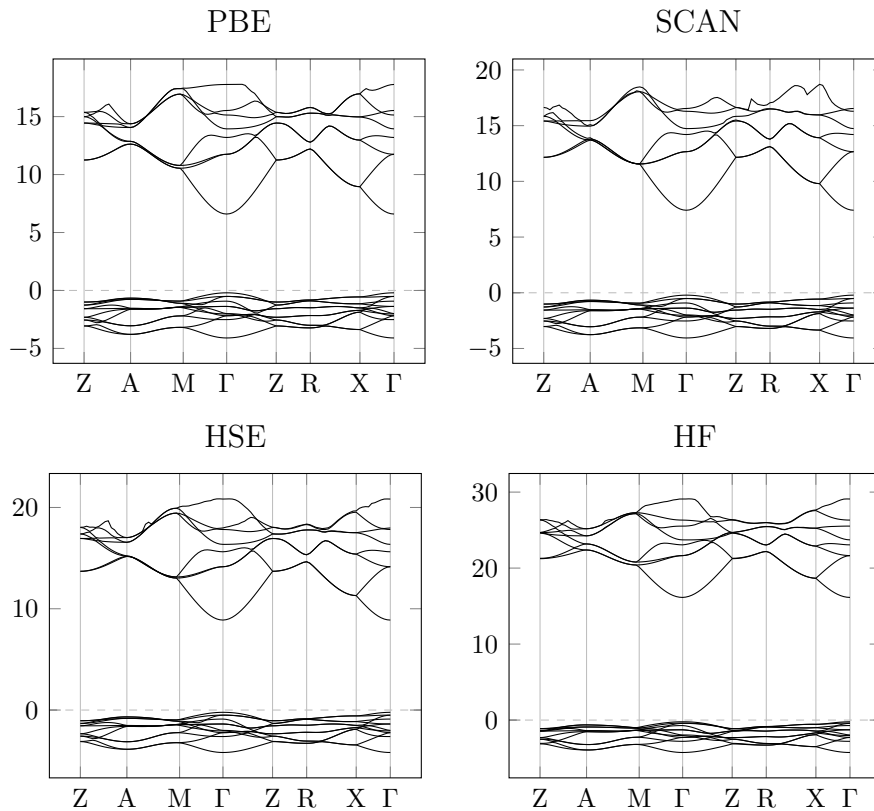


Figure 3.5: The band structure of different functionals was compared. On the x-axis is the \mathbf{k} -vector distance, on the y-axis the energy eigenvalue. The functional form of the bands did not change much when using different functionals, especially in the region near the gap and for the first excited states.

The HSE functional includes a mixing parameter for the exact Hartree-Fock correlation amount. As is shown in [Figure 3.4](#), a pure Hartree-Fock calculation overestimates the band gap and thus, this mixing parameter can be increased to fit the result to the experimental data (see [Figure 3.6](#)).

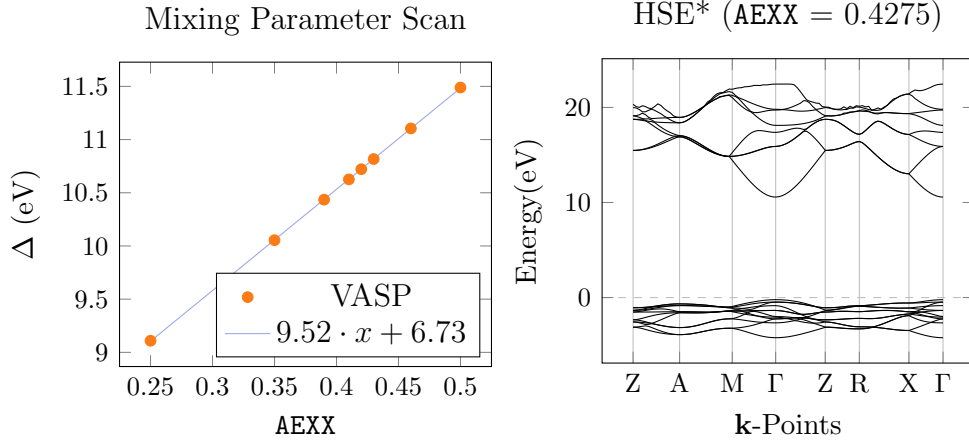


Figure 3.6: On the left side, the band gap Δ was determined with HSE calculations when the mixing parameter for Hartree-Fock type interactions was varied. In VASP, this mixing parameter is controlled by the flag `AEXX` in the `INCAR` file. The resulting values (orange dots) have a surprisingly strong linear dependence and were fitted accordingly (blue line). Using this fit, an optimal value for the mixing of `AEXX = 0.4275` was determined to match the experimental value [BCA⁺11]. On the right side, the band structure was evaluated for the HSE functional with exactly this mixing, denoted by HSE*. The resulting band gap turned out to be $\Delta = 10.794$ eV.

3.3.2 Density Of States

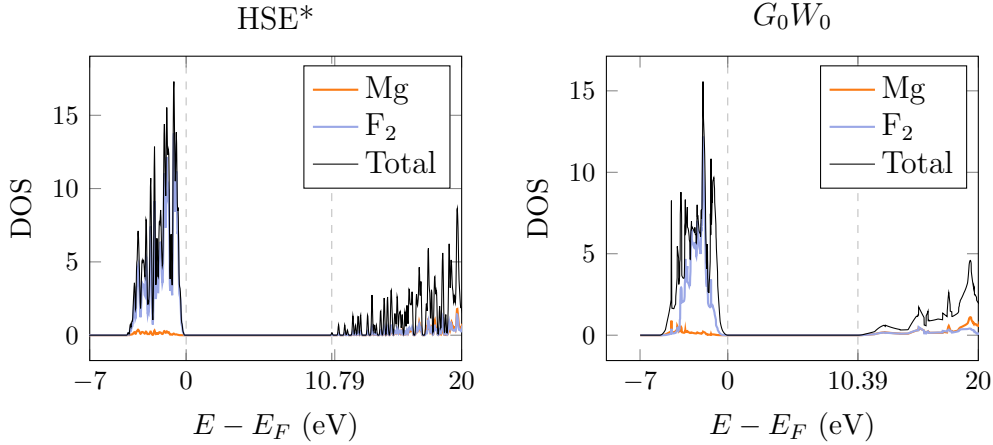


Figure 3.7: The density of states is compared for two cases. On the left side, the calculation was done using the HSE potential with an adjusted mixing parameter for HSE (see [Figure 3.6](#)) and on the right side the calculation was done with G_0W_0 . The band gap is highlighted by the dashed lines. The functional form is roughly similar. Note that the number of points \mathbf{k} -points for the G_0W_0 calculation is smaller and the smearing parameter was chosen to be larger. At the lower end of the gap, almost all of the states are populated by fluorine electrons.

3.4 Optical Studies

Optical properties are interesting to study as well. In this section we examine the dielectric tensor (for a short review, see [section A.5](#)) in two ways: One calculation was done with the PBE functional. For better results in optical studies it is often required to include well calculated excited states, which is beyond the reach of PBE. Therefore, the GW -approach with the Random Phase Approximation (RPA) was used. The approach is similar to the HF-approach, as discussed in [subsection 2.2.1](#), but the major difference is that the Coulomb interaction is dynamically screened. For a certain number of cases, this can lower the band gap compared to a pure HF-calculation and improve the results. Indeed, the GW approach is quite sophisticated and exceeds the scope of this work. For a short description of the approach see reference [[AG98](#)].

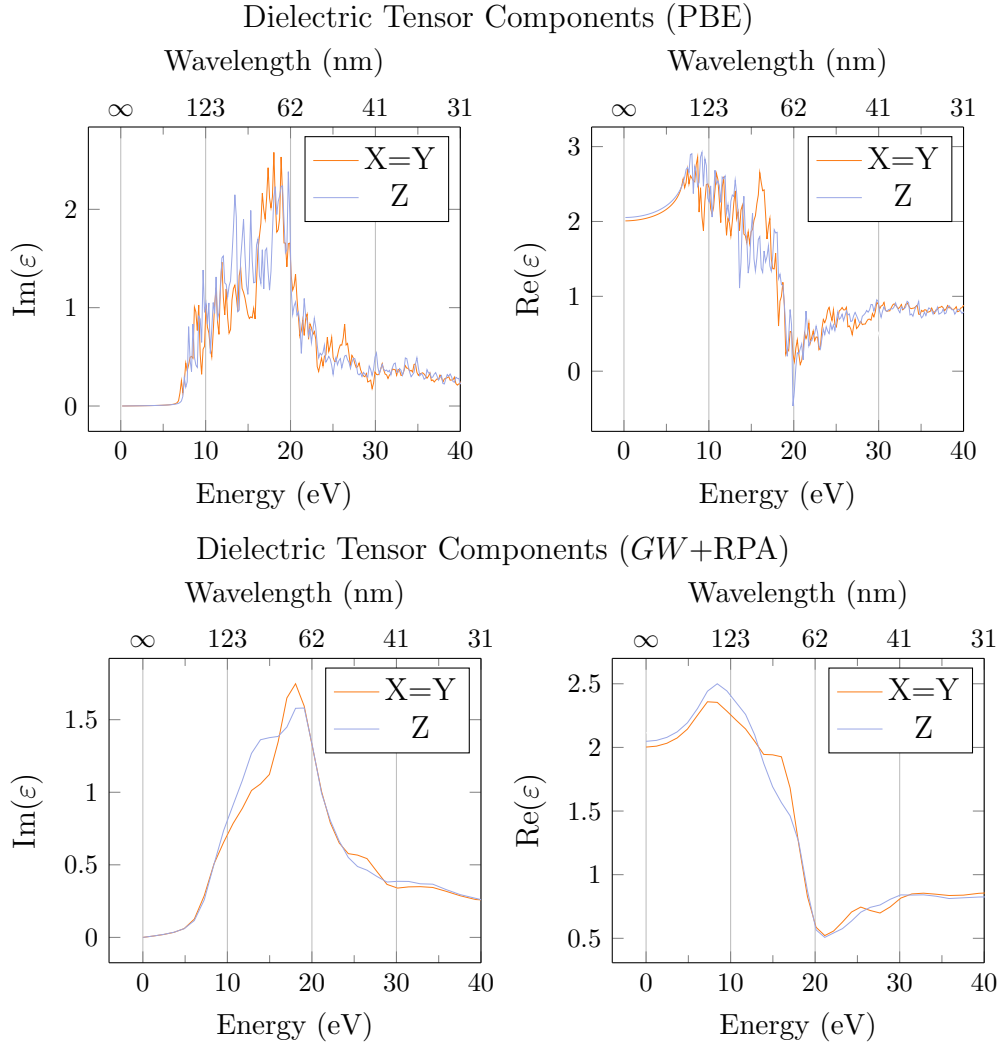
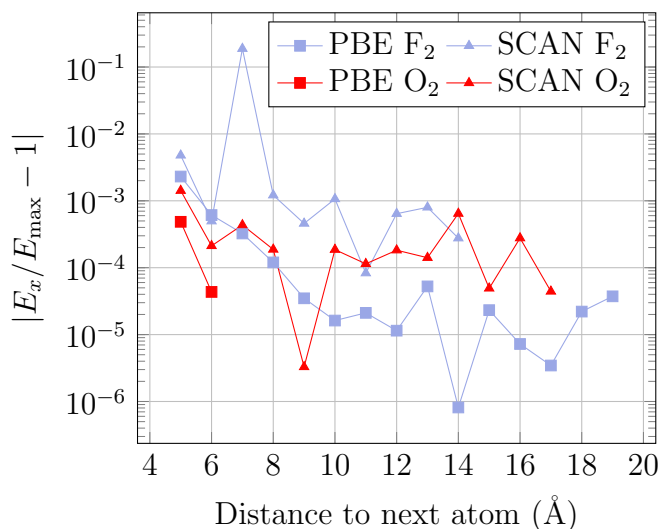


Figure 3.8: The optical properties of MgF_2 were studied using the PBE functional and the RPA within the GW -approach. The plots on the left side depict the imaginary part of the diagonal elements of the dielectric tensor, while the right side show the real part. The crystal exhibits two optical axes, due to the symmetry. Off-diagonal elements of the tensor were nearly zero and thus not shown in this plot. Remarkably, PBE shows a similar result in the energy range shown. Since the computational effort increases greatly for GW , the energy sampling was much lower and as a consequence the curve is smoothed.

3.5 Total Energies

To compare different configurations it is required that the systems consist of the same particles to take all energy contributions into account. Therefore, the energies of F_2 and O_2 in the gas phase were calculated because they are either ejected and go into the gas phase or get stored in the bulk during the formation of the crystal due to charge compensation (for possible charge compensations, see [subsection 3.7.1](#)).

It is possible to calculate the energies of gases in VASP by setting the lattice constant in the POSCAR file to a very high value, such that interactions between the different unit cells can be neglected. To test if this is really the case, the lattice constant was varied up to very high lengths as shown in [Figure 3.9](#).



[Figure 3.9](#): This figure shows the change in energy when the size of the unit cell containing only one molecule is increased. The calculations were performed with PBE and SCAN. Note that the y-axis is logarithmic and thus the reference value E_{\max} for a set of calculations cannot be shown in this plot. It is safe to assume that the interaction between two unit cells becomes negligible for all systems at about 8 Å.

For Mg it was assumed that it will stay in the bulk. The final values for the total energies for different functionals are shown in [Table 3.2](#).

	Element	Energy (eV)		
		PBE	SCAN	HSE
Gas	F ₂	-3.563800	-5.26599	-4.75428
	O ₂	-9.85702	-12.16702	-13.51708
Bulk	Mg	-2.72891	-9.08088	-2.34225
	Th	-7.344270	-95.716845	-8.809780
	MgF ₂	-31.47584	-46.95527	-38.44715

Table 3.2: This table summarizes the total energies of the elements needed for the charge compensation. As a reference, the bulk energy of MgF₂ can be found in the last row. For the calculation of the molecules the gas phase, the distance to the next atoms were determined as demonstrated in [Figure 3.9](#).

Usually, binding energy is released when the crystal forms, which is also called heat (or enthalpy) of formation (HoF). To validate the results obtained for the individual atoms, the heat of formation for MgF₂ was compared with experimental data, as shown in [Table 3.3](#).

	Functional			Expt.[Cha98]
	PBE	SCAN	HSE	
HoF (eV)	10.8	13.67	13.30	11.69

Table 3.3: The heat of formation (HoF) of magnesium fluoride is compared with an experimental value. While PBE is slightly below, SCAN and HSE overestimate the energy. Remarkably, SCAN and HSE yield almost the same value.

3.6 Doping

Now, the thorium atom will be introduced as a dopant. Doping can essentially take place in one of two ways (see [Figure 3.10](#)):

- (a) Substitutional Doping: The dopant will replace an atom of the original lattice and thus sits on one of the lattice sites.
- (b) Interstitial Doping: The dopant will sit in a position in between the other atoms.

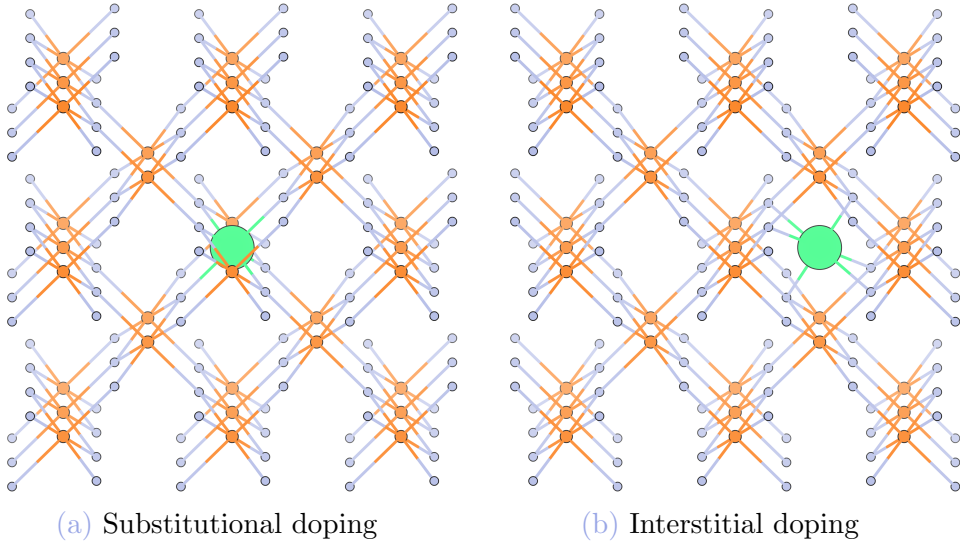


Figure 3.10: The two different types of doping are depicted. The introduced thorium is shown in a green color and its size is exaggerated for demonstrative purposes.

Doping Type	Total Energy (eV)
Substitutional	-2014.8757
Interstitial	-2011.6581

Table 3.4: This table compares the energy difference of substitutional and interstitial doping in a $4 \times 4 \times 4$ unit cell of MgF_2 with Th doping. The energy difference between the two doping types is $\Delta E = 3.22$ eV. Calculations were performed with the PBE functional.

As we can see in Table 3.4, substitutional doping is energetically preferred. Still, external parameters such as temperature might still make it possible that an energetically adverse configuration is created. It is possible to determine the probability that this is the case by means of statistical physics. Let P_I and P_S be the probability that interstitial or substitutional doping is realized respectively. Its quotient can be calculated with $P_I/P_S = \exp(-\Delta E/(k_B T))$. As an example, at $T = 300$ K and an energy difference $\Delta E = 3.22$ eV taken from Table 3.4 it follows that

$$\frac{P_I}{P_S} = e^{-\frac{\Delta E}{k_B T}} = 6.27 \cdot 10^{-55}. \quad (3.3)$$

Therefore, interstitial doping will be almost certainly never realized.

3.6.1 Cell Size

Next, it was determined how large the super cell size will have to be chosen. When thorium is implanted in the crystal, it will shift atoms in the near vicinity. In the experiment, the concentration of thorium atoms is severely lower than what is possible to simulate on a computer. It is crucial that the cell is chosen large enough such that the natural periodicity of the crystal is restored at the border of the unit cell, which is centered at the thorium atom (i.e. the atoms at the borders do not "feel" the thorium atom), to get as close as possible to the experiment.

Unfortunately, increasing the volume of the unit cell and therefore the number of atoms has an enormous impact on the computation time. The largest unit cell investigated was a $5 \times 5 \times 5$ super cell with 750 atoms. The results are shown in [Figure 3.11](#).

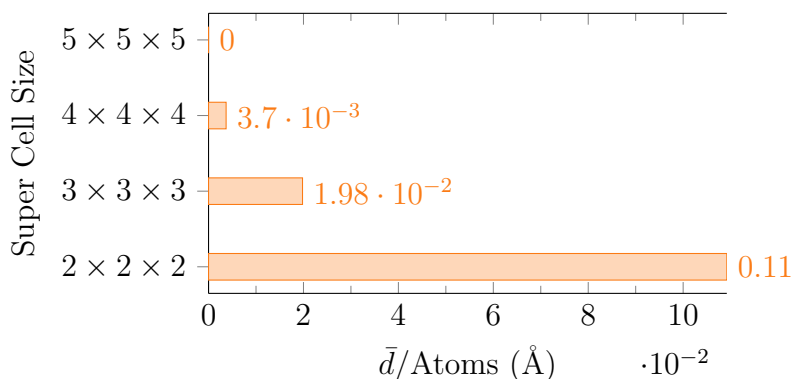


[Figure 3.11](#): The shift of atoms in the area around the central thorium atom was compared for different unit cell sizes. It was determined by investigating atoms in a sphere around Th with a diameter of 3.11 \AA and then looking at their average displacement compared to the $5 \times 5 \times 5$ super cell. Because the average displacement was quite small for the $4 \times 4 \times 4$ super cell with 384 atoms, it was the system of choice for all subsequent calculations.

With all forms of iterative relaxations, it can happen that somehow the calculation converged at a local minimum, rather than the global minimum. We rule out this possibility by displacing the thorium atom slightly and then checking if it converges back into its initial position (see [Table 3.5](#)).

Starting Position	$\Delta\bar{d}/\text{Atom}$ (Å)	Energy (eV)
At Minimum	0.0037	-2014.8757
Displaced	0.013	-2014.8757

Table 3.5: The thorium atom was displaced in each direction by 1 % of the cell size corresponding to 0.3 Å and the effects are presented in this table. Atoms around Th shifted a little bit more but the energy stayed the same. Additionally, the Th atom moved back into its initial position. Therefore, it is confirmed, that the positions are not a local minimum but rather a global one.

3.6.2 Γ -only k-mesh

As discussed in [subsection 3.1.2](#), there is a possibility for a big decrease in computing time, when it is valid to use a single \mathbf{k} -point to sample the whole Brillouin-zone, located at the Γ -point. The results of this analysis are discussed in [Table 3.6](#).

	KPoint-Mesh	
	$2 \times 2 \times 2$	$1 \times 1 \times 1$
CPU Time (h):	23.3	3.3
Energy/Atom (eV):	-5.24697	-5.24762
$\Delta\bar{d}/\text{Atom}$ (Å):	0.0037	0.017

Table 3.6: In this table we discuss the validity of using a single \mathbf{k} -Point at Γ for the calculation of $4 \times 4 \times 4$ super cells. The system analyzed is MgF_2 with substitutional doping of Th and the PBE functional was used. Remarkably, the CPU time required is about seven times lower than for the bigger cell. Since the energy difference per atom is $\Delta E = 6.523 \cdot 10^{-4}$ eV and the shift of atoms around the center gets larger by $\Delta\bar{d} = 1.33 \cdot 10^{-2}$ Å the resulting error is negligible. All subsequent calculations of $4 \times 4 \times 4$ super cells were done with a single point in \mathbf{k} -space at Γ and the SCAN functional.

3.7 Charge Compensation

3.7.1 Overview

Thorium has an oxidation number of +4. As we have found in [Table 3.4](#), it will replace a Mg atom, which has an oxidation number of +2. Therefore, two electrons will be available to form bonds with some other atoms which will be located in the vicinity of the defect.

Practically, there are four possibilities on how this compensation can take place.

(a) 1 Interstitial Oxygen:

An additional oxygen (oxidation number -2) atom will rest somewhere in between the lattice sites.

(b) 2 Substitutional Oxygen:

Oxygen can replace two fluorine atoms, which have an oxidation number of -1 .

(c) 2 Interstitial Fluorine:

The two charge compensation atoms can as well be two fluorine sitting in between the lattice sites. The positions can be assumed to be similar to the interstitial oxygen atoms due to the shape of the lattice.

(d) 1 Vacancy of Magnesium:

The oxidation number of magnesium is +2 and therefore it is also possible that one magnesium atom will be removed from the lattice.

An overview of the calculations done for the different types of charge compensations can be found in [Table 3.7](#).

#	Position	$E_{\max} - E$ (eV)			Δ (eV)		
		20	10	0	4	6	8
+1 O (int.):							
1	{0.5, 1, 0.5}	6.86				5.43	
2	{0.85, 0.85, 0.5}	6.31				5.42	
3	{0.3, 0.7, 1}	7.29				5.09	
4	{1, 1.5, 0.5}	8.44				3.26	
+2 O (subs.):							
5	{0.7, 0.7, 0}, {0.7, 0.7, 1}	13.68				5.7	
6	{0.2, 0.8, 0.5}, {0.7, 0.7, 1}	11.25				5.53	
7	{0.3, 0.3, 0}, {0.7, 0.7, 1}	14.26				4.77	
8	{0.3, 0.3, 1}, {0.7, 0.7, 1}	13.64				5.82	
+2 F (int.):							
9	{0.5, 1, 0.5}, {0.5, 0, 0.5}		0.88			6.48	
10	{0.5, 1, 0.5}, {1, 0.5, 0.5}		1.06			6.46	
11	{0.15, 0.15, 0.5}, {0.85, 0.85, 0.5}		1.85			6.37	
12	{0.3, 0.7, 0}, {0.3, 0.7, 1}		2.37			5.85	
13	{0.7, 0.3, 1}, {0.3, 0.7, 1}		1.71			6.31	

















14	$\{0.7, 0.3, 0\},$ $\{0.3, 0.7, 1\}$	1.52		5.91
15	$\{0.15, 0.15, 0.5\},$ $\{0.5, 1, 0.5\}$	0.87		6.4
16	$\{0.3, 0.7, 1\},$ $\{0.5, 1, 0.5\}$	0.78		6.06
17	$\{0.15, 0.15, 0.5\},$ $\{0.3, 0.7, 1\}$	0.52		5.93
18	$\{0.5, 1, 0\},$ $\{0.5, 1, 1\}$	0.59		6.76
19	$\{0.5, 0, 0\},$ $\{0.5, 1, 1\}$	0		6.51
20	$\{0.5, 1, 1\},$ $\{0.5, 0, 1\}$	$1.04 \cdot 10^{-2}$		6.6
21	$\{0.5, 1, 1\},$ $\{1, 0.5, 1\}$	0.4		6.41
22	$\{0.5, 1, 1\},$ $\{1, 0.5, 0\}$	0.12		6.81
23	$\{0.5, 1, 1.5\},$ $\{0.5, 1.5, -0.5\}$	3.36		4.58
24	$\{0.5, 1, 0.5\},$ $\{0, 0.5, 0\}$	0.2		6.34
25	$\{0.5, 1, 0.5\},$ $\{0.5, 0, 0\}$	0.29		6.56
	-1 Mg (vac.):			
26	$\{0.5, 1.5, 0.5\}$	12.98		5.36
27	$\{0, 1, 1\}$	14.36		4.71
28	$\{0.5, 1.5, 0.5\}$	14.69		4.73
29	no doping	8.2		7.62

Table 3.7: This table compares various different types of charge compensations, their ground state energy and band gap Δ . In the first column, the number serves as an identifier, since the respective calculation including the final position of the atoms as well as the density of states can be found in [Appendix C](#). The second column shows the initial position of the charge compensation before the relaxation. The values in the curly brackets indicate the x , y and z position in fractional coordinates in the $1 \times 1 \times 1$ unit cell, where the thorium atom lies in its center. For a visual depiction of the charge compensation in combination with the notation, please see the Figures in [section C.2](#). The third column is concerned with the energy of the ground state and therefore related via Boltzmann factors to the probability for the charge compensation to occur in the respective configuration. The value 0 was chosen to be the energetically most favorable configuration. As a consequence, configurations with higher values, i.e. longer bars are more unlikely to occur. The energetically most favorable type is the interstitial doping of $+2F$. Its configuration will subsequently be highlighted with a green color. In the final column is the value for the gap Δ . It is required for the gap to be larger than the isomer energy, such that the crystal stays transparent for the core transition energy. Note that all the calculations were done using SCAN. It is important to mention that, as we have discussed in [Figure 3.4](#), SCAN underestimates the band gap. When compared to a bulk calculation of MgF_2 , thorium doping with charge compensation has a lower energy, as can be seen in the last row. This means that the crystal will accept thorium as a dopant.

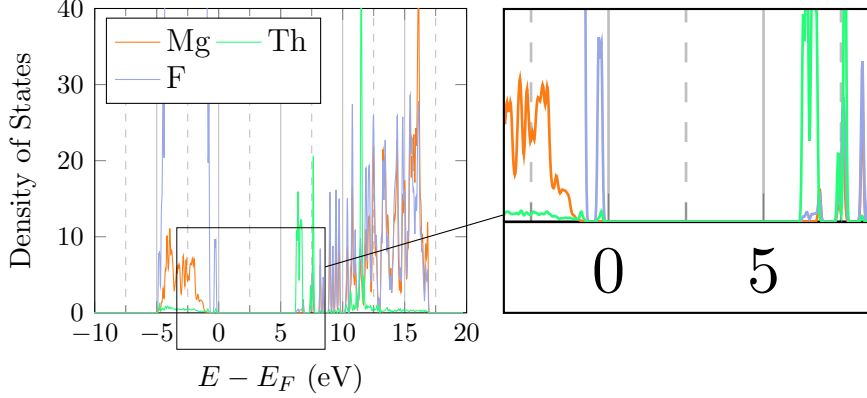


Figure 3.12: The density of states for the most probable configuration 19 of +2F interstitial is shown. The resulting band gap is estimated by the SCAN functional to be 6.51 eV. Notice, that the first excited states originate almost solely from the thorium atom.

A complete collection of all calculations with charge compensation, including a depiction of the final ionic positions, a plot for the density of states and tables for the total energies are shown in [Appendix C](#).

3.8 Electric Field Gradient

The quadrupole interaction of a nucleus with an external electric field is described by the quadrupole tensor and the electric field gradient [[AAB⁺90](#)]. The latter is a second rank tensor given by the partial spatial derivatives of the electrostatic potential V that is external to the nucleus, evaluated at the nucleus

$$V_{ij} = \left. \frac{\partial^2 V}{\partial x_i \partial x_j} \right|_{\text{nucleus}}. \quad (3.4)$$

Evidently, this tensor is symmetric and can therefore be diagonalized to have the diagonal values V_{xx} , V_{yy} and V_{zz} , which are conventionally ordered such that $|V_{zz}| \geq |V_{yy}| \geq |V_{xx}|$. Furthermore, it is traceless and thus only two parameters are independent. Usually these are given by V_{zz} and the asymmetry parameter

$$\eta = \frac{V_{xx} - V_{yy}}{V_{zz}}. \quad (3.5)$$

For a more detailed discussion and notably for the case that the electron wave function has an overlap with the nucleus, see reference [KV79]. The electric field gradient can be calculated numerically [PBBS98] and the result is shown in Table 3.8.

#	η				V_{zz} (V/Å ²)					
	0	0.5	1	1.5	-4,000	-2,000	0	2,000	4,000	6,000
1	9.6 · 10 ⁻²				4,148					
2	0.73				231					
3	0.64				493					
4	1.5 · 10 ⁻²				1,970					
5	0.59				-952					
6	0.55				446					
7	4.7 · 10 ⁻²				501					
8	0.23				-2,138					
9	0.1				-539					
10	0.77				-526					
11	0.19				-609					
12	0.54				-1,045					
13	0.12				-1,110					
14	0.49				780					
15	0.87				-544					
16	0.38				899					
17	0.31				423					
18	2.3 · 10 ⁻²				477					
19	0.92				439					
20	0.54				-400					
21	0.83				-394					
22	0.87				-525					













23	 0.63	-343 
24	 $7.4 \cdot 10^{-2}$	 405
25	 0.41	-420 
26	 0.24	-268 
27	 0.51	-590 
28	 0.54	-187 

Table 3.8: In this table, the electric field gradient at the thorium atom is shown for different charge compensations. For an explanation of the charge compensation in each row, please see [Table 3.7](#) or [section C.2](#). The energetically favored type of compensation is shown with a green identifier number.

Chapter 4

Discussion

In this work, we have demonstrated a basic approach to ab-initio simulations of materials. The lattice parameters of MgF_2 are in good agreement with the experiment. A comparison of various energy functionals reveals that only computationally demanding approaches such as the G_0W_0 -scheme or a HSE calculation with appropriate mixing, lead to values similar to the experimental value of the gap. The optical studies not only confirm the transparency of the crystal for the investigated energy range, but also display that the PBE functional leads to remarkably similar results in comparison with GW . The enthalpy of formation was also in accordance with the experiment, while the SCAN functional yields almost the same energy as the HSE functional. We have shown that upon introducing thorium as a dopant, it will substitute a magnesium atom. We have demonstrated that the use of a $4 \times 4 \times 4$ super cell with a Γ -only calculation is a very reasonable trade-off between computing speed and accuracy.

As the simulated data reveal MgF_2 will accept thorium as a dopant and the most probable configuration for charge compensation is the interstitial placement of $+2\text{F}$. Fortunately, the size of the gap is also preserved. Therefore, the direct excitation of the thorium nucleus could be possible according to our calculations. For the experimental realization it is important to mention that the charge compensation of oxygen reduces the gap and therefore, the impurity might lessen the crystals transparency. A magnesium vacancy is very unlikely to occur. It is energetically favorable if the charge compensation stays in the vicinity, but not too close to the thorium atom. Interestingly, the interstitial final position of the oxygen or fluorine atoms often converges in a position that breaks the symmetry of the lattice.

We have calculated that there is a large energy difference between the undoped MgF_2 and some type of doping. We note, that this does not necessarily mean that the crystal easily accepts thorium and the charge compensation with a great release of energy because usually, there is an energy barrier for the atoms to overcome when entering the crystal.

The most important unknown variable is the energy of the isomer state of $^{229\text{m}}\text{Th}$. As we can see in the density of states, the energies just above the gap are almost exclusively occupied by thorium states for all types of charge compensations. It might be possible, that the nucleus cannot be excited directly because the electrons will absorb the photons instead.

However, there is a possibility that the core will be indirectly excited by an excited electron if only the overlap between the nucleus and the electron wavefunction is large enough [HSNOP13, PFPT10, BKM+17]. This process is called electron-bridge. The huge advantage is, that the electron orbitals are much greater in size than the nucleus and therefore the absorption of a photon is more likely, due to its larger cross section. Additionally, if the energy of $^{229\text{m}}\text{Th}$ is below the gap, one could in principle place oxygen into MgF_2 deliberately to tailor the gap to a specific value.

The experiment is thus far concerned with the CaF_2 crystal, which shows a similar behavior as MgF_2 [Des16]. The current data show a high amount of luminescence in the core transition range, which might result from the excitation of thorium electrons above the gap [SSS15]. Further studies should calculate the overlap of these electrons with the nucleus. The choice of the host system could therefore not only be dependent on the gap, but also on the overlap of the electron wave function with the thorium nucleus if the electron-bridge mechanism can be realized.

Appendices

Appendix A

Theory

A.1 Isomer states

This section aims to give a qualitative discussion about metastable nuclear states, called isomer states.

When a nucleus is excited, it means that one or more of its protons or neutrons reach states with higher energy levels. Usually these are states with far higher energy than electronic excitations. There are several ways how the state decays into the ground state, most prominently by the emission of a photon. For these types of decay it is important to note that the angular momentum has to be conserved. In almost all cases it can be assumed, that the photon can carry away one unit of angular momentum, since it is a boson and thus the nuclear spin cannot change by more than one unit in the decay. These processes of so-called electric dipole transitions are defined by the term *allowed* decays.

What happens if the excited nucleus has more than one unit of spin? These processes are magnetic transitions and can still take place but take much more time. It is estimated that each additional unit of angular momentum decreases the rate by about 5 orders of magnitude [vD11]. Thus, the nucleus shows a metastable excited state, denoted with an m next to its atomic mass number. Typically, they decay in the order of 10^{-9} s [MWJC07]. In particular, there are two interesting isomer states, namely ^{180m}Ta and ^{229m}Th .

The former one is a state that has nine units of spin. The decay is thus extremely unlikely to occur. While its ground state decays with β -decay with a half life time of about 8 hours, the metastable state is estimated

to have a half life time of more than 10^{15} years. No decay of ^{180m}Ah has ever been observed and it is the only excited nucleus state, that is in fact stable.

The latter one, ^{229m}Th , is the main topic of this work. It is extraordinary due to its extremely small excitation energy that lies several orders of magnitude below what isomers usually have, as depicted in Figure A.1. In addition, due to its predicted long half life time, it would result in an immensely small natural linewidth of $\Delta E/E \approx 10^{-20}$ eV [vdWSLT17].

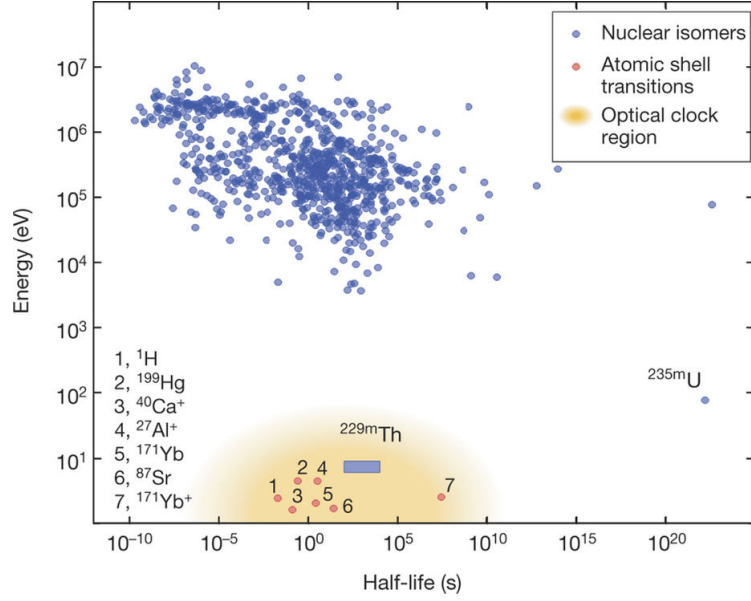


Figure A.1: This plot depicts the energy of isomer states on a logarithmic y-axis. ^{229m}Th shows by far the lowest energy difference to its ground state and makes it perfect to study in terms of a potential atomic clock. The figure was taken from [vdWSL+16].

Because the energy is in the range of optical lasers, the excitation could potentially lead to many interesting applications, for example testing the stability of fundamental constants [vdWSL+16, Fla06, RDG+10, LFDF09], studies of material properties and it may be used for building a laser [BKM+17, Tka11].

A.2 Ritz Method

The Ritz method states that the lowest energy eigenvalue, i.e. the ground state, satisfies the following relation

$$E_0 \leq \frac{\langle \Psi | H | \Psi \rangle}{\langle \Psi | \Psi \rangle}. \quad (\text{A.1})$$

The equality is only satisfied in the case of $|\Psi\rangle = |\Psi_0\rangle$, where $|\Psi_0\rangle$ is the ground state wave function.

Proof.

$$\begin{aligned} \langle \Psi | H | \Psi \rangle &= \sum_n \langle \Psi | H | \Psi_n \rangle \langle \Psi_n | \Psi \rangle \\ &= \sum_n E_n \langle \Psi | \Psi_n \rangle \langle \Psi_n | \Psi \rangle \\ &\geq E_0 \sum_n \langle \Psi | \Psi_n \rangle \langle \Psi_n | \Psi \rangle \\ &= E_0 \langle \Psi | \Psi \rangle \end{aligned} \quad (\text{A.2})$$

□

A.3 Functionals

Functionals are a widely applied mathematical concept in physics. Informally speaking, a functional takes a function as an input and produces a scalar value as the output. Let V be a vector space of $K \in \{\mathbb{R}, \mathbb{C}\}$. Then F is a functional if [BFK⁺15]

$$F : V \rightarrow K \quad (\text{A.3})$$

As an example [Cap02], consider the particle number, which is also discussed in this work

$$N = \int n(\mathbf{r}) \, d^3r = N[n]. \quad (\text{A.4})$$

The square brackets denote, that the variable n is in fact a function $n(\mathbf{r})$. The integral operation reduces the particle density n to the scalar value of the total particle number N .

Functional variation

Consider a functional in one variable $y = f(x)$ [Cap02]. To construct a meaningful formula for the variation, there are two types of variations to consider. When the functional dependence $f(x)$ is fixed, the usual approach is the differential dy , which is a quantity that measures how y changes as a result of a variation $x \rightarrow x + dx$ of the variable x . On the other hand, if the value x is fixed, we can study how the value y changes at this point by a variation of $f(x)$, which is expressed by the functional variation δf

$$\tilde{f}(x) = f(x) + \delta f(x). \quad (\text{A.5})$$

$\tilde{f}(x)$ is different only for an infinitesimal perturbation $\delta y(x)$ from $y(x)$ for all $x \in [x_0, x_1]$. An important condition is that the values on the borders are held fixed $\delta f(x_0) = \delta f(x_1) = 0$.

Functional derivative

The differential of a functional is defined to be the part of the difference $F[f + \delta f] - F[f]$ that depends on δf linearly [PW94]. Because each $\delta f(x)$ may contribute to this difference we write for small δf

$$\delta F = \int \frac{\delta F}{\delta f(x)} \delta f(x) dx. \quad (\text{A.6})$$

Notice the similarities to the total differential of a function $G(x_1, x_2, \dots)$: $dG = \sum_i \partial G / \partial x_i dx_i$. In fact, equation (A.6) can be seen as an extension to the total differential.

The quantity $\delta F / \delta f(x)$ is the *functional derivative of F with respect to f at the point x* . It is possible to determine a functional derivative by expanding $F[f + \delta f] - F[f]$ in terms of δf and keeping only the first order term. Thus a functional $F[f]$ is differentiable if $\delta F / \delta f(x)$ exists in the sense of

$$\lim_{\varepsilon \rightarrow 0} \frac{F[f + \varepsilon \phi] - F[f]}{\varepsilon} = \left\{ \frac{d}{d\varepsilon} F[f + \varepsilon \phi] \right\}_{\varepsilon=0} = \int \frac{\delta F}{\delta f(x)} \phi(x) dx. \quad (\text{A.7})$$

A practical formula can be found that is applicable for most cases of interest. For a functional $F[n] = \int f(n, n', n'', \dots; x) dx$ the derivative can be found to be [GFS00]

$$\frac{\delta F[n]}{\delta n(x)} = \frac{\partial f}{\partial n} - \frac{d}{dx} \frac{\partial f}{\partial n'} + \frac{d^2}{dx^2} \frac{\partial f}{\partial n''} - \frac{d^3}{dx^3} \frac{\partial f}{\partial n'''} + \dots \quad (\text{A.8})$$

A.4 PBE Functional

The PBE functional can be written as [XI04]

$$E_{xc}^{PBE} = \int d^3r n(\mathbf{r}) \varepsilon_x^0(n) F_{xc}(r_s, \zeta, s), \quad (\text{A.9})$$

where r_s is the local Wigner-Seitz radius defined as $r_s = [(4\pi/3)n(\mathbf{r})]^{1/3}$, the local spin polarization $\zeta = (n_\uparrow - n_\downarrow)/n$ and s is a dimensionless density gradient, defined as $s = |\nabla n|/(2k_F n)$, where k_F is the Fermi wave vector. The enhancement factor

$$F_{xc}(r_s, \zeta, s) \equiv F_x(s) + \frac{\varepsilon_c^0(r_s, \zeta)}{\varepsilon_x^0(n)} F_c(r_s, \zeta, t), \quad (\text{A.10})$$

where $t = |\nabla n|/(2gk_s n)$, with $g = [(1 + \zeta)^{2/3} + (1 - \zeta)^{2/3}]/2$ and $k_s = (4k_F/\pi)^{1/2}$ is the Thomas-Fermi screening wave vector.

$$F_x^{\text{PBE}}(s) = 1 + \kappa - \frac{\kappa}{1 + \frac{\mu}{\kappa} s^2}, \quad (\text{A.11})$$

where $\kappa = 0.804$ and $\mu = 0.21951$.

$$F_c(r_s, \zeta, t) \equiv 1 + \frac{H(r_s, \zeta, t)}{\varepsilon_c^0(r_s, \zeta)} \quad (\text{A.12})$$

and

$$H^{\text{PBE}} = g^3 \frac{\beta^2}{2\alpha} \ln \left[1 + \frac{2\alpha}{\beta} \frac{t^2 + At^4}{1 + At^2 + A^2 t^4} \right], \quad (\text{A.13})$$

where $\alpha = 0.0716$, $\beta = 0.066725$, $A = 2\alpha/(\beta \exp[-2\alpha\varepsilon_c^0(r_s, \zeta)/(g^3\beta^2)])$.

A.5 Optics

When an electric field \mathbf{E} enters a medium, the atoms and molecules will be polarized and thus create a field \mathbf{D} , that weakens the original field \mathbf{E} . The strength of this weakening is described by the relative permittivity $\varepsilon(\omega)$

$$\mathbf{D} = \varepsilon(\omega)\mathbf{E}. \quad (\text{A.14})$$

In SI-Units the vacuum formally has a permittivity, denoted by ε_0 . In a material, the relative permittivity $\varepsilon_r(\omega)$ is a dimensionless number, with the relationship

$$\varepsilon_r = \frac{\varepsilon(\omega)}{\varepsilon_0}. \quad (\text{A.15})$$

In anisotropic media, the relative permittivity is a second rank tensor, but for simplicity we assume a scalar value for ε_r . Generally speaking, the relative permittivity is a complex number, with $\varepsilon_r(\omega) = \varepsilon_r^{\text{Re}}(\omega) - i\varepsilon_r^{\text{Im}}(\omega)$. In the following, we will see that the imaginary part describes the absorption of an electromagnetic wave. To improve readability, we will drop the obvious dependencies of functions.

Solving Maxwell's inhomogeneous equations in the case of zero charge and current, we end up with the wave equation for \mathbf{E} and \mathbf{B} respectively

$$\nabla^2\mathbf{E} - \varepsilon\mu\frac{\partial^2\mathbf{E}}{\partial t^2} = 0 \quad (\text{A.16})$$

$$\nabla^2\mathbf{B} - \varepsilon\mu\frac{\partial^2\mathbf{B}}{\partial t^2} = 0 \quad (\text{A.17})$$

We know, that the solution of wave equations propagate with a speed given by the factor in front of the derivative. In vacuum this would lead to $1/c^2 = \varepsilon\mu$. In this case, we use equation (A.15) and get

$$v = \frac{1}{\sqrt{\varepsilon\mu}} = \frac{1}{\sqrt{\varepsilon_r\mu_r}} c = \frac{c}{n}, \quad (\text{A.18})$$

with the index of refraction being

$$n = \sqrt{\varepsilon_r\mu_r}. \quad (\text{A.19})$$

Considering an electromagnetic plane wave

$$\mathbf{E} = \text{Re}\{\mathbf{E}_0 e^{i(\mathbf{k}\cdot\mathbf{x}-\omega t)}\} \quad (\text{A.20})$$

and plugging it into the wave equation (A.17), we get a dispersion relation

$$\omega^2 = \frac{\varepsilon\mu}{k^2}, \quad (\text{A.21})$$

and since $\omega = 2\pi\nu = \frac{2\pi c}{\lambda}$ it follows that

$$k = \frac{2\pi}{\lambda} n. \quad (\text{A.22})$$

Now, if we plug in \mathbf{k} into the plane wave (A.20), we see that the imaginary part of n results in a damping of the wave

$$\mathbf{E} = \text{Re}\left\{\mathbf{E}_0 e^{i\left(\frac{2\pi}{\lambda} n x - \omega t\right)}\right\} = e^{-\frac{2\pi}{\lambda} \text{Im}\{n\}x} \text{Re}\left\{\mathbf{E}_0 e^{i\left(\frac{2\pi}{\lambda} \text{Re}\{n\}x - \omega t\right)}\right\}. \quad (\text{A.23})$$

Appendix B

Optimization

B.1 Compilation

For this thesis the compilation of VASP from the source code was needed. During the compilation, the Intel compiler offers an optimization flag `-O`, where the subsequent number increases the speed of computation. It was determined, whether this flag produced significant improvements and whether it will be more prone to errors (see [Table B.1](#)). After the analysis, it was determined that the `-O1` flag was practically as efficient as `-O2` while execution errors can be more easily avoided.

	Time (s)		Page Faults	
	CPU	Total	Minor	Major
<code>-O1</code>	13.2	14.8	24941	28
<code>-O2</code>	13.1	14.0	25454	46

[Table B.1](#): For a test calculation, the two optimization flags are compared. While the total elapsed time decreased by about 5 %, the major page faults increased by 64 %.

B.2 Ionic Relaxation Parameters

Because the minimization procedure is done iteratively, a proper setting for the minimization scheme (time steps and algorithms) is important for convergence. A study thereof is shown in [Table B.2](#). In conclusion, the CG-method outperforms the DIIS scheme by far and was thus used for

most of the calculations.

POTIM (fs)	IBRION=1		IBRION=2	
	Time (min)	# steps	Time (min)	# steps
0.1	418	400	145	99
0.2	419	400	140	95
0.3	379	400	153	104
0.4	384	400	187	141
0.5	280	284	144	99

Table B.2: In this table the parameter POTIM was varied for different IBRIONs. The case IBRION=1 corresponds to the DIIS scheme, while IBRION=2 uses the CG method, as mentioned in [subsection 2.4.5](#). The system used for the computation was a 2F interstitial $2 \times 2 \times 2$ super cell of MgF₂ with Th doping and a $3 \times 3 \times 3$ Monkhorst-Pack mesh in **k**-space. The maximum number of ionic steps is controlled by the NSW-tag and was set to NSW = 400. The functional behavior of POTIM remains unclear but it is obvious, that the CG method converges much faster and more reliable than DIIS for the case studied.

B.3 Paralellization

The calculations in DFT and beyond often need massively parallel machines to simulate systems with many atoms. There are a number of ways to increase computation speed with VASP with the architecture in mind. The flag NPAR controls how the calculation of the bands is distributed among the nodes. It was determined that the best optimization for the system is at NPAR = 4 (see [Figure B.1](#)).

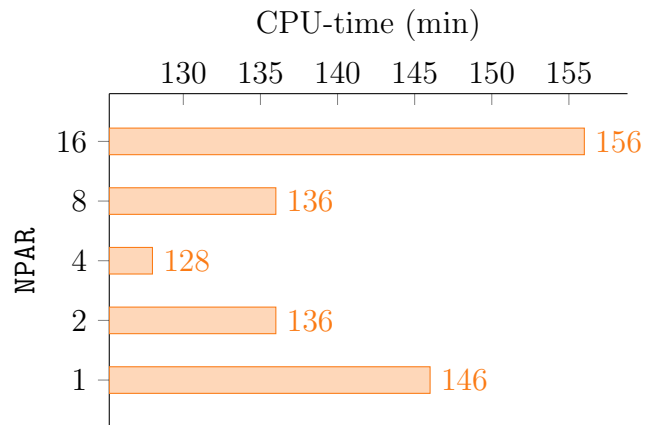


Figure B.1: The performance of a MgF_2 with Th doping was compared for different numbers of NPAR. The unit cell was $2 \times 2 \times 2$ in size and the \mathbf{k} -points grid was chosen to be a $3 \times 3 \times 3$ Monkhorst-Pack mesh. It can be seen, that $\text{NPAR} = 4$, lies at a clear minimum.

Appendix C

List of Calculations

This section includes a comprehensive list of the calculations made for the different charge compensations. The respective position of the charge position is given in fractional units of the $1 \times 1 \times 1$ unit cell with thorium at its center.

C.1 Total Energies

To compare different systems energetically, there must be the same number of particles in it. Covering all discussed cases, the total ensemble consists of:



C.1.1 +O (Interstitial)

Inside the crystal we have: $127 \text{ Mg} \quad 256 \text{ F} \quad 1 \text{ Th} \quad 1 \text{ O}$

To get the total energy one needs to calculate

$$E = \text{VASP} + \frac{1}{2} \text{ O}_2 + \text{F}_2 \quad (\text{C.1})$$

#	Position	Energy (eV)
1	{0.5, 1, 0.5}	-3115.0862
2	{0.85, 0.85, 0.5}	-3115.6279
3	{0.3, 0.7, 1}	-3114.6551
4	{1, 1.5, 0.5}	-3113.4985

Table C.1: Total energies for interstitial oxygen as charge compensation.

C.1.2 +2O (Substitutional)

Inside the crystal we have: 127 Mg 254 F 1 Th 2 O

To get the total energy one needs to calculate

$$E = \text{VASP} + 2 \text{F}_2 \quad (\text{C.2})$$

#	Position	Energy (eV)
5	{0.7, 0.7, 0} {0.7, 0.7, 1}	-3108.2650
6	{0.2, 0.8, 0.5} {0.7, 0.7, 1}	-3110.6901
7	{0.3, 0.3, 0} {0.7, 0.7, 1}	-3107.6791
8	{0.3, 0.3, 1} {0.7, 0.7, 1}	-3108.3002

Table C.2: Total energies for substitutional oxygen as charge compensation.

C.1.3 +2F (Interstitial)

Inside the crystal we have: 127 Mg 258 F 1 Th

To get the total energy one needs to calculate

$$E = \text{VASP} + \text{O}_2 \quad (\text{C.3})$$

#	Position		Energy (eV)
9	{0.5, 1, 0.5}	{0.5, 0, 0.5}	-3121.0604
10	{0.5, 1, 0.5}	{1, 0.5, 0.5}	-3120.8772
11	{0.15, 0.15, 0.5}	{0.85, 0.85, 0.5}	-3120.0877
12	{0.3, 0.7, 0}	{0.3, 0.7, 1}	-3119.5722
13	{0.7, 0.3, 1}	{0.3, 0.7, 1}	-3120.2324
14	{0.7, 0.3, 0}	{0.3, 0.7, 1}	-3120.4227
15	{0.15, 0.15, 0.5}	{0.5, 1, 0.5}	-3121.0771
16	{0.3, 0.7, 1}	{0.5, 1, 0.5}	-3121.1610
17	{0.15, 0.15, 0.5}	{0.3, 0.7, 1}	-3121.4223
18	{0.5, 1, 0}	{0.5, 1, 1}	-3121.3496
19	{0.5, 0, 0}	{0.5, 1, 1}	-3121.9421
20	{0.5, 1, 1}	{0.5, 0, 1}	-3121.9317
21	{0.5, 1, 1}	{1, 0.5, 1}	-3121.5454
22	{0.5, 1, 1}	{1, 0.5, 0}	-3121.8244
23	{0.5, 1, 1.5}	{0.5, 1.5, -0.5}	-3118.5821
24	{0.5, 1, 0.5}	{0, 0.5, 0}	-3121.7396
25	{0.5, 1, 0.5}	{0.5, 0, 0}	-3121.6544

Table C.3: Total energies for interstitial fluorine as charge compensation

C.1.4 $-Mg$ (Vacancy)

Inside the crystal we have: 126 Mg 256 F 1 Th

To get the total energy one needs to calculate

$$E = \text{VASP} + \text{Mg} + \text{O}_2 + \text{F}_2 \quad (\text{C.4})$$

#	Position	Energy (eV)
26	{0.5, 1.5, 0.5}	-3108.9670
27	{0, 1, 1}	-3107.5857
28	{0.5, 1.5, 0.5}	-3107.2527

Table C.4: Total energies for a magnesium vacancy as charge compensation.

C.1.5 No Doping

Inside the crystal we have:

128 Mg 256 F

To get the total energy one needs to calculate

$$E = \text{VASP} - 1\text{Mg} + 1\text{Th} + 1\text{F}_2 + 1\text{O}_2 \quad (\text{C.5})$$

#	Energy (eV)
29	-3113.7467

Table C.5: Total energy for a $4 \times 4 \times 4$ cell of MgF_2 without doping.

C.1.6 PBE

For the most probable configuration, a PBE calculation was also performed to validate the result.

#	Energy (eV)	$E_{\text{MgF}_2} - E$ (eV)	Δ (eV)	η	V_{zz} (V/Å ²)
19 (PBE)	-2032.4862	3.03	5.82	1.00	436
19 (SCAN)	-3121.9421	8.20	6.51	0.92	439

Table C.6: In this table, a comparison of the PBE and the SCAN functional is demonstrated. As expected, PBE underestimates the band gap Δ . The values for the electric field gradient are in good accordance with SCAN. However, we are surprised to find a large deviation in the energy difference of the undoped MgF_2 .

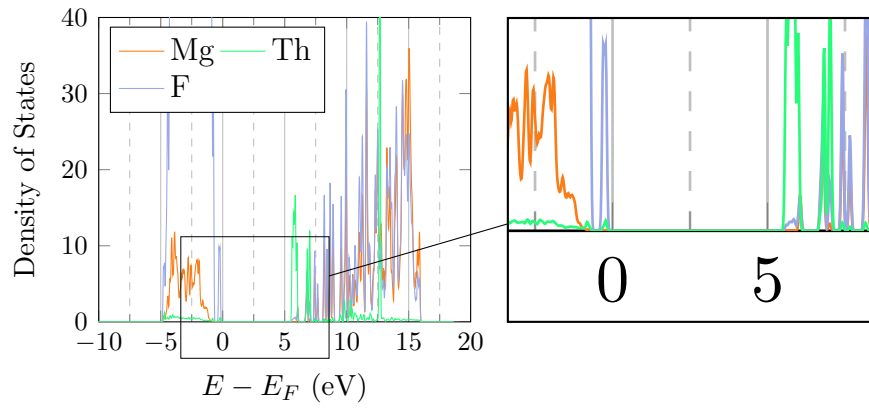


Figure C.1: The density of states for the most probable configuration calculated with PBE is shown. The band gap is $\Delta = 5.8464$ eV.

C.2 Plots

On the top of each page is a figure that shows the displacement of the atoms when the dopant and charge compensations are introduced. Note that the sizes of the atoms are not to scale. The charge compensations and the thorium atom are highlighted by making the sphere larger.

At the bottom of each page the DOS for each element is depicted separately and the region around the gap Δ is zoomed in. The number of samples for the whole DOS is controlled by the `NEDOS` flag in VASP. It was set to `NEDOS=3000` and therefore, a lot of spikes appear due to some isolated and relatively flat energy bands. The spikes are an artifact from calculation only the Γ -point.

C.2.1 O Interstitial

1

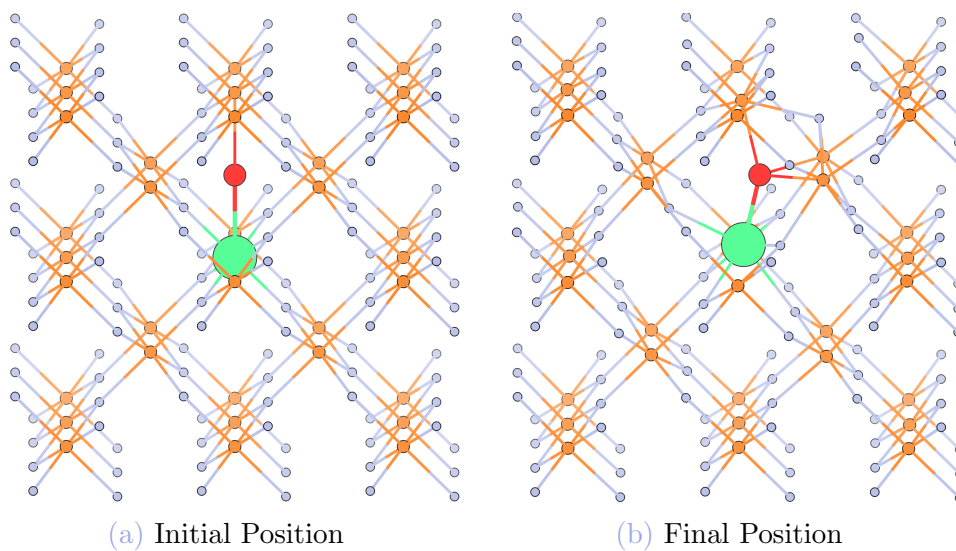


Figure C.2: Initial position of the interstitial oxygen: $\{0.5, 0.5, 1\}$.

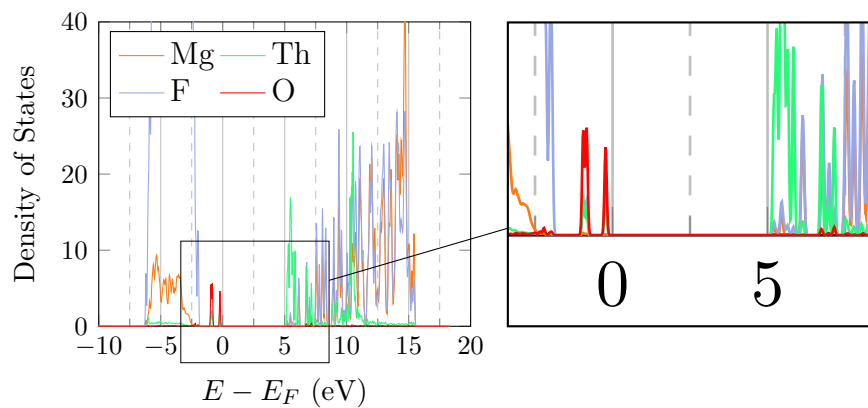


Figure C.3: $\Delta = 5.4285$ eV

2

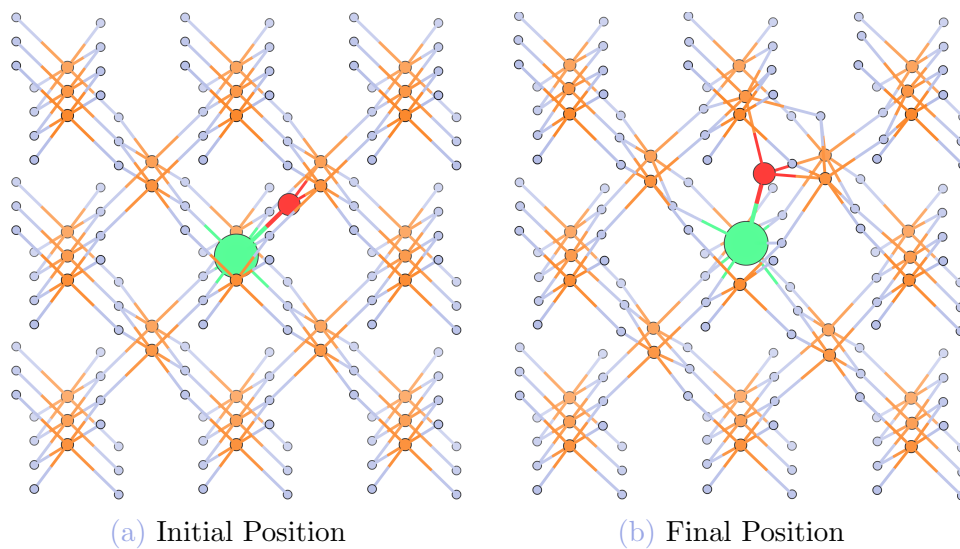


Figure C.4: Initial position of the interstitial oxygen: $\{0.85, 0.85, 0.5\}$.

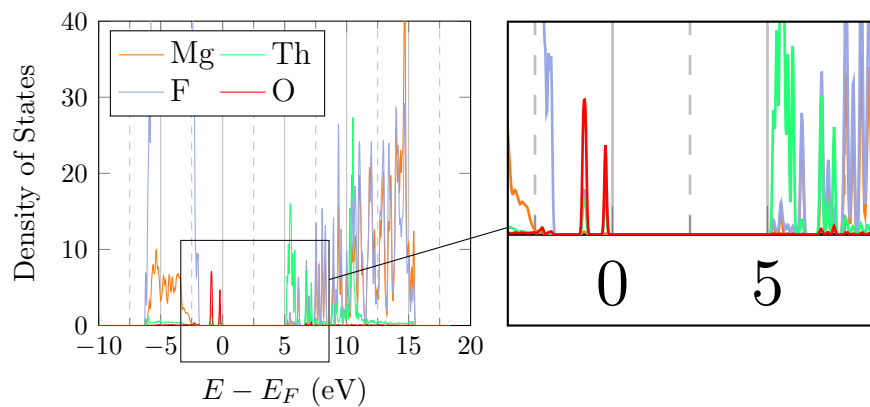


Figure C.5: $\Delta = 5.4221$ eV

3

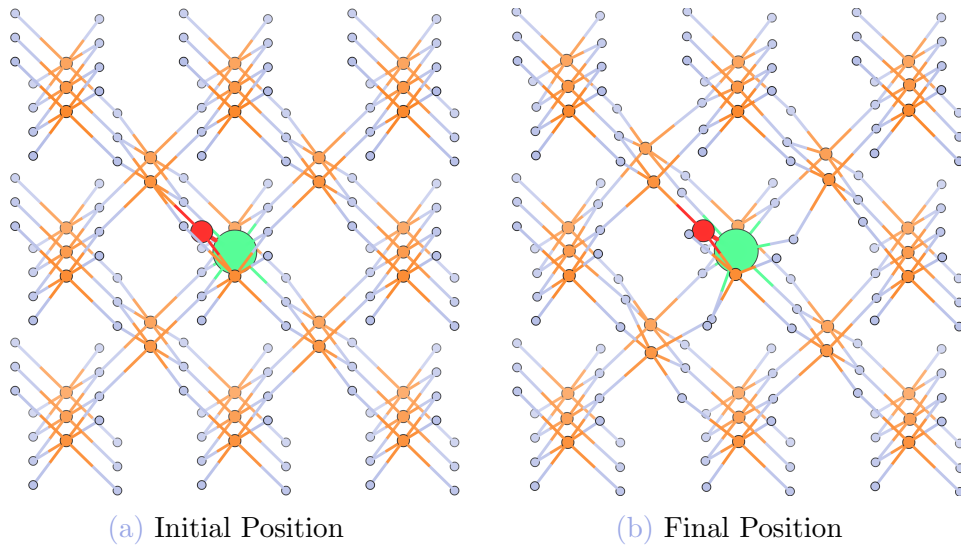


Figure C.6: Initial position of the interstitial oxygen: $\{0.3, 0.7, 1\}$.

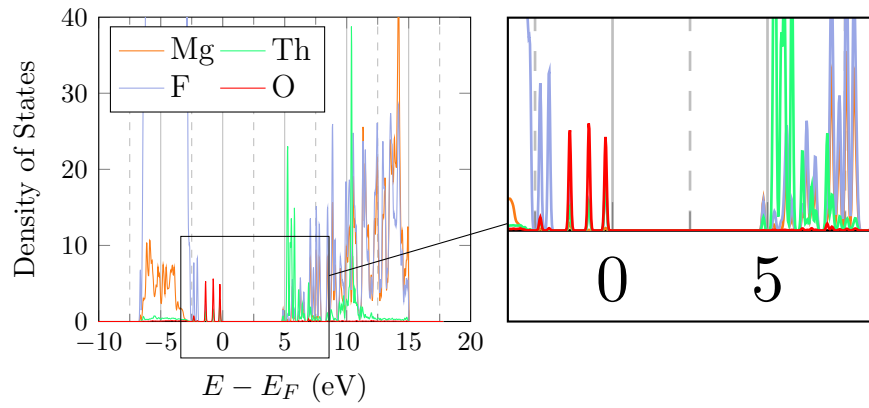


Figure C.7: $\Delta = 5.0928$ eV

4

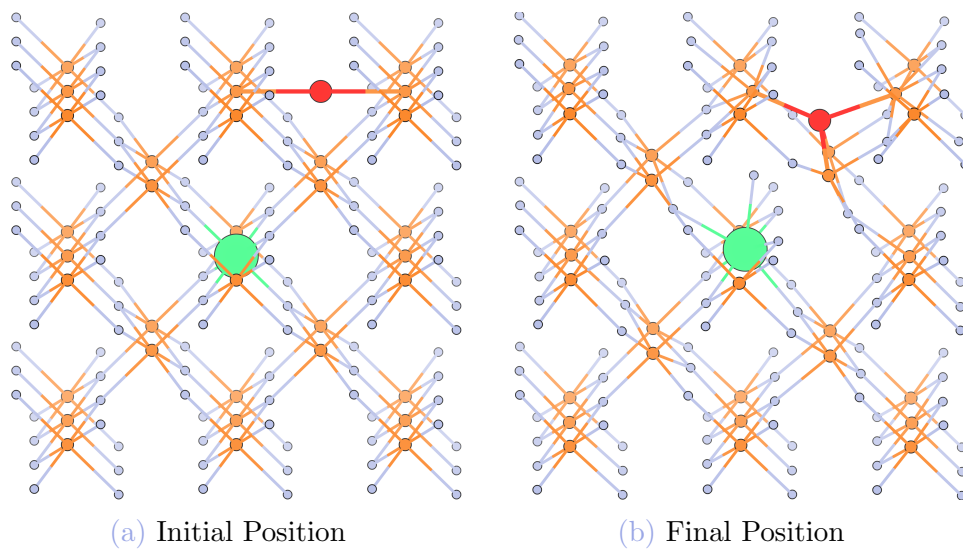


Figure C.8: Initial position of the interstitial oxygen: $\{1.5, 1.5, 0.5\}$.

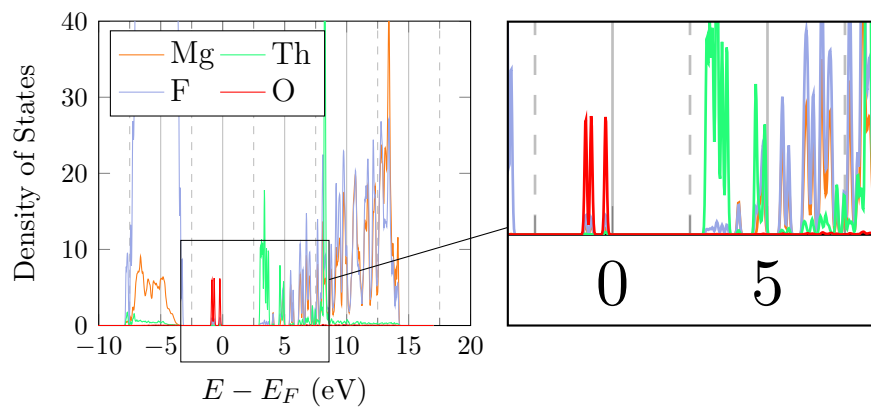


Figure C.9: $\Delta = 3.2613$ eV

C.2.2 O Substitutional

5

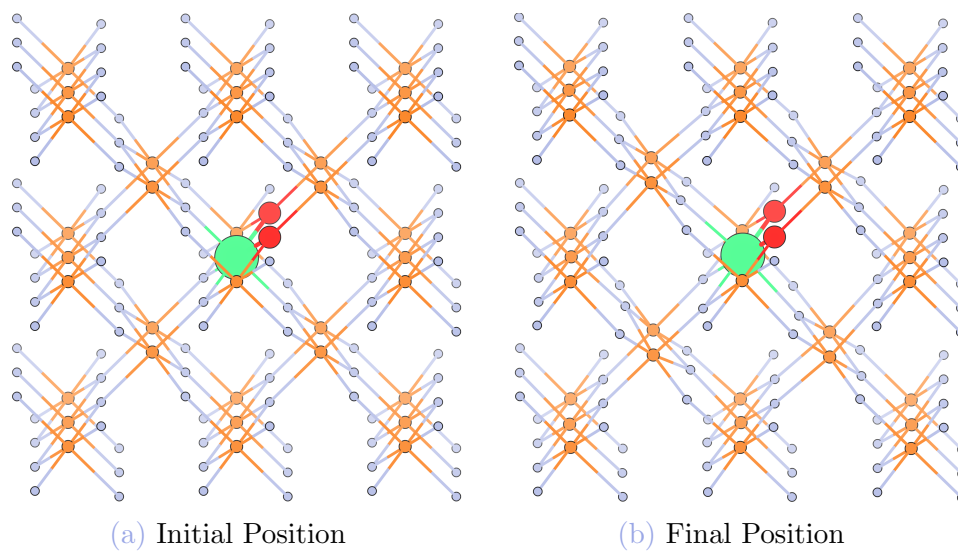


Figure C.10: Initial positions of the substitutional oxygens: $\{0.7, 0.7, 0\}$ and $\{0.7, 0.7, 1\}$.

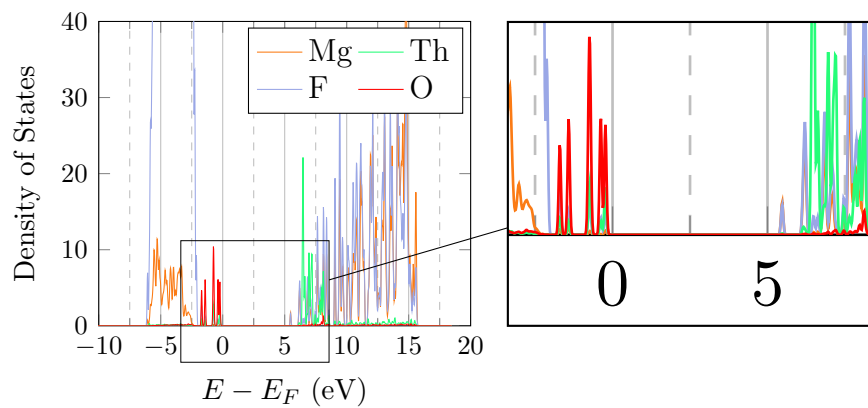


Figure C.11: $\Delta = 5.7029$ eV

6

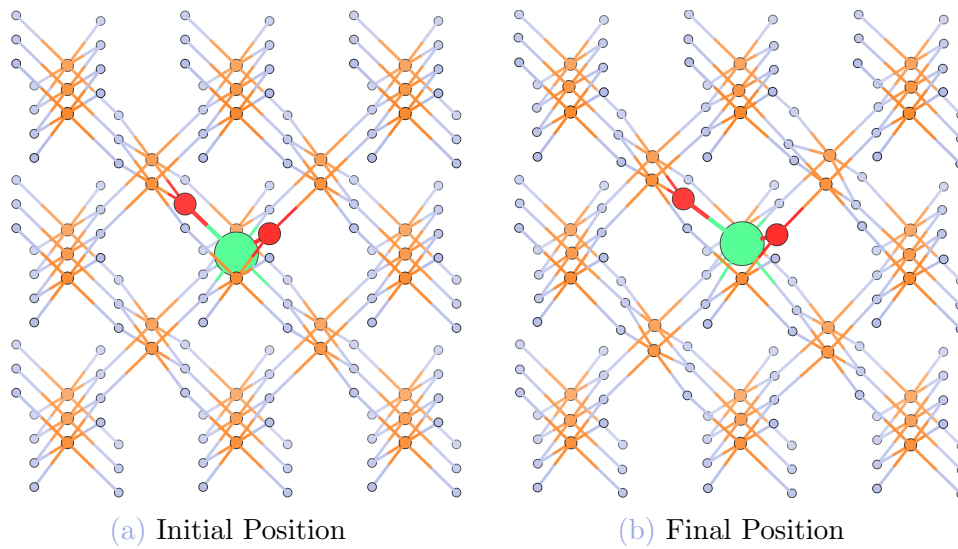


Figure C.12: Initial positions of the substitutional oxygens: $\{0.2, 0.8, 0.5\}$ and $\{0.7, 0.7, 1\}$.

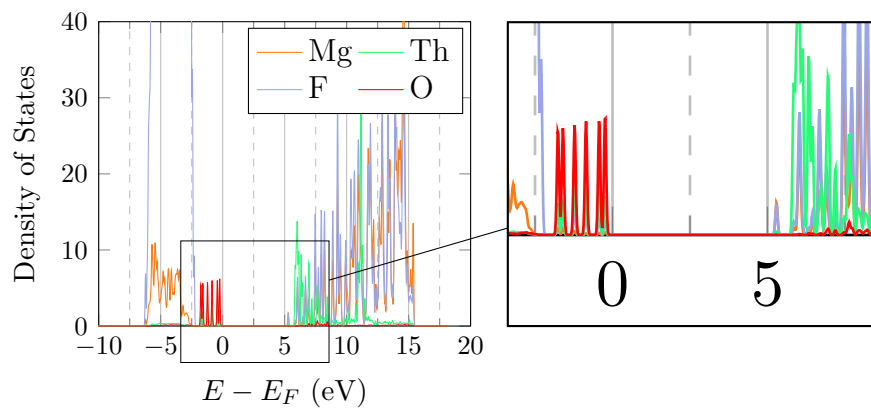


Figure C.13: $\Delta = 5.5298$ eV

7

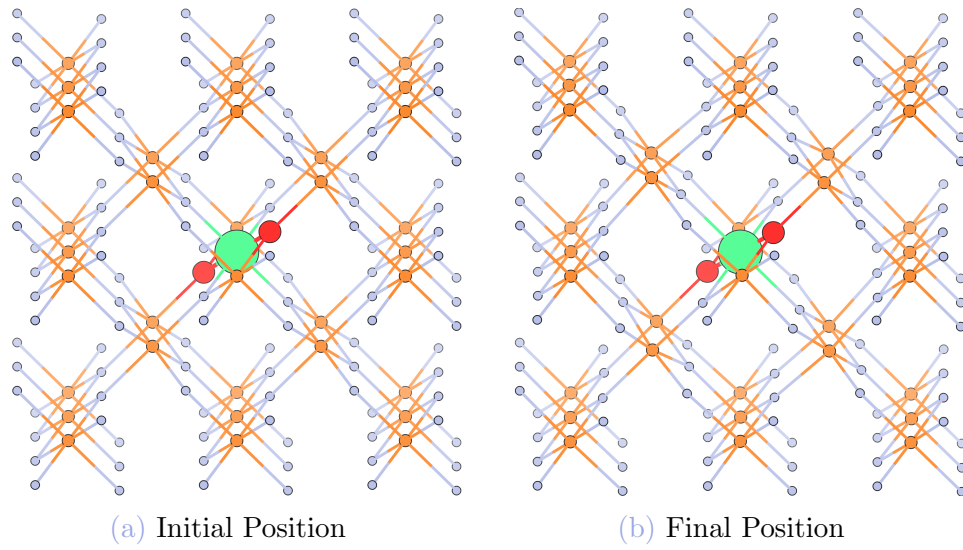


Figure C.14: Initial positions of the substitutional oxygens: $\{0.3, 0.3, 0\}$ and $\{0.7, 0.7, 1\}$.

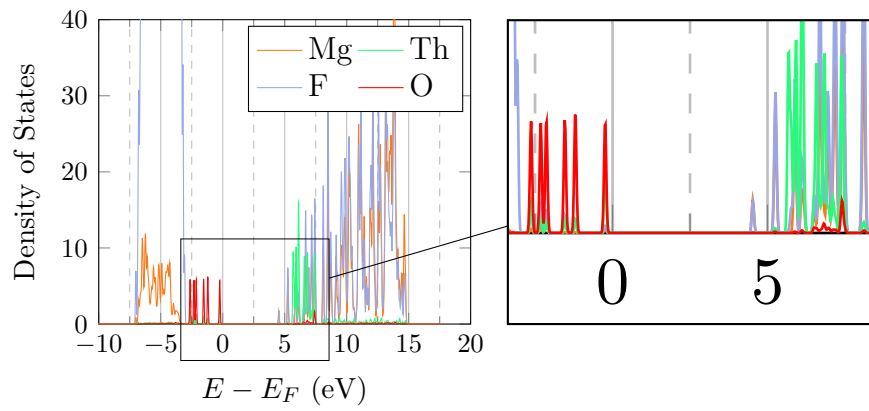


Figure C.15: $\Delta = 4.767$ eV

8

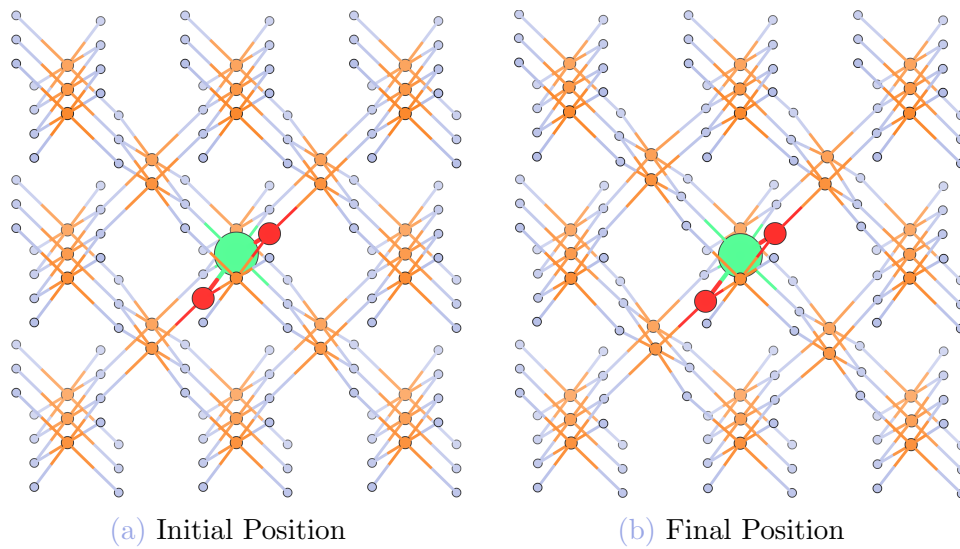


Figure C.16: Initial positions of the substitutional oxygens: $\{0.3, 0.3, 1\}$ and $\{0.7, 0.7, 1\}$.

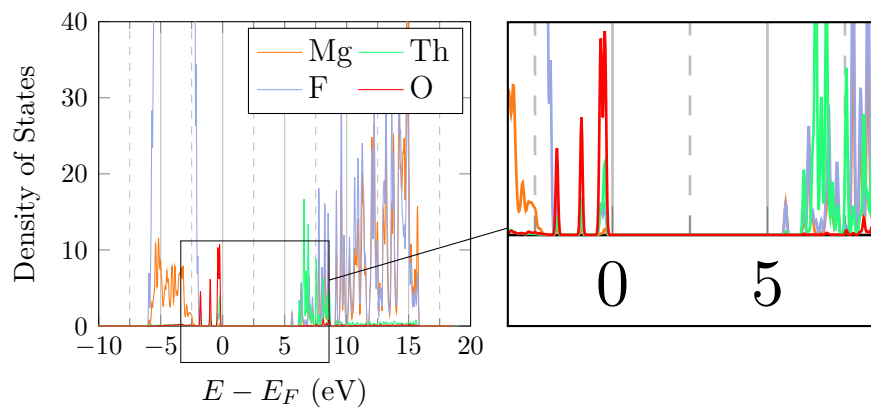


Figure C.17: $\Delta = 5.8164$ eV

C.2.3 F Interstitial

9

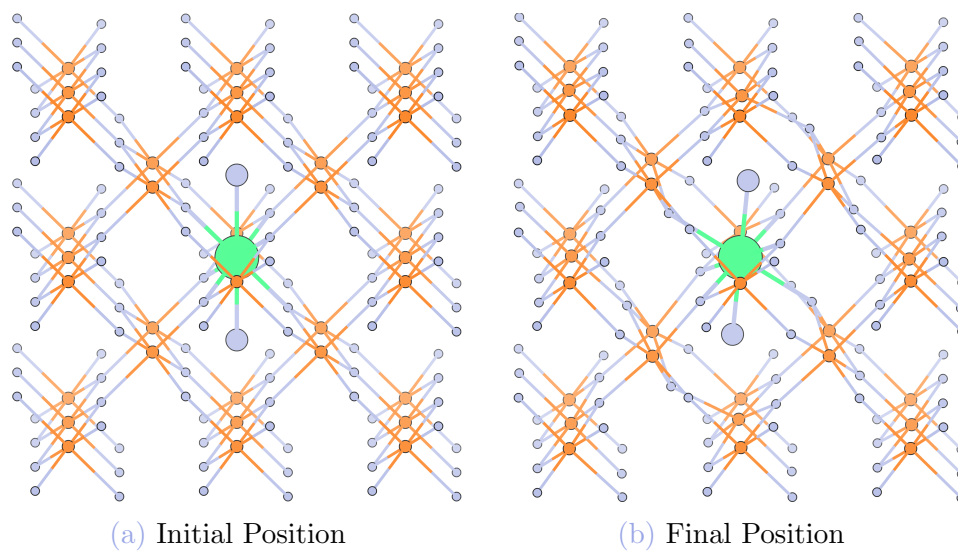


Figure C.18: Initial positions of the interstitial fluorine: $\{0.5, 1, 0.5\}$ and $\{0.5, 0, 0.5\}$.

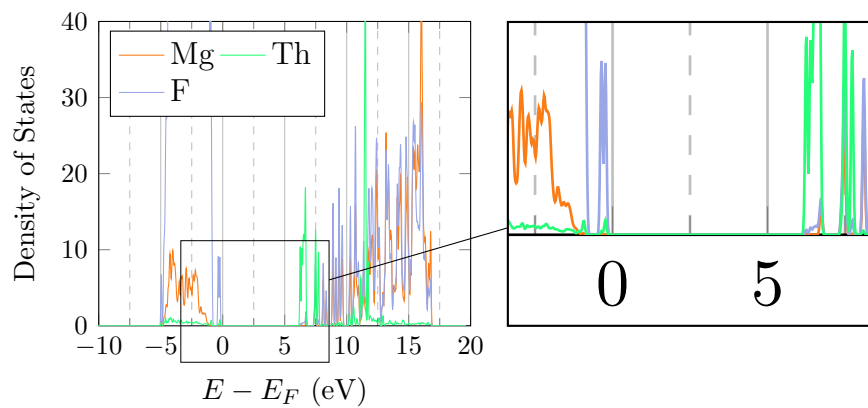


Figure C.19: $\Delta = 6.4807$ eV

10

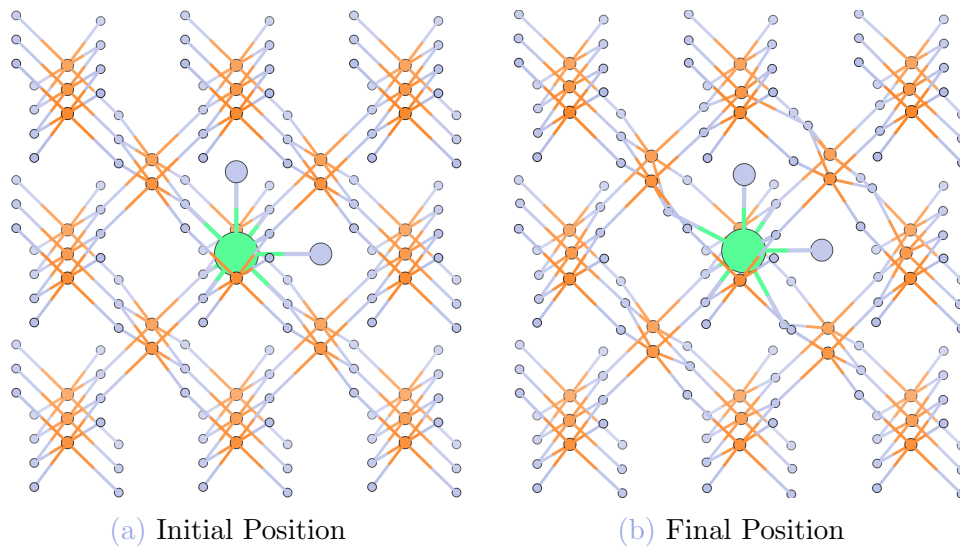


Figure C.20: Initial positions of the interstitial fluorine: $\{0.5, 1, 0.5\}$ and $\{1, 1, 0.5\}$.

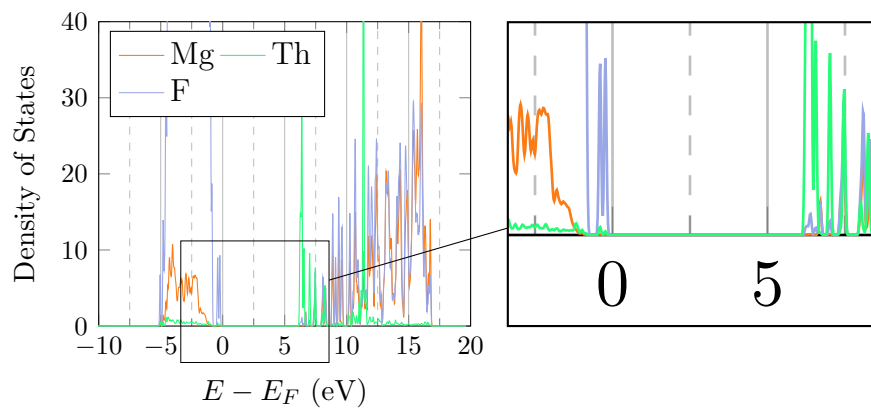


Figure C.21: $\Delta = 6.4631$ eV

11

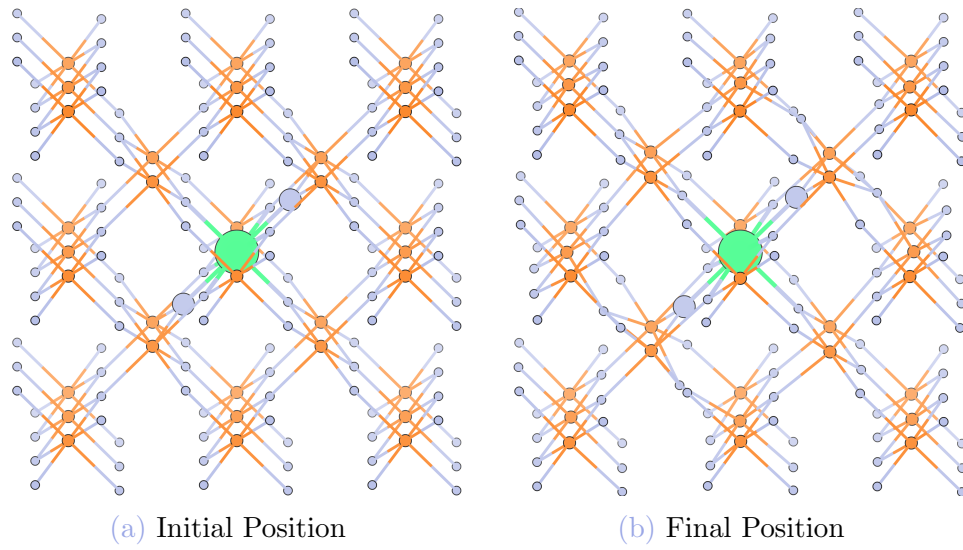


Figure C.22: Initial positions of the interstitial fluorine: $\{0.15, 0.15, 0.5\}$ and $\{0.85, 0.85, 0.5\}$.

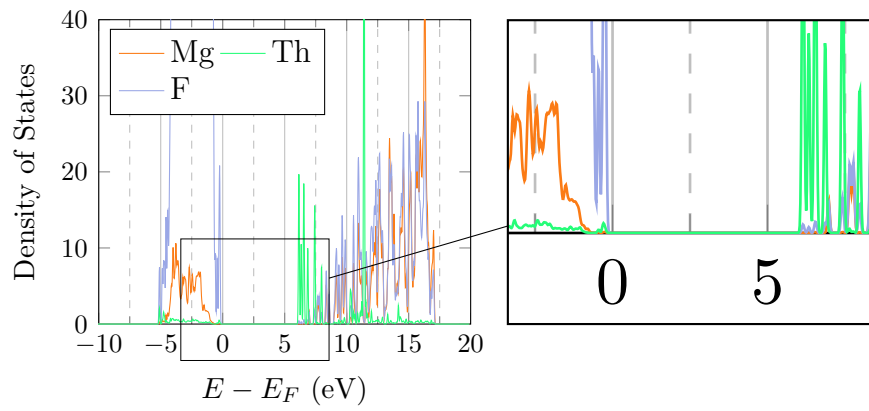


Figure C.23: $\Delta = 6.3693$ eV

12

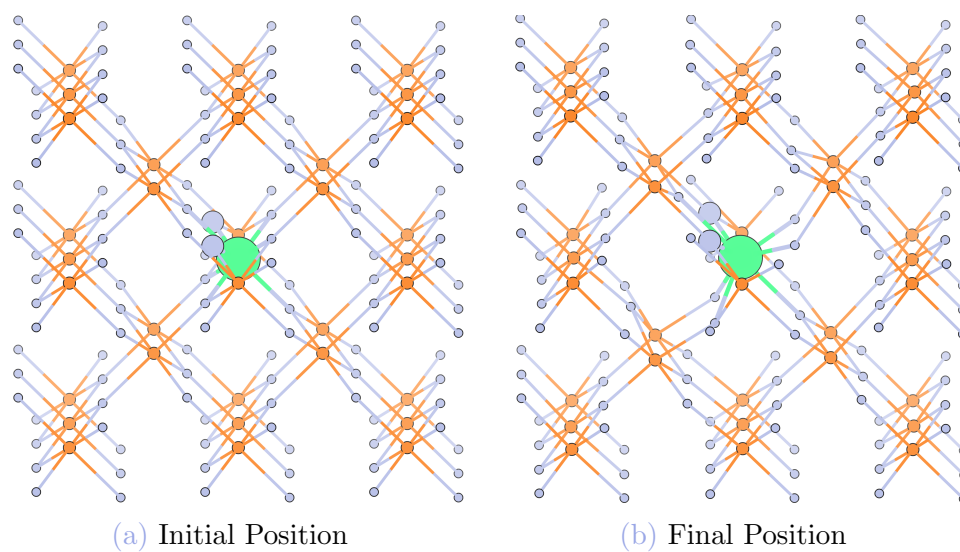


Figure C.24: Initial positions of the interstitial fluorine: $\{0.3, 0.7, 0\}$ and $\{0.3, 0.7, 1\}$.

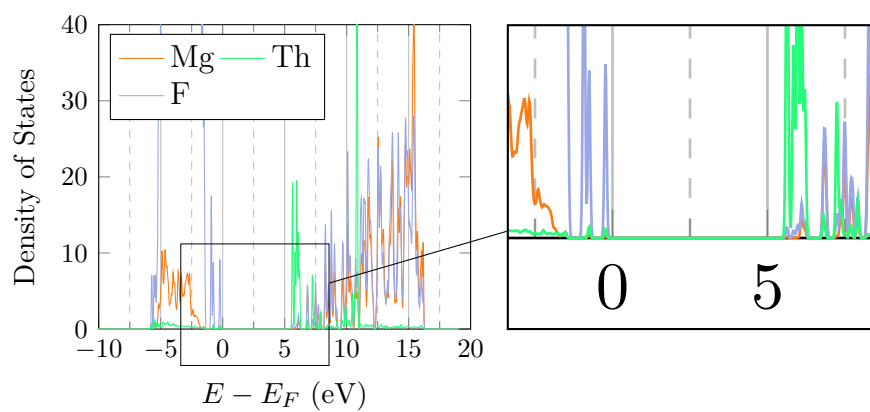


Figure C.25: $\Delta = 5.8464$ eV

13

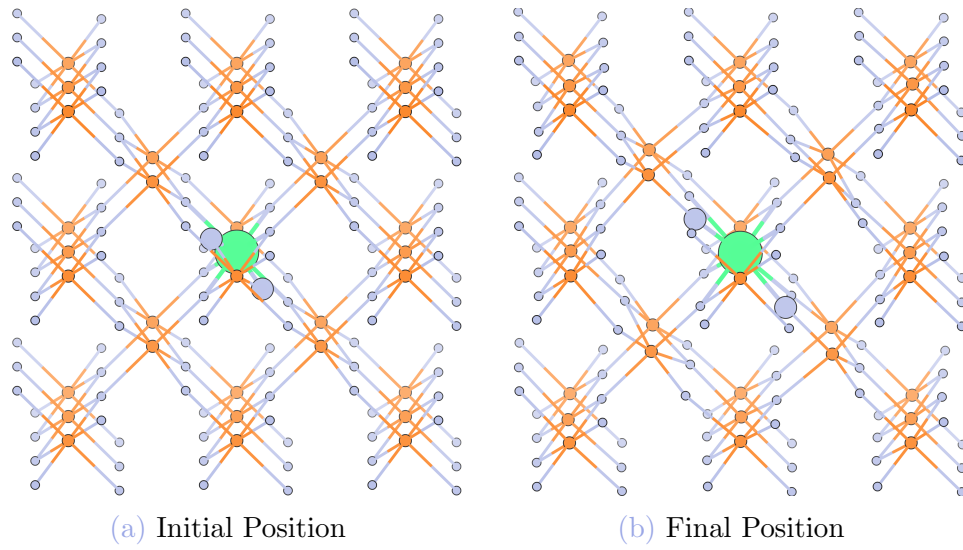


Figure C.26: Initial positions of the interstitial fluorine: $\{0.7, 0.3, 1\}$ and $\{0.3, 0.7, 1\}$.

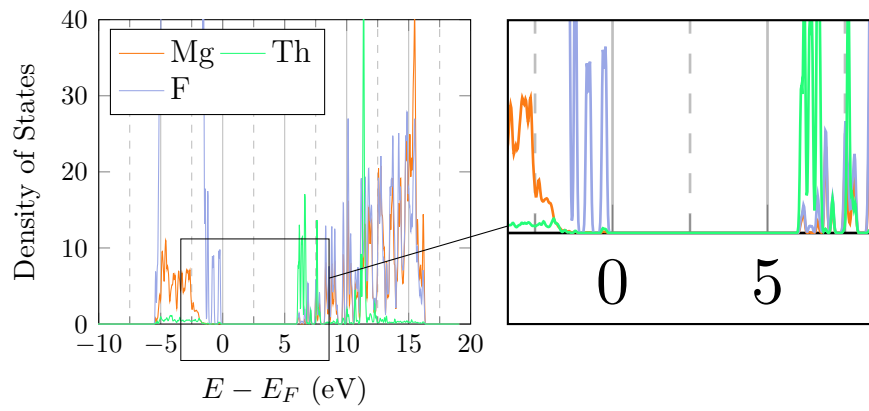


Figure C.27: $\Delta = 6.3056$ eV

14

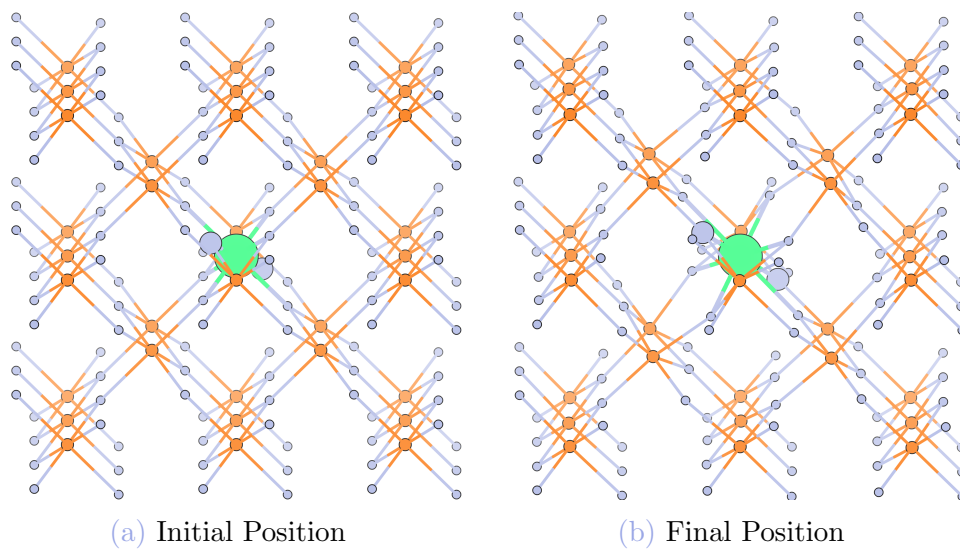


Figure C.28: Initial positions of the interstitial fluorine: $\{0.7, 0.3, 0\}$ and $\{0.3, 0.7, 1\}$.

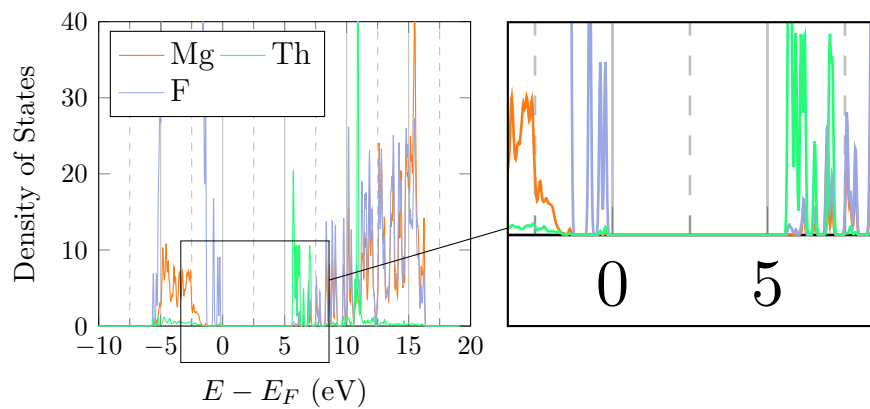


Figure C.29: $\Delta = 5.9133$ eV

15

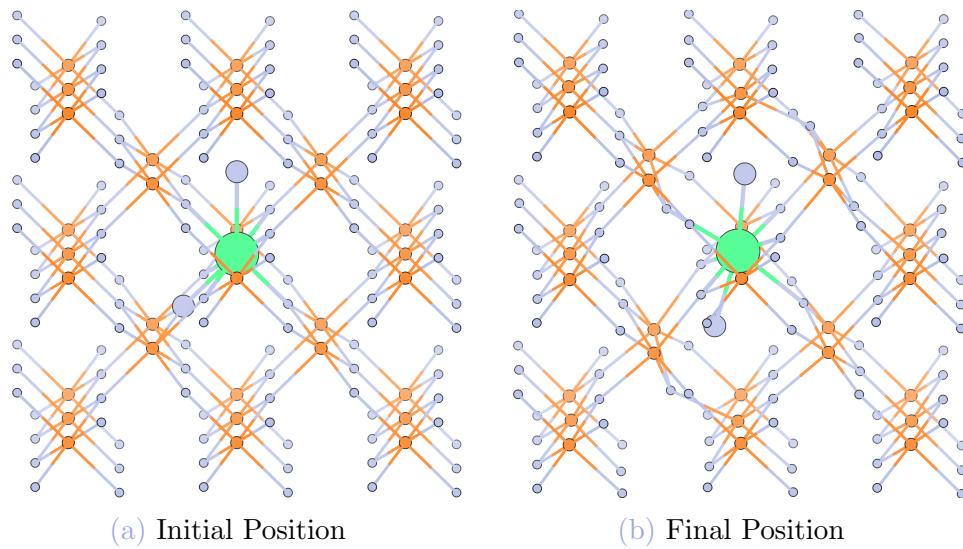


Figure C.30: Initial positions of the interstitial fluorine: $\{0.15, 0.15, 0.5\}$ and $\{0.5, 1, 0.5\}$.

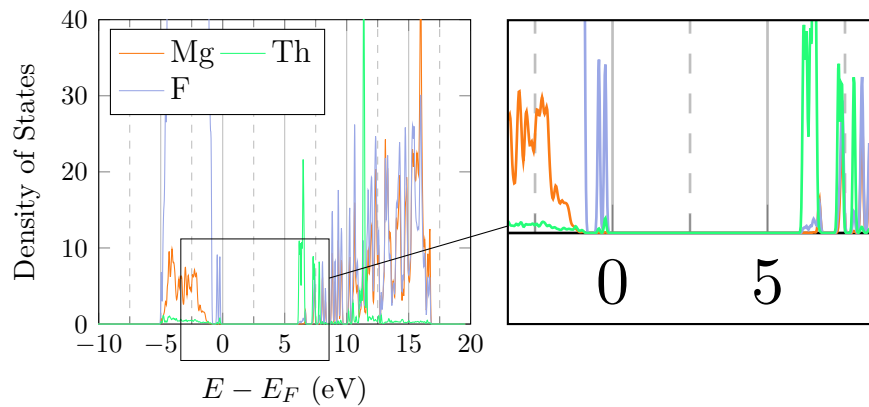


Figure C.31: $\Delta = 6.4008$ eV

16

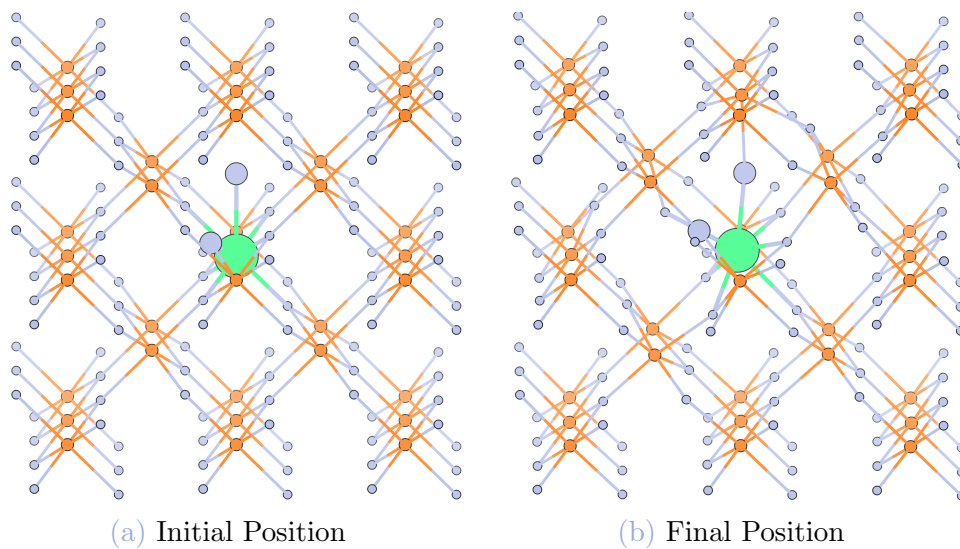


Figure C.32: Initial positions of the interstitial fluorine: $\{0.3, 0.7, 1\}$ and $\{0.5, 1, 0.5\}$.

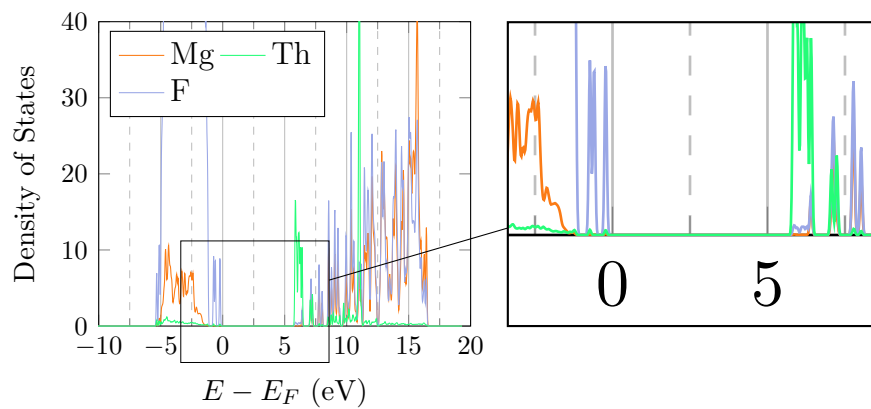


Figure C.33: $\Delta = 6.0628$ eV

17

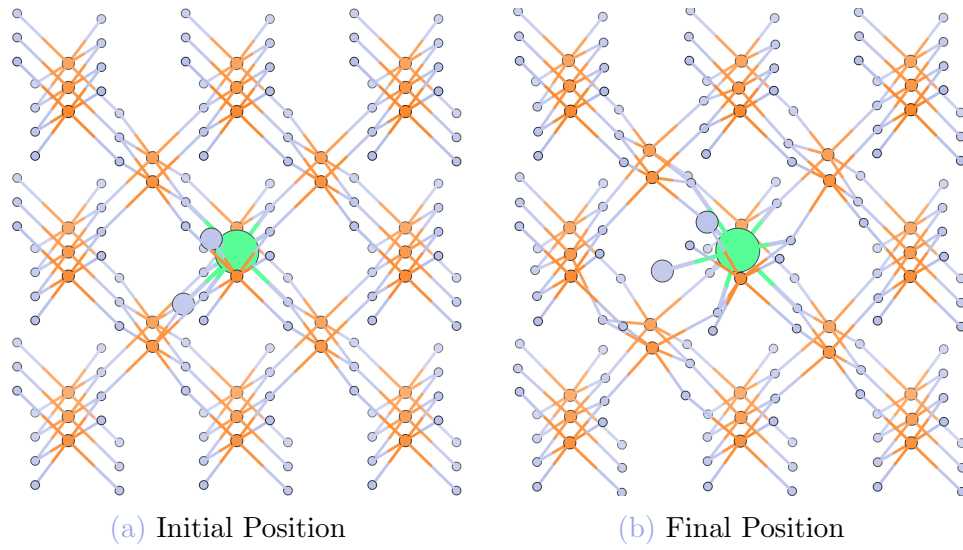


Figure C.34: Initial positions of the interstitial fluorine: $\{0.15, 0.15, 0.5\}$ and $\{0.3, 0.7, 1\}$.

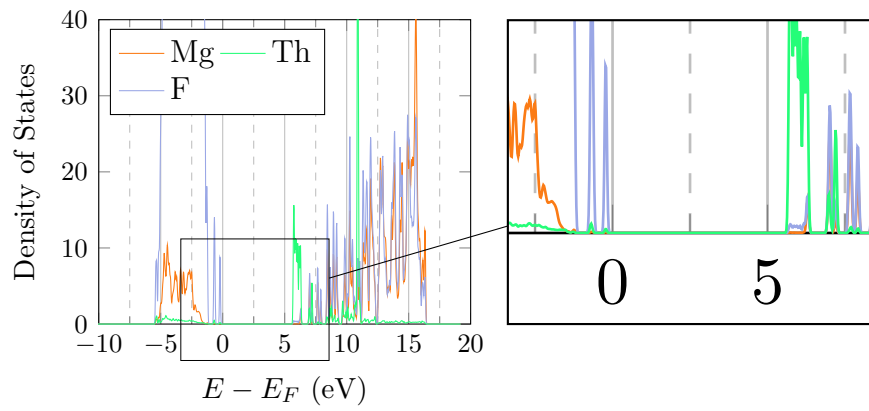


Figure C.35: $\Delta = 5.9309$ eV

18

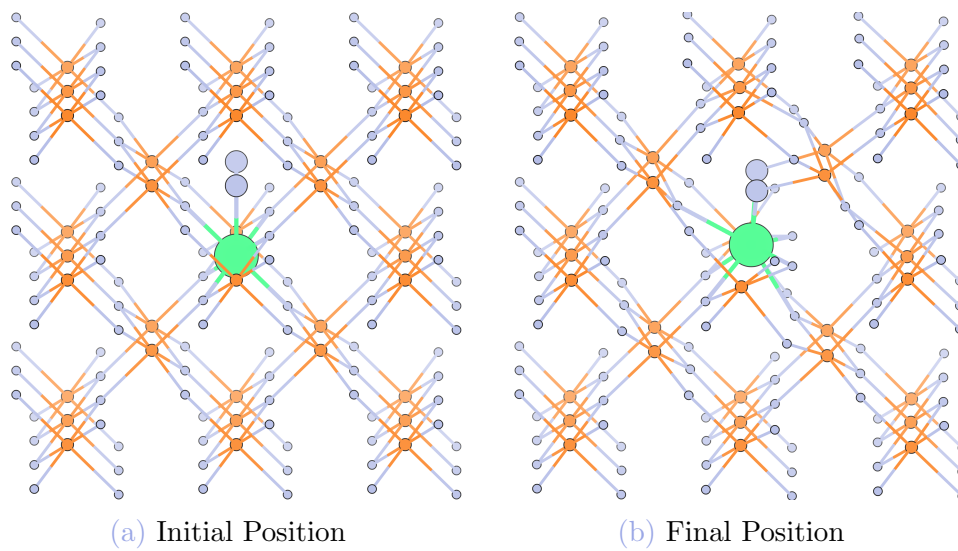


Figure C.36: Initial positions of the interstitial fluorine: $\{0.5, 1, 0\}$ and $\{0.5, 1, 1\}$.

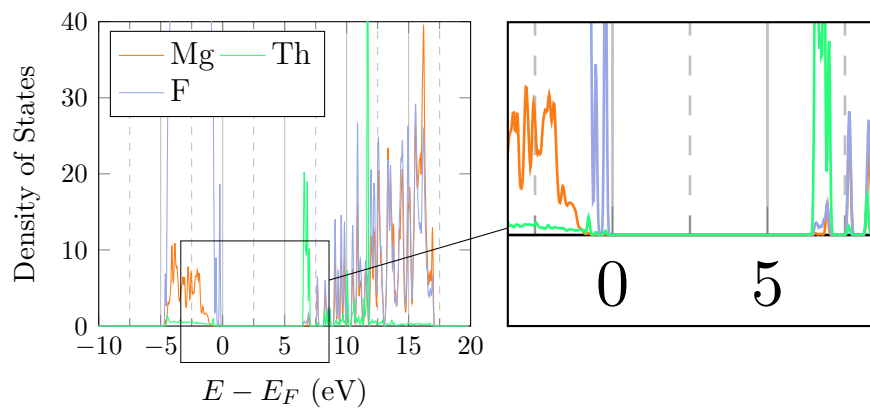


Figure C.37: $\Delta = 6.761$ eV

19

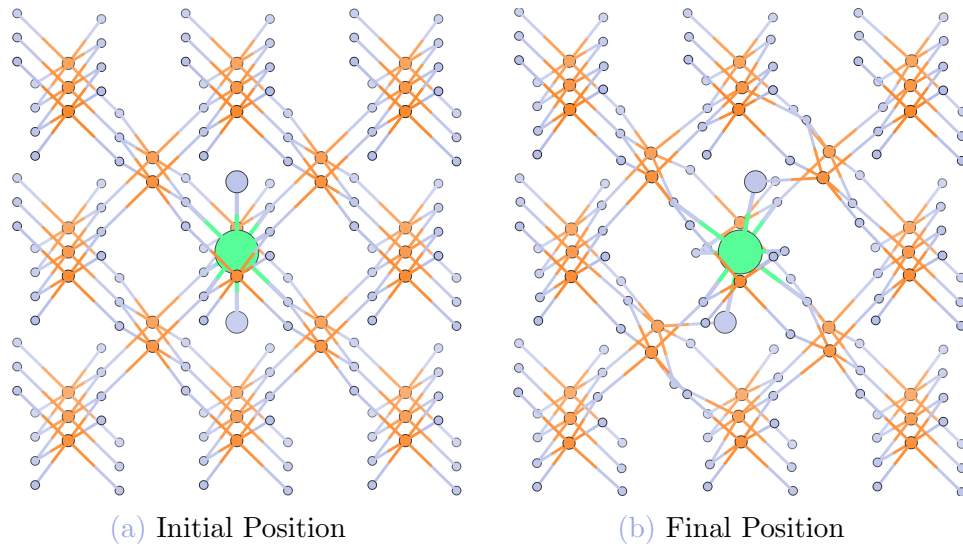


Figure C.38: Initial positions of the interstitial fluorine: $\{0.5, 0, 0\}$ and $\{0.5, 1, 1\}$.

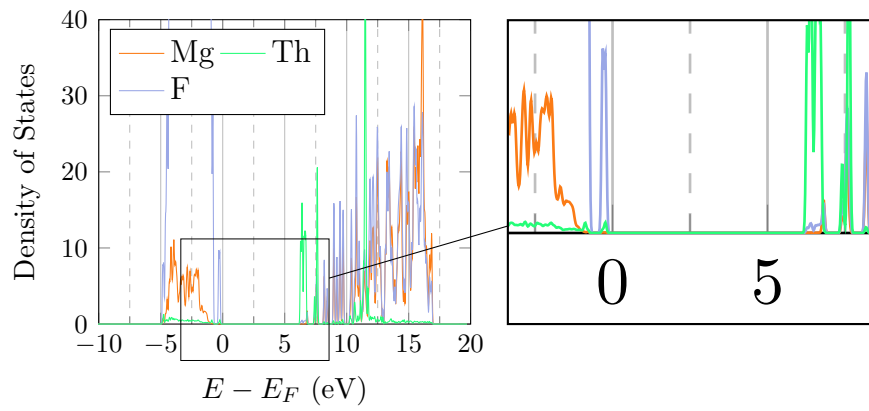


Figure C.39: $\Delta = 6.5103$ eV

20

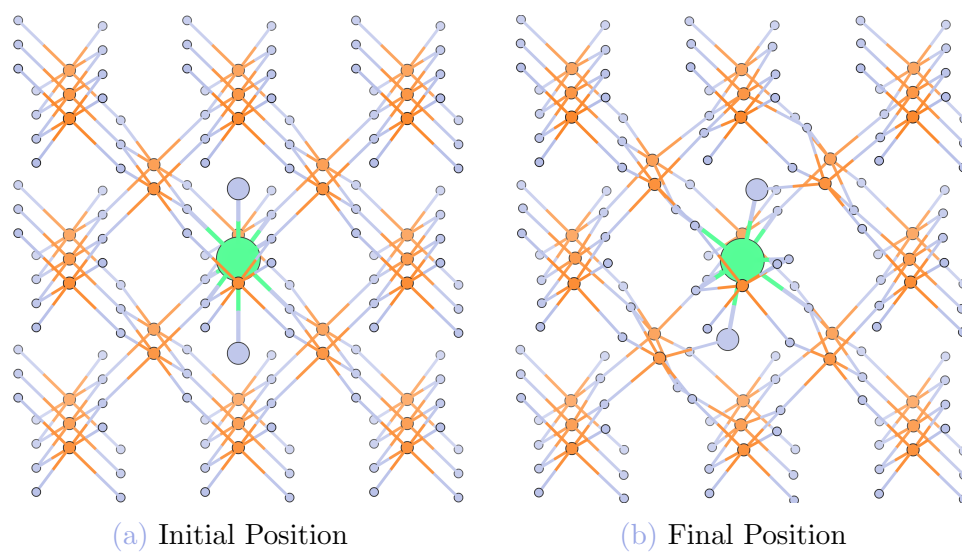


Figure C.40: Initial positions of the interstitial fluorine: $\{0.5, 0, 1\}$ and $\{0.5, 1, 1\}$.

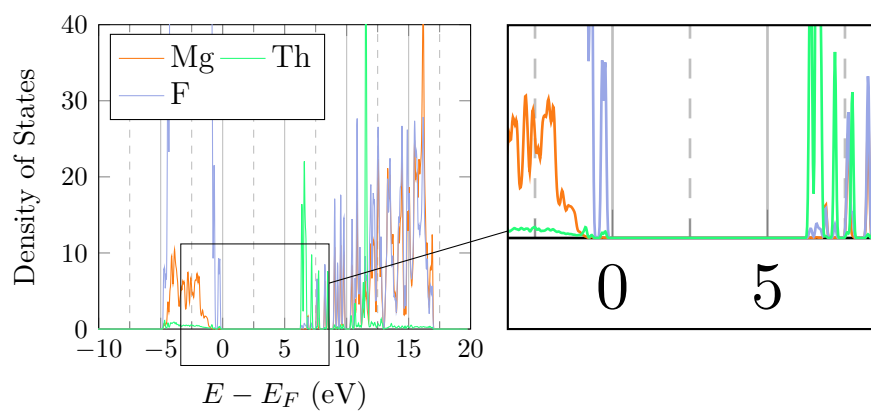


Figure C.41: $\Delta = 6.6002$ eV

21

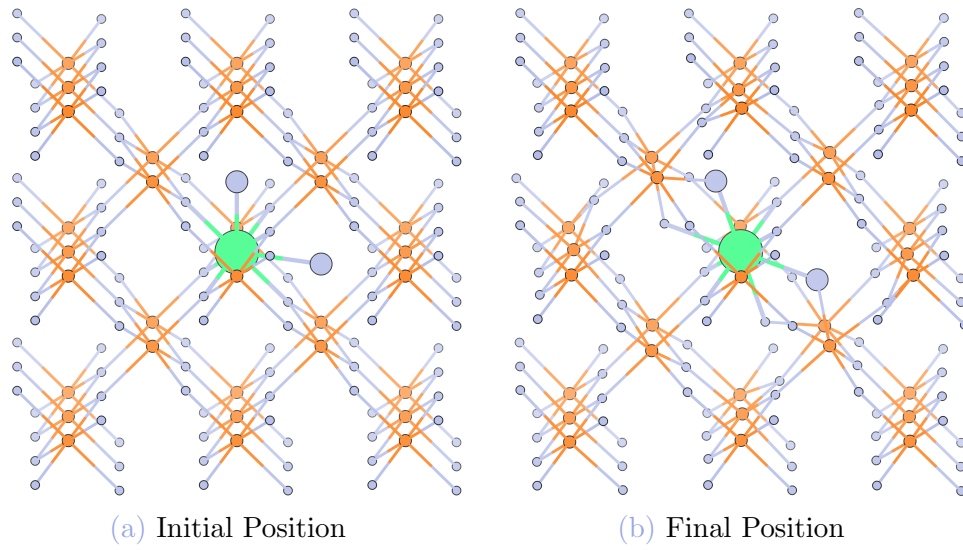


Figure C.42: Initial positions of the interstitial fluorine: $\{0.5, 1, 1\}$ and $\{1, 0.5, 1\}$.

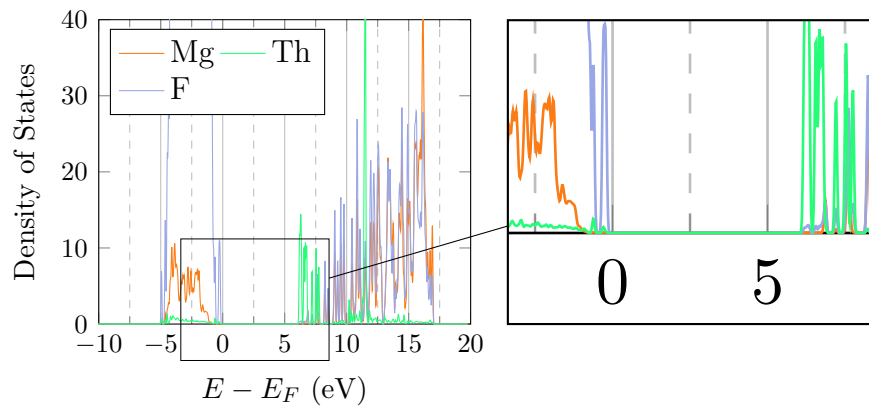


Figure C.43: $\Delta = 6.4141$ eV

22

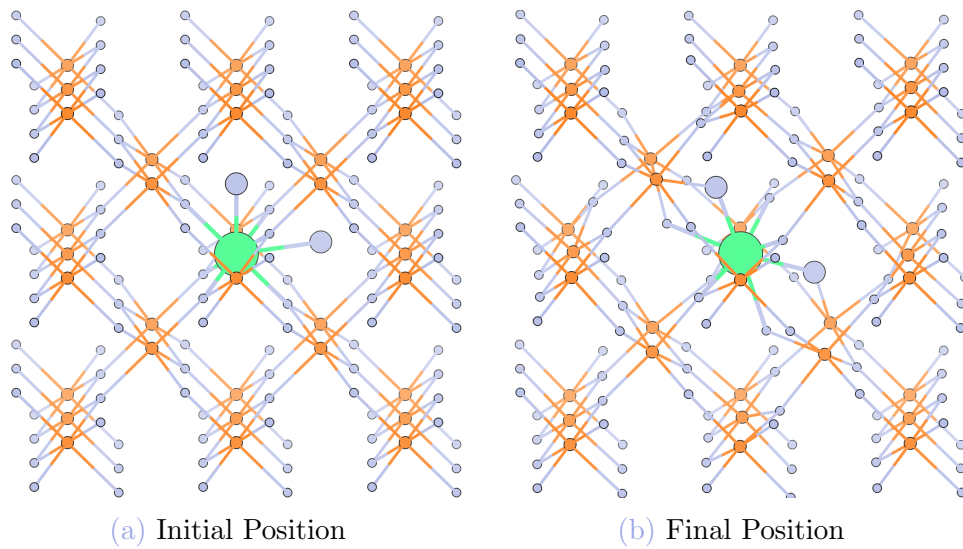


Figure C.44: Initial positions of the interstitial fluorine: $\{0.5, 1, 1\}$ and $\{1, 0.5, 0\}$.

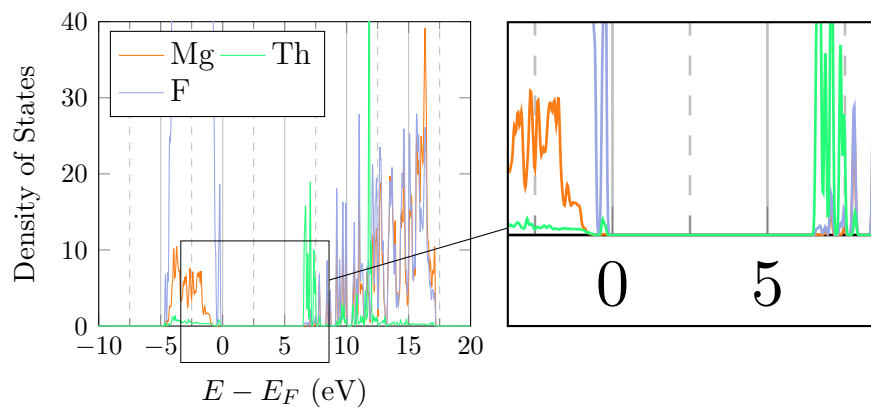


Figure C.45: $\Delta = 6.8147$ eV

23

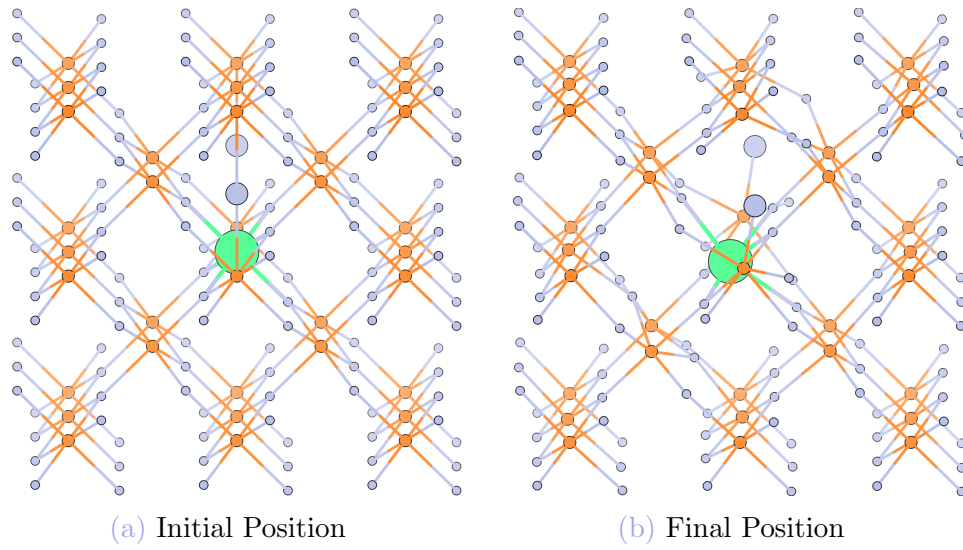


Figure C.46: Initial positions of the interstitial fluorine: $\{0.5, 1.5, 1.5\}$ and $\{0.5, 1.5, -0.5\}$.

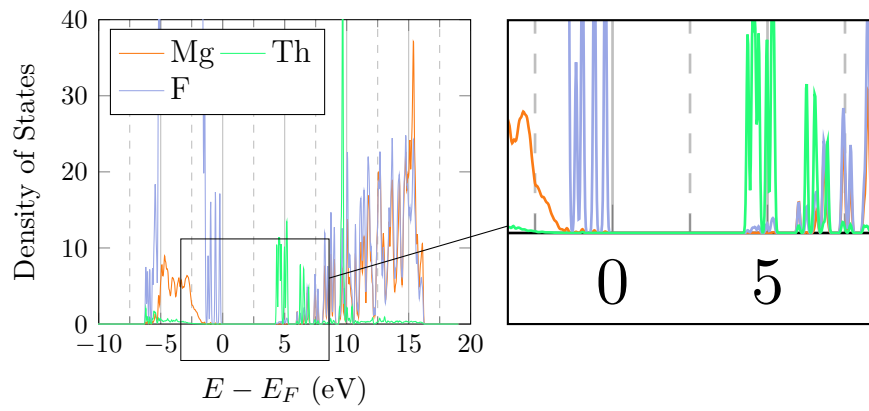


Figure C.47: $\Delta = 4.581$ eV

24

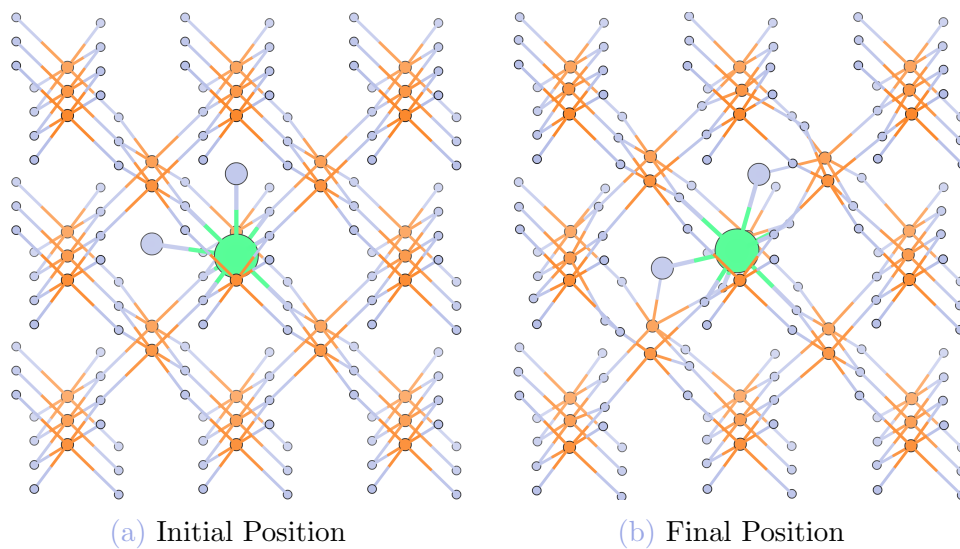


Figure C.48: Initial positions of the interstitial fluorine: $\{0.5, 1, 0.5\}$ and $\{0, 0.5, 0\}$.

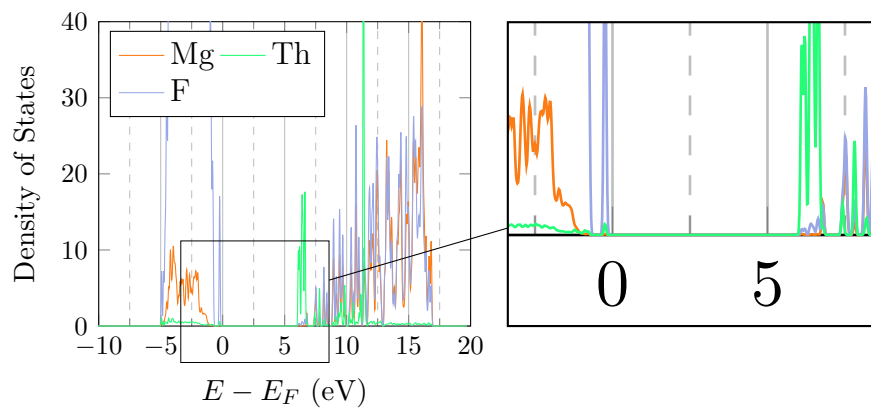


Figure C.49: $\Delta = 6.3362$ eV

25

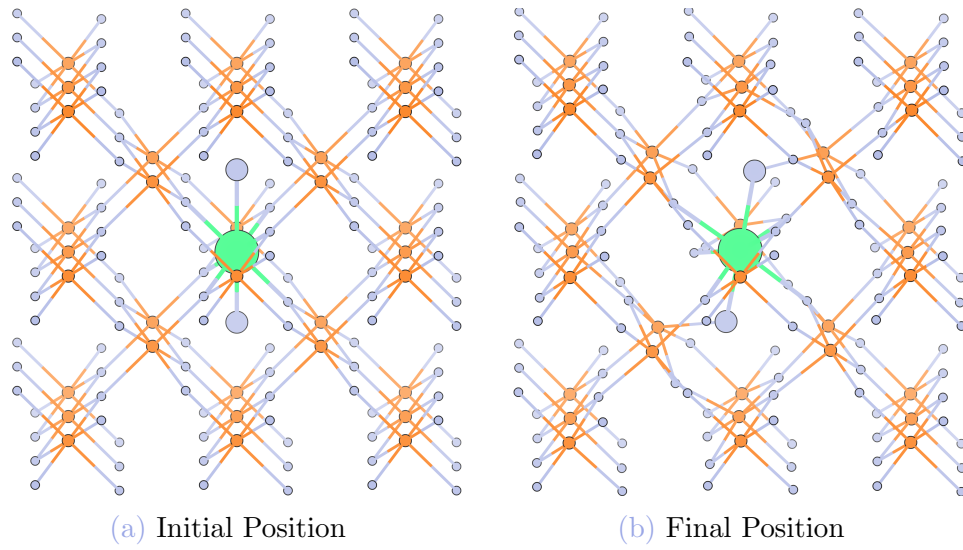


Figure C.50: Initial positions of the interstitial fluorine: $\{0.5, 1, 0.5\}$ and $\{0.5, 0, 0\}$.

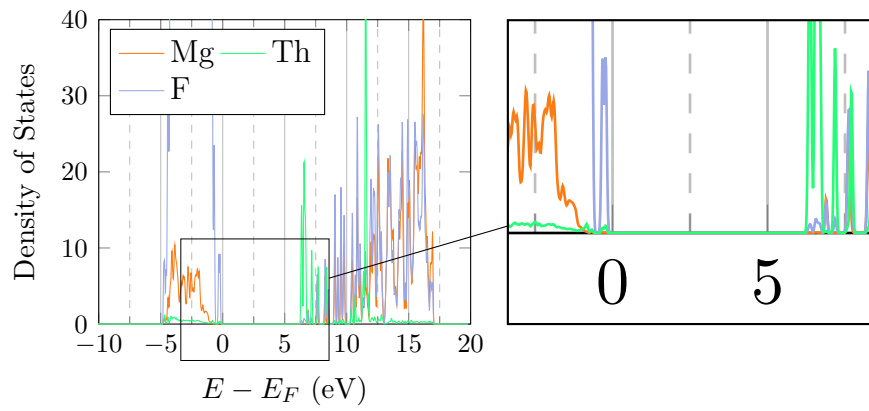


Figure C.51: $\Delta = 6.5602$ eV

C.2.4 Mg vacancy

26

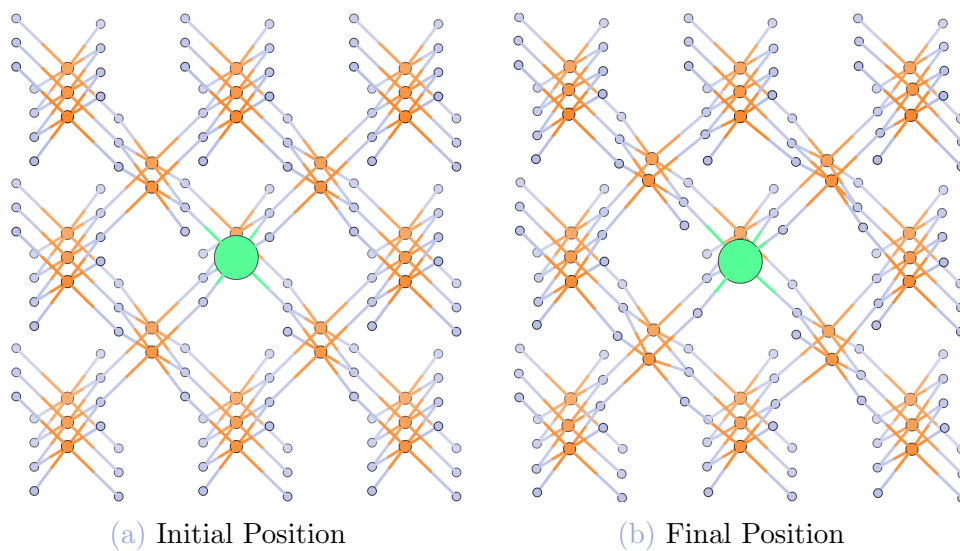


Figure C.52: The magnesium vacancy: $\{0, 1, 1\}$.

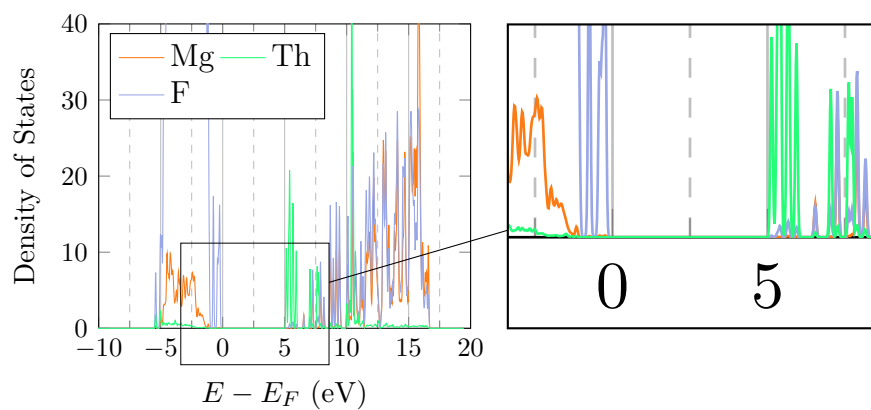


Figure C.53: $\Delta = 5.3627$ eV

27

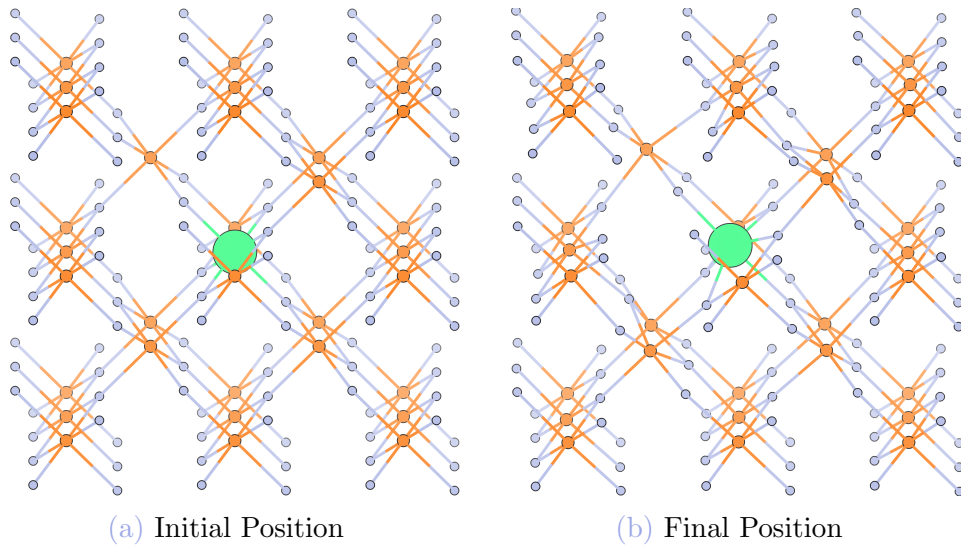


Figure C.54: The magnesium vacancy: {0.5, 0.5, 1.5}

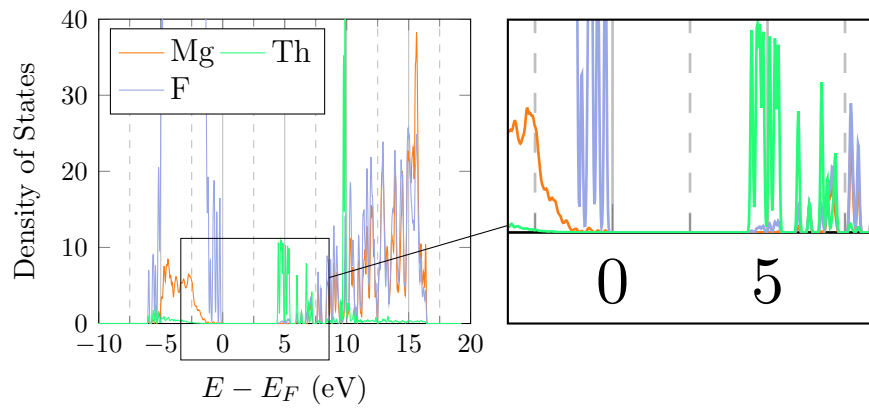


Figure C.55: $\Delta = 4.7093$ eV

28

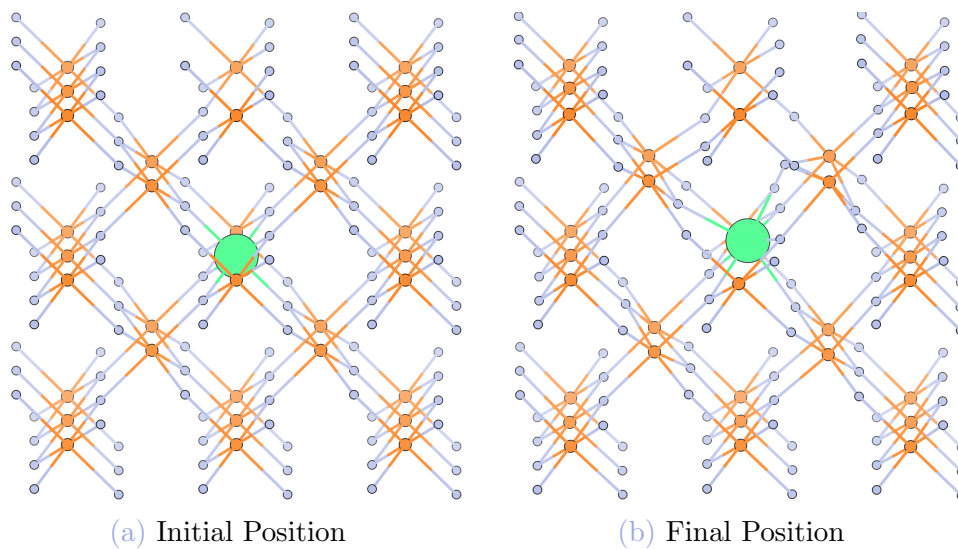


Figure C.56: The magnesium vacancy: $\{0.5, 1.5, 0.5\}$

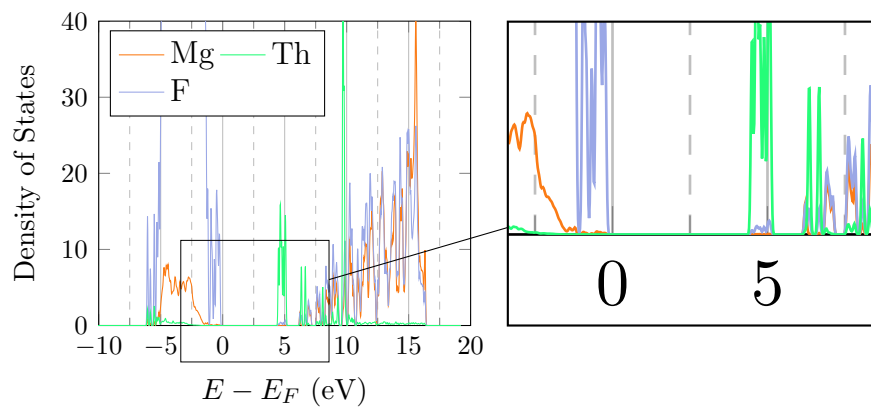


Figure C.57: $\Delta = 4.7307$ eV

Bibliography

- [AAB⁺90] Hisazumi Akai, Masako Akai, S. Blügel, B. Drittler, H. Ebert, Kiyoyuki Terakura, R. Zeller, and P. H. Dederichs. Theory of hyperfine interactions in metals. *Progress of Theoretical Physics Supplement*, 101:11–77, 1990.
- [AG98] F. Aryasetiawan and O. Gunnarsson. The GW method. *Reports on Progress in Physics*, 61(3):237, 1998.
- [AO] Inc. Almaz Optics. Magnesium Fluoride MgF₂. almazoptics.com. Web. 4 OCT 2017. Almaz Optics, Inc.
- [Bau76] W. H. Baur. Rutile-type compounds. V. Refinement of MnO₂ and MgF₂. *Acta Crystallographica Section B*, 32(7):2200–2204, Jul 1976.
- [BBB⁺07] B. R. Beck, J. A. Becker, P. Beiersdorfer, G. V. Brown, K. J. Moody, J. B. Wilhelmy, F. S. Porter, C. A. Kilbourne, and R. L. Kelley. Energy splitting of the ground-state doublet in the nucleus ²²⁹Th. *Phys. Rev. Lett.*, 98:142501, Apr 2007.
- [BCA⁺11] K Babu, Bheema Lingam Chittari, Sushil Auluck, Surya Tewari, and Ganapathy Vaitheeswaran. Structural, thermodynamic and optical properties of MgF₂ studied from first-principles theory. *Journal of Solid State Chemistry*, 184:343–350, 02 2011.
- [Bec93a] Axel D. Becke. Density functional thermochemistry. III. the role of exact exchange. *The Journal of Chemical Physics*, 98(7):5648–5652, 1993.
- [Bec93b] Axel D. Becke. A new mixing of hartree–fock and local density functional theories. *The Journal of Chemical Physics*, 98(2):1372–1377, 1993.

- [BFK⁺15] M. Bartelmann, B. Feuerbacher, D. Krüger, T. and Lüst, Rebhan A., and Wipf A. *Theoretische Physik*. Springer Berlin Heidelberg, 2015.
- [BJA94] Peter E. Blöchl, O. Jepsen, and O. K. Andersen. Improved tetrahedron method for brillouin-zone integrations. *Phys. Rev. B*, 49:16223–16233, Jun 1994.
- [BKM⁺17] Pavlo V. Bilous, Georgy A. Kazakov, Iain D. Moore, Thorsten Schumm, and Adriana Pálffy. Internal conversion from excited electronic states of ²²⁹Th ions. *Phys. Rev. A* 95, 032503, 2017.
- [Blö94] P. E. Blöchl. Projector augmented-wave method. *Phys. Rev. B*, 50:17953–17979, Dec 1994.
- [BO27] M. Born and R. Oppenheimer. Zur Quantentheorie der Molekeln. *Annalen der Physik*, 389(20):457–484, 1927.
- [BPM14] S. Bühler-Paschen and P. Mohn. Festkörperphysik II. Lecture Notes, 2014.
- [Bur16] Bureau International des Poids et Mesures. *BIPM Annual Report on Time Activities*, volume 11, Pavillon de Breteuil, F-92312 SÈVRES Cedex, France, 2016.
- [Buron] J. Burgdörfer. Skriptum zur Vorlesung aus Quantentheorie, Teil II. Lecture Notes, 2009, 3rd edition.
- [BWB⁺09] B R Beck, C Wu, P Beiersdorfer, G V Brown, J A Becker, K J Moody, J B Wilhelmy, F S Porter, C A Kilbourne, and R L Kelley. Improved value for the energy splitting of the ground-state doublet in the nucleus ²²⁹Th, Jul 2009.
- [Cap02] K. Capelle. A bird’s-eye view of density-functional theory. *eprint arXiv:cond-mat/0211443*, November 2002.
- [CC73] D. J. Chadi and Marvin L. Cohen. Special points in the brillouin zone. *Phys. Rev. B*, 8:5747–5753, Dec 1973.
- [Cha98] Jr. Chase, M. W. NIST-JANAF Thermochemical Tables. *J. Phys. Chem. Ref. Data*, Monograph(9), 1998.

- [CTT97] Thomas M. Cotter, Michael E. Thomas, and William J. Tropsf. Magnesium fluoride (MgF_2). In Edward D. Palik, editor, *Handbook of Optical Constants of Solids*, pages 899 – 918. Academic Press, Burlington, 1997.
- [Des16] Philipp Dessovic. Ab-initio calculations for thorium doped calcium fluoride (CaF_2). Diploma thesis, TU Vienna, 2016.
- [dPeM06] Bureau International des Poids et Mesures. *The International System of Units (SI)*. STEDI MEDIA, 8th edition, 2006.
- [ED11] E. Engel and R.M. Dreizler. *Density Functional Theory*. Springer-Verlag Berlin Heidelberg, 1 edition, 2011.
- [Eug90] Eugene S. Kryachko and Eduardo V. Ludeña. *Energy Density Functional Theory of Many-Electron Systems*. Understanding Chemical Reactivity. Springer Netherlands, 1990.
- [Fla06] V. V. Flambaum. Enhanced effect of temporal variation of the fine structure constant and the strong interaction in ^{229}Th . *Phys. Rev. Lett.*, 97:092502, Aug 2006.
- [GFS00] I.M. Gelfand, S.V. Fomin, and R.A. Silverman. *Calculus of Variations*. Dover Books on Mathematics. Dover Publications, 2000.
- [Giu14] F. Giustino. *Materials Modelling using Density Functional Theory: Properties and Predictions*. OUP Oxford, 2014.
- [Gro00] Johannes Grotendorst, editor. *Modern Methods and Algorithms of Quantum Chemistry - Proceedings*, volume 1 of *NIC Series*, 2000.
- [HK64] P. Hohenberg and W. Kohn. Inhomogeneous Electron Gas. *Phys. Rev.*, 136:B864–B871, Nov 1964.
- [HSE03] J. Heyd, G. E. Scuseria, and M. Ernzerhof. Hybrid functionals based on a screened Coulomb potential. *Journal of Chemical Physics*, 118:8207–8215, May 2003.
- [HSL⁺16] N. Huntemann, C. Sanner, B. Lipphardt, Chr. Tamm, and E. Peik. Single-ion atomic clock with 3×10^{-18} systematic uncertainty. *Phys. Rev. Lett.*, 116:063001, Feb 2016.

- [HSNOP13] O. A. Herrera-Sancho, N. Nemitz, M. V. Okhapkin, and E. Peik. Energy levels of th+ between 7.3 and 8.3 ev. *Phys. Rev. A* 88, 012512, 2013.
- [JAG76] C. Jouanin, J.P. Albert, and C. Gout. Band structure and optical properties of magnesium fluoride. *Journal de Physique*, 37(5):595–602, 1976.
- [KF96a] G. Kresse and J. Furthmüller. Efficient iterative schemes for ab initio total-energy calculations using a plane-wave basis set. *Phys. Rev. B*, 54:11169–11186, Oct 1996.
- [KF96b] G. Kresse and J. Furthmüller. Efficiency of ab-initio total energy calculations for metals and semiconductors using a plane-wave basis set. *Computational Materials Science*, 6(1):15 – 50, 1996.
- [KH93] G. Kresse and J. Hafner. Ab initio molecular dynamics for liquid metals. *Phys. Rev. B*, 47:558–561, Jan 1993.
- [KH94] G. Kresse and J. Hafner. Ab initio. *Phys. Rev. B*, 49:14251–14269, May 1994.
- [KH00] W. Koch and M.C. Holthausen. *A chemist’s guide to density functional theory*. Wiley-VCH, 2000.
- [KJ99] G. Kresse and D. Joubert. From ultrasoft pseudopotentials to the projector augmented-wave method. *Phys. Rev. B*, 59:1758–1775, Jan 1999.
- [KLR⁺12] G A Kazakov, A N Litvinov, V I Romanenko, L P Yatsenko, A V Romanenko, M Schreitl, G Winkler, and T Schumm. Performance of a 229 thorium solid-state nuclear clock. *New Journal of Physics*, 14(8):083019, 2012.
- [KSS17] Georgy A. Kazakov, Thorsten Schumm, and Simon Stellmer. Re-evaluation of the beck et al. data to constrain the energy of the th-229 isomer, 2017.
- [KV79] Elton N. Kaufmann and Reiner J. Vianden. The electric field gradient in noncubic metals. *Rev. Mod. Phys.*, 51:161–214, Jan 1979.
- [Laa13] Kari Laasonen. Ab initio molecular dynamics, 2013.

- [LFDF09] Elena Litvinova, Hans Feldmeier, Jacek Dobaczewski, and Victor Flambaum. Nuclear structure of lowest ^{229}Th states and time-dependent fundamental constants. *Phys. Rev. C*, 79:064303, Jun 2009.
- [LYP88] Chengteh Lee, Weitao Yang, and Robert G. Parr. Development of the colle-salvetti correlation-energy formula into a functional of the electron density. *Phys. Rev. B*, 37:785–789, Jan 1988.
- [MI11] Koichi Momma and Fujio Izumi. *VESTA3* for three-dimensional visualization of crystal, volumetric and morphology data. *Journal of Applied Crystallography*, 44(6):1272–1276, Dec 2011.
- [MKE⁺] M. Marsman, G. Kresse, A. Eichler, R. Lorenz, R. Hirschl, and J. Hafner. VASP Tutorial. Institut für Materialphysik and Center for Computational Materials Science, Universität Wien.
- [MP76] Hendrik J. Monkhorst and James D. Pack. Special points for Brillouin-zone integrations. *Phys. Rev. B*, 13:5188–5192, Jun 1976.
- [MWJC07] Philip M. Walker and James J. Carroll. Feature article: Nuclear isomers: Recipes from the past and ingredients for the future, 06 2007.
- [Noba] The Nobel Prize in Chemistry 1998. Nobelprize.org. Web. 23 Jul 2017. http://www.nobelprize.org/nobel_prizes/chemistry/laureates/1998/ (version: 2017-07-23).
- [Nobb] The Nobel Prize in Physics 2005. Nobelprize.org. Web. 23 Jul 2017. http://www.nobelprize.org/nobel_prizes/physics/laureates/2005/ (version: 2017-07-23).
- [ODD⁺06] W. H. Oskay, S. A. Diddams, E. A. Donley, T. M. Fortier, T. P. Heavner, L. Hollberg, W. M. Itano, S. R. Jefferts, M. J. Delaney, K. Kim, F. Levi, T. E. Parker, and J. C. Bergquist. Single-atom optical clock with high accuracy. *Phys. Rev. Lett.*, 97:020801, Jul 2006.
- [Par10] Thomas E Parker. Long-term comparison of caesium fountain primary frequency standards. *Metrologia*, 47(1):1, 2010.

- [PBBS98] Helena M. Petrilli, Peter E. Blöchl, Peter Blaha, and Karlheinz Schwarz. Electric-field-gradient calculations using the projector augmented wave method. *Phys. Rev. B*, 57:14690–14697, Jun 1998.
- [PBE96] John P. Perdew, Kieron Burke, and Matthias Ernzerhof. Generalized gradient approximation made simple. *Phys. Rev. Lett.*, 77:3865–3868, Oct 1996.
- [PEB96] John P. Perdew, Matthias Ernzerhof, and Kieron Burke. Rationale for mixing exact exchange with density functional approximations. *The Journal of Chemical Physics*, 105(22):9982–9985, 1996.
- [PFPT10] S. G. Porsev, V. V. Flambaum, E. Peik, and Chr. Tamm. Excitation of the isomeric ^{229m}Th nuclear state via an electronic bridge process in $^{229}\text{Th}^+$. *Phys.Rev.Lett.*105:182501, 2010.
- [Phi] Philipp. What’s the difference between pbe and b3lyp methods? Chemistry Stack Exchange. <https://chemistry.stackexchange.com/a/11013> (version: 2017-07-20).
- [PT03] E. Peik and Chr. Tamm. Nuclear laser spectroscopy of the 3.5 eV transition in Th-229. *EPL (Europhysics Letters)*, 61(2):181, 2003.
- [PW94] R.G. Parr and Y. Weitao. *Density-Functional Theory of Atoms and Molecules*. International Series of Monographs on Chemistry. Oxford University Press, 1994.
- [PYSP15] Haowei Peng, Zeng-Hui Yang, Jianwei Sun, and John P. Perdew. SCAN+rVV10: A promising van der Waals density functional. *Phys. Rev. X* 6, 041005, 2015.
- [PZOT08] E. Peik, K. Zimmermann, M. Okhapkin, and Chr. Tamm. Prospects for a nuclear optical frequency standard based on thorium-229. arXiv:0812.3548, 2008.
- [RDG⁺10] Wade G. Rellergert, D. DeMille, R. R. Greco, M. P. Hehlen, J. R. Torgerson, and Eric R. Hudson. Constraining the evolution of the fundamental constants with a solid-state optical frequency reference based on the ^{229}Th nucleus. *Phys. Rev. Lett.*, 104:200802, May 2010.

- [Rob79] J Robertson. Electronic structure of SnO_2 , GeO_2 , PbO_2 , TeO_2 and MgF_2 . *Journal of Physics C: Solid State Physics*, 12(22):4767, 1979.
- [RS11] Thorsten Rohwedder and Reinhold Schneider. An analysis for the diis acceleration method used in quantum chemistry calculations. *Journal of Mathematical Chemistry*, 49(9):1889, Aug 2011.
- [SCLR69] G. Stephan, Y. Le Calvez, J.C. Lemonier, and Mme S. Robin. Properties optiques et spectre electronique du MgF_2 et du CaF_2 de 10 à 48 eV. *Journal of Physics and Chemistry of Solids*, 30(3):601 – 608, 1969.
- [Sla29] J. C. Slater. The Theory of Complex Spectra. *Physical Review*, 34:1293–1322, November 1929.
- [SM07] Ron Shepard and Michael Minkoff. Some comments on the DIIS method. *Molecular Physics*, 105(19-22):2839–2848, 2007.
- [SRP15] Jianwei Sun, Adrienn Ruzsinszky, and John P. Perdew. Strongly constrained and appropriately normed semilocal density functional, 2015.
- [SRZ⁺15] Jianwei Sun, Richard C. Remsing, Yubo Zhang, Zhaoru Sun, Adrienn Ruzsinszky, Haowei Peng, Zenghui Yang, Arpita Paul, Umesh Waghmare, Xifan Wu, Michael L. Klein, and John P. Perdew. SCAN: An efficient density functional yielding accurate structures and energies of diversely-bonded materials, 2015.
- [SS83] L. J. Sham and M. Schlüter. Density-functional theory of the energy gap. *Phys. Rev. Lett.*, 51:1888–1891, Nov 1983.
- [SSS15] Simon Stellmer, Matthias Schreidl, and Thorsten Schumm. Radioluminescence and photoluminescence of $\text{Th}:\text{CaF}_2$ crystals. *Sci. Rep.* 5, 15580, 2015.
- [Tho27a] L. H. Thomas. The calculation of atomic fields. *Proceedings of the Cambridge Philosophical Society*, 23:542, 1927.
- [Tho27b] L. H. Thomas. Un Metodo Statistico per la Determinazione di alcune Prioprietà dell’Atomo. *Rend. Accad. Naz. Lincei*, 6:602–607, 1927.

- [Tka11] E. V. Tkalya. Proposal for a nuclear gamma-ray laser of optical range. *Phys. Rev. Lett.*, 106:162501, Apr 2011.
- [Tuc02] Mark E Tuckerman. Ab initio molecular dynamics: basic concepts, current trends and novel applications. *Journal of Physics: Condensed Matter*, 14(50):R1297, 2002.
- [vD11] Leon van Dommelen. Quantum mechanics for engineers. Online Release: <http://www.dommelen.net/quantum2/index.pdf>, 2011.
- [vdWSL⁺16] Lars von der Wense, Benedict Seiferle, Mustapha Laatiaoui, Jürgen B. Neumayr, Hans-Jörg Maier, Hans-Friedrich Wirth, Christoph Mokry, Jörg Runke, Klaus Eberhardt, Christoph E. Düllmann, Norbert G. Trautmann, and Peter G. Thirolf. Direct detection of the 229th nuclear clock transition. *Nature*, 533:47 EP –, May 2016. Article.
- [vdWSLT17] Lars von der Wense, Benedict Seiferle, Mustapha Laatiaoui, and Peter G. Thirolf. The extraction of 229–Th3+ from a buffer-gas stopping cell. *Nucl. Instrum. Meth. B* 376, 260-264, 2017.
- [Wgs] Wgsimon. Microprocessor transistor counts 1971-2011 & moore’s law. Wikipedia. https://upload.wikimedia.org/wikipedia/commons/0/00/Transistor_Count_and_Moore%27s_Law__2011.svg (version: 2017-10-30).
- [XI04] Xin Xu and William A. Goddard III. The extended perdew-burke-ernzerhof functional with improved accuracy for thermodynamic and electronic properties of molecular systems. *The Journal of Chemical Physics*, 121(9):4068–4082, 2004.
- [ZSPW17] Yubo Zhang, Jianwei Sun, John P. Perdew, and Xifan Wu. Comparative first-principles studies of prototypical ferroelectric materials by LDA, GGA, and SCAN meta-GGA. *Phys. Rev. B* 96, 035143, 2017.